Structure, stability properties, and nonlinear dynamics of lateral modes of a broad area semiconductor laser

Blaaberg, Søren ; Rottwitt, Karsten; Petersen, Paul Michael; Tromborg, Bjarne

Publication date:
2007

Document Version
Early version, also known as pre-print

Structure, stability properties, and nonlinear dynamics of lateral modes of a broad area semiconductor laser

Søren Blaaberg Jensen

Ph.D. thesis

COM·DTU
November 2006

Structure, stability properties, and nonlinear dynamics of lateral modes of a broad area semiconductor laser

Søren Blaaberg Jensen

This thesis is submitted as part of the requirements for obtaining the Ph.D. degree from the Technical University of Denmark. The project was funded by Risø National Laboratory.

Supervisors:

Bjarne Tromborg Department of Communications, Optics and Materials
Karsten Rottwitt Department of Communications, Optics and Materials
Paul Michael Petersen Risø National Laboratory

Søren Blaaberg Jensen Kgs. Lyngby, November 6, 2006

Abstract

The subject of this thesis is a theoretical investigation of the nonlinear lateral modes of broad area (BA) semiconductor lasers including studies of stationary properties, of stability properties, and of the dynamics of a BA laser in an external cavity.

The most prominent characteristics of the output field of a BA laser are due to lateral properties. A detailed investigation of stationary lateral field distributions is carried out and leads to the finding of a systematic structure of several categories of lateral nonlinear modes. In addition to the known definite-parity modes, asymmetric modes are found, although the physical system under investigation is symmetric. The structure and interrelationship between different modes are also seen in their tuning curves.

A stability analysis of the above mentioned stationary solutions must be carried out in order to evaluate their physical role. By means of a Green's function method a small-signal analysis is carried out with emphasis on the stability properties. It is found that all regarded modes are unstable except for the case of very low pump currents. The small-signal stability analysis explains why BA lasers are generally found to have fluctuating output fields: at considerable pump currents there are no stable stationary solutions.

An existing external-cavity scheme including a spatial filter is imitated theoretically and it is found that one consequence of the external cavity is to dampen the lateral dynamics of the field, which in turn leads to a improvement of the spatial coherence of the output. The near-field reveals that the external-cavity scheme changes the lateral dynamics of the BA laser to a behavior more similar to a laser array.

Resume

Titlen på dette Ph.d.-projekt er "Struktur, stabilitetsegenskaber og ikke-lineær dynamik i bred-areal halvlederlasere". Indholdet er en teoretisk undersøgelse af ikke-lineære laterale modes i bred-areal-lasere (BA-lasere). Undersøgelsen omfatter stationære egenskaber, stabilitetsegenskaber samt dynamiske egenskaber af en BA-laser i en ekstern kavitet.

De mest tydelige karateristika ved en BA-lasers udgangsfelt skyldes laterale egenskaber. En detaljeret undersøgelse af stationære løsninger til det laterale feltproblem udføres og leder til erkendelsen af en systematisk struktur i flere kategorier af laterale ikke-lineære modes. I tillæg til kendte modes med bestemt paritet findes asymmetriske modes selvom det betragtede fysiske system er symmetrisk. Strukturen og indbyrdes tilhørsforhold mellem statinonære tilstande ses også på deres tuningskurver.

En stabilitetsanalyse af de ovenfor omtalte stationære tilstande udføres for at evaluere deres fysiske betydning. Ved hjælp af en Green's funktion metode udføres en småsignalanalyse med hovedvægt på stabilitetsegenskaber. Det viser sig at alle betragtede stationære løsninger er ustabile bortset fra ved meget lave pumpestrømme. Den lineære stabilitetsanalyse forklarer hvorfor BA-lasere generelt har fluktuerende udgangsfelter: Ved betragtelige pumpestrømme er ingen stationære løsninger stabile.

Et eksisterende ekstern-kavitets-system der indbefatter et rumligt filter imiteres teoretisk og det bliver klart at en konsekvens af den eksterne kavitet er at dæmpe nær-feltes laterale dynamik, hvilket medfører en forbedret rumlig kohærens. Nær-feltet afslører at den eksterne kavitet ændrer BA-laserens laterale dynamik til mere at ligne dynamikken i et laser array.

Acknowledgments

Many thanks to my main supervisor Bjarne Tromborg for sharing some of his wisdom with me and for his generous engagement in the project. It was always a pleasure spending time with Bjarne.
Also thanks to Karsten Rottwitt for stepping in as main supervisor the last few months after Bjarne retired. I wish all the best to Søren Dyøe Agger in the years to come. Colleagues at COM are acknowledged, especially a long string of nice office mates. The last of whom was Niels Gregersen who had to put up with my foot tapping.
Special thanks go to Lone Bjørnstjerne for her kind help on many occasions.

At Risø I thank Paul Michael Petersen for funding and many nice people for some good times.

Contents

Chapter 1

Introduction

Broad area (BA) semiconductor lasers are edge-emitting semiconductor lasers usually designed as high-power laser devices intended to emit as much power as possible while at the same time having a reasonably long lifetime. They are wide-aperture Fabry-Perot lasers which, in their simplest form, only offer guiding of light by means of index guiding in one transverse direction; in the second much broader transverse direction (the lateral direction) the light is purely gain guided. An injected current inverts the semiconductor gain material over a limited lateral region where light is amplified. The broadness of the lateral region pumped by the injected is motivated by a combined urge for high output power along with the necessity of lowering the intensity of light to avoid catastrophic optical damage.

BA lasers, being Fabry-Perot lasers, are longitudinally multi-moded. However, the main interest both from a theoretical and an application point of view has traditionally been directed towards the lateral behaviour. Modern BA lasers usually have emitter-widths of 100 μm or wider. The geometry of BA lasers gives a single-mode behavior in the index guided transverse direction while the behaviour in the lateral gain guided region typically gives rise to a heavily laterally multi-moded behaviour yielding complex variations in space and time often termened filamentation giving inherently poor coherence properties. Consequently, various schemes aimed at improving the coherence of the output of BA lasers have been suggested.

While the incoherent output is of inconvenience for applications demanding high power, BA lasers form a laboratory for the study of nonlinear phenomena. The work presented in this thesis is theoretical. The purpose of

the work is to obtain a better understanding of the lateral properties of BA lasers. While the dynamics of BA lasers has been studied quite a lot, the stationary mode structure has been studied less systematicly. We perform an in-depth investigation of the stationary lateral modes in a BA Laser. After finding stationary solutions in the lateral nonlinear system, we go through a small-signal analysis. In time-domain calculations we try to reproduce experimental behavior of a set-up involving a BA laser in an asymmetric external cavity acting as a spatial filter. The purpose of the cavity is to improve the spatial coherence of the BA laser. The contents of the remaining chapters is outlined below.

In **Chapter 2** we present the regarded BA-laser device. It is a generic structure as our aim is to do a general investigation rather than to view a particular design. Motivated by the need for lasers with improved coherence properties, an existing external-cavity scheme aimed at improving the spatial coherence is described. We study this secheme in a later chapter. We lastly aim to give a very brief overlook of the theoretical treatment of BA lasers, while mentioning the approaches we pursue in the subsequent chapters.

In **Chapter 3** we first derive the main equations governing the lateral field distribution and carrier-density distribution using mean-field theory. Here mean-field theory yields performing an average over the longitudinal direction of the laser. We then combine these two equations to form a single, nonlinear field equation with the aim of finding stationary solutions. With appropriate boundary conditions for lateral gain guided modes, stationary solutions are then found. We find that the variety and structure of lateral stationary solutions and the way their frequencies vary with pump current to be much richer than what has previously been shown [1]. We find asymmetric modes in the symmetric laser structure and other modes which can only exist due to the nonlinear nature of the gain material. The modes turn out to be related in a systematic structure that we have found in their tuning curves, i.e. curves showing the stationary frequency of the modes versus pump current, and in their field distributions.

Along with the results of Chapter 3 yielding stationary solutions , **Chapter 4** is of a theoretical nature. In this chapter we perform a small-signal analysis of the nonlinear stationary solutions obtained in Chapter 3 using a Green's function approach. In particular we investigate the stability proper-

ties of selected modes. The analysis shows that all investigated lateral modes are unstable with the exception of the two lowest order modes at very low pump currents. This fundamental result is in correspondance with streak-camera measurements [2] and large-signal theory [3][4] which tell that BA lasers are never in a steady state when the applied current in considerable.

Chapter **5** contains time-domain calculations based on the numerical method named hopscotch. A solitary BA laser is compared to a BA laser in an asymmetric external cavity. The external cavity improves the spatial coherence of the lsaser. We obtain a good qualitative agreement with measurements found in the literature. Our calculations show that the asymmetric external cavity laser operates in a fluctuating state.

In **Chapter 6** we present a method to calculate lateral modes in a BA laser via a mode expansion. With an expansion in linear gain guided lateral modes, it becomes possible to recognize the most significant perturbations of the field at low currents.

Chapter 7 gives a short summary of results.

Chapter 2

Broad area semiconductor lasers

The geometry of BA-laser devices with their wide apertures allow for high-power output when pumped at high currents. In fact the geometry also makes BA lasers suitable for scientific purposes as testbeds for gain materials [5] or for experiments on spatially nondegenerate four-wave mixing. Injecting a pump- and a probe beams at different angels with a frequency detuning makes it possible to measure ambipolar carrier diffusion coefficients and carrier lifetimes [6]. Their usefulnes as lasers, however, is also limited by the geometry since it allows the lateral field distribution to vary in time and space in a complex manner that ruins the coherence of the output beam. The strongly nonlinear behavior due to the light-semiconductor interaction also gives a range of interesting phenomena to be studied. Moreover, the hunt for methods to improve the coherence of the output of BA lasers has been ongoing for at least two decades.

Now, we desribe the basics of BA lasers, and qualitatively discuss their spatiotemporal behavoir which is often described through the process of filamentation. We then, after briefly reviewing methods to improve coherence properties of BA lasers, describe an asymmetric external cavity BA laser that we investigate in Chapter 5. Lastly in this chapter, we discuss some of the different paths that one can choose, including those that we choose, when one studies BA lasers theoretically.

2.1 Broad area laser devices

The name "BA laser" originates from the laser geometry. When increasing the current in a semiconductor laser high above its threshold, the intensity of light eventually surpasses a threshold where catastrophic optical damage is done to the laser facets. At the same time many applications demand high-power output. In order to keep the intensity of light below the damage threshold of the laser facets and at the same time obtain high output power, the laser structure is made wider in the lateral direction.

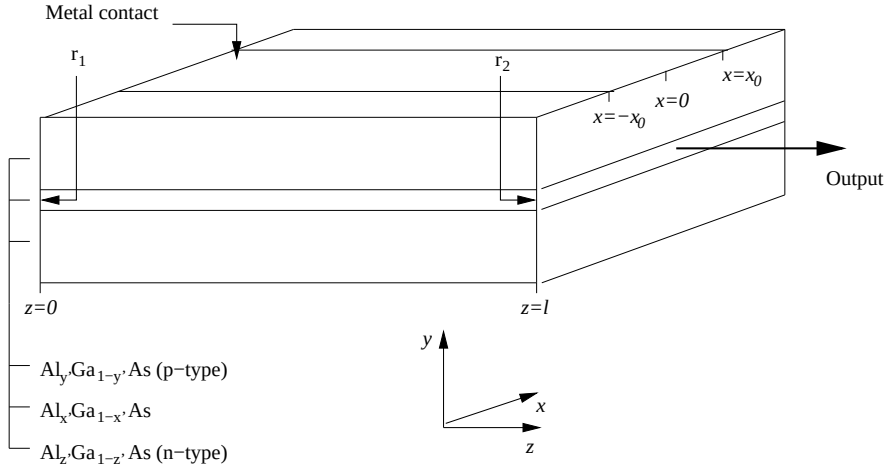

Figure 2.1: Generic structure of a broad area laser. The active layer ($Al_{x'}Ga_{1-x'}As$) is sandwiched between two cladding layers. The coordinate system represents the lateral (x), the transverse (y), and the longitudinal (z) axes, respectively. The origin is centered in the middle of the waveguide at the back facet. Here it is dispalced for clarity.

BA lasers are edge-emitting lasers. Figure 2.1 illustrates a BA laser in its simplest form. Three semiconductor layers form a p-i-n junction. The top layer is a p-type doped cladding layer. The middle layer, an intrinsic core layer, is the active layer where light may be amplified in case the material is inverted. The bottom layer is an n-type doped cladding layer. On top of the structure sits a metal contact. Not shown in the figure is the substrate on which the n-type layer is grown. Under the substrate a second metal contact is deposited. In the calculations presented in this thesis we have assumed the material composition of the BA laser to be in the AlGaAs

material system but this is not essential for the theoretical analysis. From Figure 2.1, it is evident that there is no lateral (in the x-direction) variation in the material composition and therefore no lateral variation in the refractive index present in the system. The BA laser regarded here is thus purely gain guided. For a purely gain guided BA laser the optical field is limited in the lateral direction only by the extend of the region having appreciable current pumping. BA lasers with weak lateral index guiding [7] and more complicated and refined layer structures [8] than the simple one in Figure 2.1 have been realized. However, the work presented in this thesis is purely theoretical and has no relation to a specific device wherefore we focus on a generic BA-laser structure. This generic structure is thus a wide double heterostructure with a wide top metal contact. The double heterostructure serves two important purposes. Since the bandgaps of the p- and n-layers are higher than the one of the intrinsic layer, carriers are confined in the intrinsic layer where they are to recombine preferably under stimulated emission. In addition, the intrinsic layer also confines light as its refractive index is higher than the two outer layers. The double heterostructure is therefore also a slab waveguide responsible for the transverse (y-direction) guiding of light. The core layer is made sufficiently thin so that only one transverse mode is supported. Most if not all commercially available BA lasers have one or more quantum wells serving as the gain material. When quantum wells constitute the active region of the laser a separate-confinement heterostructure must carry the burden of waveguiding. BA lasers with quantum dot gain material have also been reported [9].

For a gain guided single-stripe AlGaAs laser supporting only one lateral mode, the width of the top metal contact (the current stripe) is typically 3 to 5 μm. The top metal contact of a BA laser can be said to be one or two orders of magnitude wider than that of a singe-lateral mode laser. BA lasers with current stripes as wide as 1000 μm have been reported [10]. In this thesis we regard a width of $w = 2x_0 = 200$ μm. When increasing the width to several tens of microns, one allows for lateral multimode operation. In fact when increasing the width of the current stripe to obtain a higher maximun output power, the high-power performance is limited by spatially localized bursts (filaments) of high intensity, which in itself lowers the threshold for catastrophical optical damage of the output facet [11]. Nevertheless, the highest output power achievable from a semiconductor laser increases with increasing area of the output facets. Therefore BA lasers remain poplar for high-power applications. The laser mirrors (facets) with amplitude reflectiv-

ities r_1 and r_2 are obtained by cleaving the crystal in planes perpendicular to the grown layers. The facets may in addition be coated to modify their reflectivities.

The p-i-n junction is forward-biased to obtain inversion. When the diode is forward biased electrons and holes are injected into the intrinsic layer where they may recombine or continue to the layer opposite to the one from which they were injected. As the forward bias is increased the quasi-Fermi levels of the electrons and the holes, will increase and decrease, respectively. When they are separated by the bandgap energy, the material is inverted. In semiconductor laser modeling it is often assumed that one is not too far away from thermal equilibrium and that all electron-hole transitions take place between the extrema of one conduction band and one valence band, i.e. at zero wave number. In this thesis we will employ this approach.

2.2 Spatiotemporal behavior

In most experimental work on high-power lasers, slow detection methods average out any fast variations in time giving only a static spatial variation in the intensity distribution to read out. Such measurements are unlikely to give a full understanding of the physical mode of operation of a particular laser. Fischer *et al.* [2] measured the spatio-temporal dynamics of the output field of a BA laser on a picosecond time scale using a streak-camera. The near-field was seen to consist of rapidly changing irregular lateral patterns of light intensity. A BA laser pumped at a high current never finds a steady state. The dynamics following the initial relaxation oscillations may be divided into two domains of filaments [12] where a filament is a small region in the active region of relatively high intensity. Firstly, "static" filamentation where regions of the near-field of high respectively low intensity retain their individual lateral positions. The field of a BA laser is not static, however, even at moderate (moderate not being high) pump currents. Thus the "static" filaments are turned on and off on a time scale of the order of 100 ps. The reason for this is "dynamic filamentation", the second domain, which means that the filaments tend to move laterally as a function of time. This behavior manifests itself as zig-zag patters in the temporal evolution of the near-field (we shall see an example of this in Chapter 5). If a filament originating on one edge of the active region migrates all the way to the opposite edge it would take roughly between 200 to 500 ps for the inspected device

of [2]. The device was a GaAs/AlGaAs device of width 100 μm pumped at two times threshold. Static theories of filamentation have been also been put forth [13]. In fact one may interpret stationary field distributions obtained by solving an appropriate set of model equations, i.e. a nonlinear spatial mode in the laser, as static filamentation [1][14]. In Chapter 3 we find several different types of nonlinear modes revealing a rich variety of stationary, spatial shapes.

The irregular output of BA lasers has its origin in the process of dynamic filamentation. In BA lasers with no passive, lateral index guiding, the lateral field distribution is constrained laterally only by the finite width of the lateral current distribution. Antiguiding in semiconductors is the phenomenon where regions with relatively high carrier density or inversion (and therefore a relatively high gain) implies a relatively low refractive index. Oppositely for regions with relatively low carrier density (and therefore a relatively low gain) which have a relatively high refractive index. The filamentation process involves antiguiding that causes self-focusing, diffraction, and local differences in gain: Consider a local burst of high intensity (a filament). The carrier density is locally depleted causing locally low gain and due to the antiguiding effect locally high refractive index compared to the surrounding area where the gain is relatively high and hence the refractive index relatively low. The filament can persist due to the index guide which has been formed. Eventually, however, the gain in its neighboring area, where the intensity of light is low, rises sufficiently high above the threshold level, due to the pump current, so that the filament moves laterally and is amplified and the process can start over. With many such filaments interacting nonlinearly the overall result is an apparently chaotic behavior in time and space. We will show examples of this behavior in Chapter 5. The above description of dynamic filamentation relies on local depletion of the carrier density. At the two edges of the pumped region the carrier density is typically relatively high due to a relatively low intensity of light indicating that the total field creates a global waveguide through gain-guiding and anti-guiding. By global we mean on the length scale of the width of the metal contact $w = 2x_0$.

2.3 Schemes aimed to increase coherence

Because BA lasers can deliver high-power output but have weak coherence properties, there has been an urge to improve the latter. It seems that the

largest effort has been to improve the spatial coherence in order to be able to focus the output beam e.g. into an optical fiber. To optimize the spatial coherence, then, means to obtain an output resembling a Gaussian beam to as high an extend as possible. Here we briefly mention a few attempts to tame the beast, after which we will describe the specific external-cavity (EC) setup which we regard in Chapter 5. We divide the schemes into on-chip schemes where advanced semiconductor technology has been used in order to tailor a laser cavity to give a desired stable single-mode output or often a, more realisticly speaking, partly stabilized output, and then EC schemes where there is a finite delay between the output of the BA laser and the field that is fed back to the laser.

2.3.1 On-chip schemes

The α-distributed-feedback laser [15][16] is essentially a BA laser with a single intra-cavity angled grating whose fringes make up a substantial angle with the lazer axis (z-axis). The current stripe is angled parallel to the grating. The grating filters the intra-cavity field spatially and spectrally giving single-mode operation both spatially and spectrally. The output-field is close to being Gaussian and filamentation is well suppressed.

Another on-chip scheme has been demonstrated with broad area lasers having an intracavity spatial phase controller yielding a nearly diffraction-limited single-lobed far-field [17]. In the demonstrated lateral-multi-segment-device, a spatial phase controller could generate an asymmetric lateral variation in the longitudinal optical path length. Pulsed powers of 300 mW were achieved. The authors suggest that a tilted end facet ($\sim$ 1 degree) should have an equivalent effect. We mention this device as it has a built-in lateral asymmetry. The EC laser that we study in Chapter 5 is also asymmetric. The device had a single-lobed far-field off the laser axis. Semiconductor-laser arrays are devices related to BA lasers, which provide an effective method to suppress the filamentation in a wide-aperture laser. Also, a strong competitor to the BA laser as a high-power device are tapered lasers. Practically diffraction-limited tapered lasers with multi-Watt output emerged in the mid-nineties [18].

2.3.2 External cavity schemes

External cavities offer the combination of an delayed optical feedback and optionally a filtering. For twin-stripe lasers the effect of the delay in an external cavity can in specific cases be seen to stabilize what was a chaotic output intensity for the solitary laser to a periodically varying output [19]. For BA lasers with their broad spatial spectrum, some means of spatial filtering is probably necessary to increase the spatial coherence and/or stabilize the dynamic filamentation. Most likely one cannot have the former without the latter at high pump currents. In [20] a spatially filtered feedback by means of a tilted plane mirror was applied and streak-camera measurements show that the filter is able to suppress the dynamic filamentation rather well. Another way to achieve spatial filtering is to use an external reflector with a finite radius of curvature. Such external cavities have produced operation causing a single-lobed far-field of the laser [21] in agreement with theoretical predictions [22] [23]. Phase conjugate feedback without spatial filtering has produced operation in a single longitudinal mode [24]. Even operation in a true single longitudinal and lateral mode has been achieved albeit at low currents using photorefractive feedback [25]. It should be noted that a plane conventional mirror (without any spatial filtering) has been shown not to have any stabilizing effect on the output of a BA laser, nor to bring it to lase in a single longitudinal or lateral mode [24].

2.4 Asymmetric external cavity laser

It has been shown experimentally in [26][27] and through modeling [28] that injection set-ups with a single-mode laser acting as a master oscillator and the BA laser amplifier as the slave, that the best spatial coherence of the output of the slave is achieved when the angle of incidence of the master beam on the front facet of the BA laser is off the laser axis of the BA laser, i.e. the slave. On the contrary, normal incidence ($\theta = 0$) of the master beam causes filamentation in the near-field and a far-field distributed over a large range of angles. It thus appears that locking the fundamental spatial (lateral) mode is difficult to achieve. Considering an external-cavity scheme in which the intention is to force a wide aperture laser to ideally oscillate in a single lateral mode, it makes good sense to enhance lateral modes of the laser that emit light away from the laser axis in the far-field. For this

purpose an asymmetric external cavity (AEC) laser was introduced in 1987 [29]. The original work was done using a wide semiconductor laser array but the behavior of the system holds similar to the case when a BA laser is used as the active part of the system.

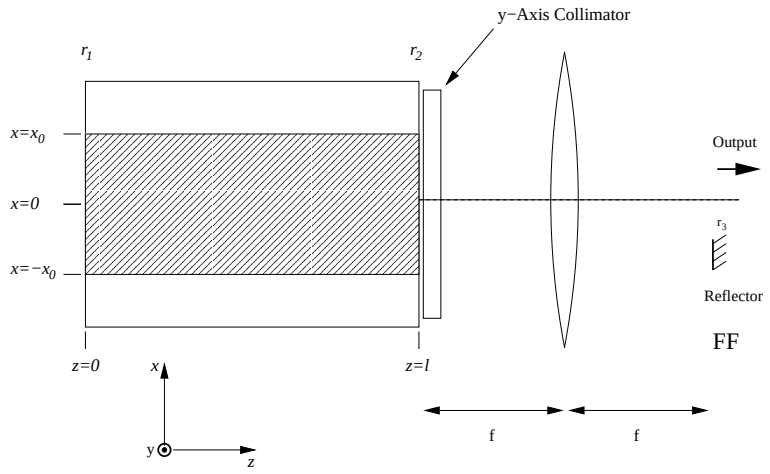

Figure 2.2: Top view of AEC laser. BA laser emits ligth through right facet. Lens of focal length f Fourier transforms the field from the x-domain to the k_x-domain. The far-field (FF) or the Fourier plane is thus at $z = l + 2f$, where the reflector with amplitude reflectivity r_3 acts as a spatial filter (due to its small lateral extend). The part of the field that is reflected due to r_3 is again Fourier transformed to the x-domain. The y-axis collimator (a lens, e.g. a cylindrical lens, of short focal length) collimates the field in the quickly diverging y-direction.

A version of the AEC laser made as simple as possible is presented in Figure 2.2. It is similar to [10]. It consists of a wide aperture laser, within this thesis a BA laser, two lenses, and a reflector (a stripe mirror) with amplitude reflectivity r_3. The field emitted from the right facet of the BA laser with amplitude reflectivity r_2 propagates through the lenses before part of it is reflected by the external stripe-mirror width. A part of the reflected field returns to the right facet through the lenses. Let us describe the system in more detail: Usually one assumes that the output (scalar) field of the solitary BA laser can be written as a product $E^+(x, z = l)\phi(y)$. The y-dependent part of the field is a single-moded and nearly Gaussian profile with negligible phase curvature because of the index guiding of the double

heterostructure in the y-direction [30]. The lens labeled "y-axis collimator", is placed immediately front of the output facet. It can be an e.g. cylindrical lens. It collimates the field along the y-axis and the y-dependence can be disregarded in the external cavity. The collimation is important since the field is quickly divergent in the y-direction. In reality parts of the reflected field will not make back to the right facet because e.g. undesired scattering at the external mirror or misalignments. These losses can from a theoretical point of view be included in the reflectivity r_3. The second lens is placed at $z = l + f$ where f is the focal length of this lens. This means that the this lens performs a spatial Fourier transform on the output field so that at $z = l + 2f$ (the Fourier plane) one obtains the spatial spectrum (the k_x-domain) or the far-field of the output field. At the Fourier-plane the field is filtered and reflected by the external stripe-mirror and due to the return to right facet at $z = l$ through the lens, the field is transformed back to the x-domain. Speaking in broader terms any type of filter can be placed in the Fourier-plane be it symmetric or asymmetric. Also, the lens could also be displaced from $z = l + f$ to obtain a focused feedback [31].

It should be noted that in some reported set-ups, e.g. [10] [32], an aperture was inserted in the output arm as an additional spatial filter. The aim of the aperture is to separate unwanted side lobes from the dominant single-lobe in the far-field (we call the dominant lobe "the single-lobe"). Therefore reported single-lobe output at very high pump currents may have undergone such additional spatial filtering. Figures 2.3 and 2.4 adopted from [33] exemplifies measured time-averaged near- and far-fields of a BA laser. The figures compare the output of the solitary BA laser and the output when the AEC is added. In Figure 2.4 the effect in the far-field is evident: the far-field of the solitary laser is a blurred shape spread over a wide span of angles, typically 2 to 6 degrees depending on the device and pump current. When the AEC is added and optimized one sees a dominant single-lobe. The single-lobe is seen to be to the left of the optical axis. In this case the stripe mirror is placed to the right of the optical axis. For a 200 μm-wide BA AlGAas-device pumped at 2 times threshold the single-lobe of the AEC laser can be located around 2 degrees off the optical axis in the far-field [34]. In order to obtain a measurement as the one in Figure 2.4 showing the entire far-field, one must insert a beam splitter just before the external mirror. If one measures the output after the external mirror, one will only (or mainly) see the single-lobe. The near-field in Figure 2.3 shows that the effect of the external mirror is to tilt the near-field. One can say that the near-field tilts in the same direction

as the far-field.

AEC lasers with external cavities including a grating as the reflector [35] and a grating as a reflector in combination with a Fabry-Perot etalon [36] have been shown to considerably narrow the emission spectrum while also improving the spatial coherence. The spectra were narrowed from around 1 nm less than 0.1 nm around 810 nm. For AEC lasers with a conventional stripe-mirror, on the other hand, the spectral width of the freely running BA lasers is not reduced significantly [37]. From a theoretical point of view, it is of interest whether an AEC laser with a mirror reflector operates in a single, stable, lateral mode or in some time dependent state. Our calculation presented in Chapter 5 implies that the latter is the case.

In high power laser technology, often the spatial coherence is of greater concern than the temporal coherence. A measure of spatial coherence often used in connection with high-power lasers is the M^2-factor. It expresses the similarity between a regarded output field of a laser with a Gaussian beam. The Gaussian has same width as the regarded field at its waist [38]. The M^2-factor appears to make most sense at values that are not vastly greater than 1. The beam quality of the single lobe in the far-field of a AEC laser may be measured using M^2. When pumped far above threshold, the M^2 of AEC lasers degrades for increasing pump currents. Hence, a compromise between high output power and low M^2 must be made in high-power applications. We will not discuss the M^2-factor further.

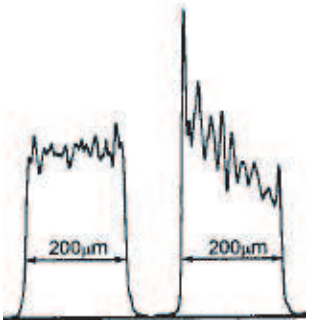

Figure 2.3: Measured near-field of solitary laser (left) and AEC laser (right). The device was a BA laser with a 200 μm-wide current stripe running at 810 nm. Adopted from [33].

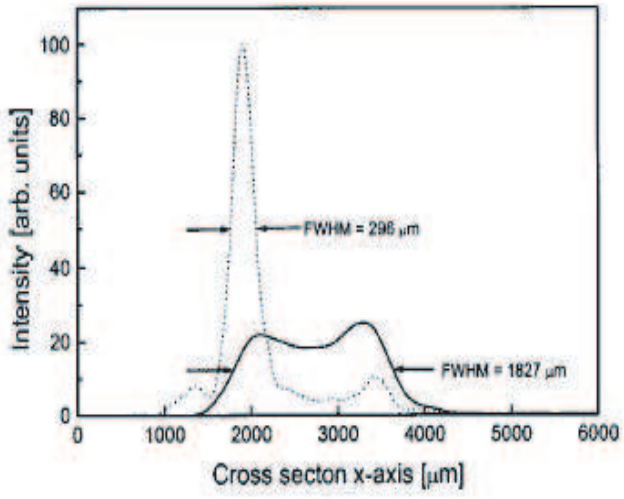

Figure 2.4: Measured far-field of solitary laser (full line) and AEC laser (dotted line). Same case as Figure 2.3. Note that the abscissa-unit is length and not angle as it is common for the far-field. The optical axis ($\theta = 0$) is around 2700 μm. The stripe mirror is located around 3500 μm, i.e. opposite the dominant single-lobe. Adopted from [33].

2.5 Theory and modeling of BA lasers

From approximately 1990 until today, mainly two paths have been followed to model BA lasers. Those are the beam propagation method (BPM) and time-domain calculations by integration of time dependent partial differential equations (PDEs).

BPM is a method to find stationary field distributions by propagating a field back and forth in the laser cavity, while considering the coupling between the intensity of the field and the semiconductor, until a steady state has been obtained. Its main quality is that it gives 2-dimensional laser modeling (as opposed to 1-dimensional) at low computational cost. We have implemented BPM both with and without the external cavity of the AEC laser. As it was also found in [1] we have found it problematic for the method to find steady states except for at very low pump currents, especially when including an external cavity in the system. Supposedly this problem is due to the difference in time scales of the optical and carrier rate equations [1]. Moreover, the

steady state which BPM may find depends on the trial field that is initially launched into the system. Since the field is propagated back and forth in the cavity the effect of filamentation interferes with the aim of finding stationary solution. An amusing example of the effect of filamentation on BPM can be found in [30] where the linewidth enhancement factor α was simply set to zero in order to get stationary results for a BA laser in an external cavity. With $\alpha = 0$ there is no self-focusing, and hence no filamentation. We have not found BPM suited for our purposes. When modeling BA amplifiers (not lasers) [39], in conjunction with injection locking of BA lasers [28], or for index-guided devices such as tapered lasers [40], BPM may work well.

When recognizing the very complex fluctuations in time and space of BA lasers and desiring to be able to compare theory with experiment at considerable pump currents it becomes advantageous to use a time-domain method. In fact one cannot expect stationary solutions to be found in measurements at high currents. While treating the field of the laser classically, different levels of describing the semiconductor gain material have been regarded. A phenomenological description using linear gain and the α-parameter is an "obvious" possibility [41]. However, as we find in Chapter 5 the phenomenological model causes some problems in a spatially extended system where the diffraction of the field has to be included. Fortunately, one can modify the equations slightly to overcome the problem. Microscopic models using the semiconductor Maxwell-Bloch equations [3][4] have been the other extreme at least for bulk BA lasers. In most cases known to us the numerical apparatus upon which the time-domain approaches rely, regardless of the level of describing the semiconductor, is the hopscotch method, a method to integrate parabolic PDEs. Implementations including 2 and 1 spatial dimensions have been presented. In Chapter 5 we use a 1-dimensional implementation of the hopscotch method with a phenomenological description of the semiconductor. This has been computationally highly advantageous since all our numerical calculations have been performed on a laptop computer. To work in one spatial dimension we use a mean-field approxiamtion when deriving equations in Chapter 3, implying that we average over the longitudinal direction z.

Of course one can choose other paths than the two described above. Within other types of lasers such as lateral single-mode EC lasers and distributed feedback (DFB) lasers there has been a great tradition of finding stationary solutions of the given system and then investigating their small

signal properties. For example for a lateral single-mode EC laser, under certain feedback conditions, the stationary solutions of the laser may be located on an ellipse in the (frequency, threshold-gain)-plane [42]. Half of the stationary solutions are found to be unstable when subject to a stability analysis, and the laser may choose to lase in only one of the solutions on the ellipse or perhaps the lasers chooses a chaotic state, but this does not mean that the existence of the ellipse is uninteresting. Based on these considerations we find stationary lateral modes in a BA laser in Chapter 3 and perform a small signal analysis of some of the found modes in Chapter 4. Since a BA laser is known to operate in a fluctuating possibly chaotic state when driven at considerable currents, our analysis is of a theoretical character. The method we use to obtain stationary solutions resembles finding bound states in a scattering potential. Again, there are several lateral modes in a BA laser for one pump current. With BPM this multitude of lateral modes would be extremely difficult to come about since the solution to which BPM settle, is dependent on a x-dependent trial field injected from one end of the laser when initiating the iteration.

Further, in order to disassemble the nonlinear effects perturbing the field near threshold we introduce a modal-expansion technique that allows for an easy interpretation in Chapter 6.

Chapter 3

Theory of stationary lateral modes in Broad area lasers

In this chapter we first formulate the equations which form the basis of the results presented in this thesis. The derived equations describe the lateral field distribution and the lateral carrier density distribution of a BA laser. To study the lateral mode structure in detail we have chosen to reduce the, in principle, 3+1 dimensional problem to a 1+1 dimensional problem. We then combine the field and carrier density to a single, nonlinear equation for stationary solutions following Lang *et al.* [1].

Secondly, we calculate stationary lasing solutions. Here, a stationary solution is the combination of an oscillation frequency ω_s, a stationary lateral field distribution $E_s(x)$, and a stationary lateral carrier-density distribution $N_s(x)$. We have found a wide variety of modes in addition to known gain guided modes. It turns out that modes with asymmetric field distributions exist despite the symmetric lateral structure under investigation. Furthermore the stationary solutions yield a beautiful pattern of tuning curves which possess a systematic structure in their interrelationship and bifurcation behavior. Tuning curves are curves in the current-frequency plane.

As discussed in Chapter 2 one cannot, in general, expect that calculated stationary modes will agree with measurements. Stationary solutions may not be stable, and one must at least investigate the stability properties of given modes before discussing their conceivable role in an experiment. We investigate stability properties of the stationary solutions in Chapter 4.

3.1 Derivation of equations using the mean field approximation

We now derive a set of equations for the field distribution and the carrier density. We choose to employ a mean field approximation which implies averaging over the longitudinal direction of the laser. We assume that the laser operates in a TE mode. The scalar wave equation in the time-domain is given as [43][44]

$$\nabla^2 \mathscr{E} - \frac{\sigma}{\epsilon_0 c^2}\frac{\partial}{\partial t}\mathscr{E} - \frac{1}{c^2}\frac{\partial^2}{\partial t^2}\mathscr{E} = \frac{1}{\epsilon_0 c^2}\frac{\partial^2}{\partial t^2}(\mathscr{P} + p), \tag{3.1}$$

where ω is the angular frequency. The real scalar electric field $\mathscr{E}(x, y, z, t)$ induces the polarization field $\mathscr{P}(x, y, z, t)$. The material losses are included in the conductivity σ. Spontaneous emission is included in the term p. c is the speed of light in vacuum and ϵ_0 is the vacuum permittivity. The Fourier transforms are defined as

$$\mathscr{E}_\omega(x, y, z) = \int_{-\infty}^{\infty} \mathscr{E}(x, y, z, t) e^{-j\omega t} \tag{3.2}$$

$$\mathscr{E}(x, y, z, t) = \frac{1}{2\pi}\int_{-\infty}^{\infty} \mathscr{E}_\omega(x, y, z) e^{j\omega t}. \tag{3.3}$$

In the frequency domain Eq. (3.1) becomes

$$\nabla^2 \mathscr{E}_\omega - j\omega\frac{\sigma}{\epsilon_0 c^2}\mathscr{E}_\omega + \frac{\omega^2}{c^2}\mathscr{E}_\omega = -\frac{\omega^2}{\epsilon_0 c^2}(\mathscr{P}_\omega + p_\omega). \tag{3.4}$$

For single-mode semiconductor lasers it has been a vast success to assume that the polarization relaxes in time scales much faster than the time scales of the other variables in the problem, the field and the distribution functions of the charge carriers. If one adiabatically eliminates the polarization variable in the semiconductor Maxwell-Bloch equations (see [45] for the case of a semiconductor BA laser) then

$$\mathscr{P}_\omega = \epsilon_0 \chi_\omega(x, y, z)\mathscr{E}_\omega(x, y, z) \tag{3.5}$$

where the susceptibility $\chi_\omega(x, y, z)$ is related to the permittivity $\epsilon_\omega(x, y, z)$ through

$$\epsilon_\omega(x, y, z) = 1 + \chi_\omega(x, y, z) - j\frac{\sigma}{\epsilon_0 \omega}. \tag{3.6}$$

Using Eqs. (3.5) and (3.6) in (3.4) yields

$$\left[\nabla^2 + \frac{\omega^2}{c^2}\epsilon_\omega(x,y,z)\right] E_\omega(x,y,z) = F_\omega(x,y,z), \tag{3.7}$$

with

$$F_\omega(x,y,z) = -\frac{\omega^2}{\epsilon_0 c^2} p_\omega(x,y,z). \tag{3.8}$$

We now show how the problem of solving the 3+1 dimensional scalar wave equation can be reduced to solving a 1+1 dimensional wave equation by applying a weighted mean field approximation. We assume that the electric field in the BA-laser waveguide in the frequency domain is of the form

$$\mathscr{E}(x,y,z,\omega) = E_\omega^+(x,z)\phi(y)e^{-j\beta z} + E_\omega^-(x,z)\phi(y)e^{j\beta z}. \tag{3.9}$$

$E_\omega^+(x,z)$ and $E_\omega^-(x,z)$ are field envelopes describing forward and backward traveling waves in the longitudinal direction. They are assumed to be slowly varying functions of z. We intend to study lateral modes for a given longitudinal mode. The propagation constant β is therefore chosen to satisfy the longitudinal oscillation condition for a Fabry-Perot laser

$$r_1 r_2 \exp(-2j\beta l) = 1 \tag{3.10}$$

where r_1 and r_2 are the left and right facet reflectivities (see Figure 2.1). The function $\phi(y)$ describes the transverse field distribution and is taken to be normalized to unity, i.e $\int \phi(y)\phi^*(y)dy = 1$. Inserting (3.9) in the scalar wave equation (3.7) and neglecting the second order z-derivatives leads to

$$\phi\frac{\partial^2}{\partial x^2}E_\omega^\pm + E_\omega^\pm\frac{\partial^2}{\partial y^2}\phi \mp 2j\beta\phi\frac{\partial}{\partial z}E_\omega^\pm - \beta^2 E_\omega^\pm\phi + k_0^2\epsilon_\omega(x,y,z)E_\omega^\pm\phi = F_\omega^\pm, \tag{3.11}$$

where $k_0 = \omega/c$ is the vacuum wavenumber. By standard procedure we separate into a transverse field equation

$$\frac{\partial^2}{\partial y^2}\phi + k_0^2\epsilon_\omega(x,y,z)\phi = k_{eff}^2\phi \tag{3.12}$$

and the in-plane field equations for $E_\omega^\pm(x,z)$

$$\frac{\partial^2}{\partial x^2}E_\omega^\pm \mp 2j\beta\frac{\partial}{\partial z}E_\omega^\pm + (k_{eff}^2 - \beta^2)E_\omega^\pm = f_\omega^\pm, \tag{3.13}$$

where

$$f_\omega^\pm(x,z) = \int_{-\infty}^{\infty} F_\omega(x,y,x)\phi^*(y)dy e^{\pm j\beta z}\,. \tag{3.14}$$

The eigenvalue equation (3.12) determines the fundamental transverse mode $\phi(y)$ and the corresponding effective wave number $k_{eff}(x,z,\omega)$. We ignore the weak dependence of ϕ on x. The effective wavenumber is related to the complex effective refractive index by $k_{eff}(x,z) = n_{eff}(x,z)(2\pi/\lambda_r)$ where λ_r is a reference wavelength [43] [46]. $n_{eff}(x,z)$ can be obtained by treating the loss and pump dependent part of $\epsilon_\omega(x,y,z)$ in (3.12) using first order perturbation theory yielding a real pump independent effective index n_r and a confinement factor

$$\Gamma = \frac{\int_{active\ layer} |\phi(y)|^2 dy}{\int_{-\infty}^{\infty} |\phi(y)|^2 dy}. \tag{3.15}$$

In (3.15) it has been assumed that the internal loss in the cladding layers are the same as in the core layer. The mean field approximation deals with averages over the z-coordinate; an averaged variable is denoted by putting a bar over the variable. Thus

$$\overline{E_\omega^\pm}(x) = \frac{1}{l}\int_0^l E_\omega^\pm(x,z)dz\,. \tag{3.16}$$

The longitudinal average of (3.13) yields the equations

$$\frac{\partial^2}{\partial x^2}\overline{E_\omega^\pm} \mp \frac{2j\beta}{l}(E_\omega^\pm(x,l) - E_\omega^\pm(x,0)) + (\overline{k_{eff}^2} - \beta^2)\overline{E_\omega^\pm} = \overline{f_\omega^\pm} \tag{3.17}$$

where we have assumed that [47]

$$\overline{k_{eff}^2 E_\omega^\pm} = \overline{k_{eff}^2}\,\overline{E_\omega^\pm}\,. \tag{3.18}$$

The envelope fields $E_\omega^\pm$ obey the boundary conditions

$$E_\omega^+(x,0) = r_1 E_\omega^-(x,0) \tag{3.19}$$

$$E_\omega^-(x,l) = r_2 e^{-j2\beta l} E_\omega^+(x,l) \tag{3.20}$$

at the two end facets. With β satisfying (3.10) we find that (3.17), (3.19) and (3.20) lead to the equation

$$\frac{\partial^2}{\partial x^2}E_\omega + (k^2 - \beta^2)E_\omega = f_\omega \tag{3.21}$$

for the weighted field and noise functions $E_\omega(x)$ and $f_\omega(x)$ given by

$$E_\omega = \frac{1}{\sqrt{2r_1}}(\overline{E_\omega^+} + r_1\overline{E_\omega^-}) \tag{3.22}$$

$$f_\omega = \frac{1}{\sqrt{2r_1}}(\overline{f_\omega^+} + r_1\overline{f_\omega^-})\,. \tag{3.23}$$

Also we have defined k by $k^2 \equiv \overline{k_{eff}^2}$.

The frequency domain equation (3.21) can be transformed to a time domain field equation for the complex field envelope $E(x,t)$ defined by

$$E(x,t)e^{j\omega_s t} = \frac{1}{2\pi}\int_0^\infty E_\omega(x)e^{j\omega t}d\omega, \tag{3.24}$$

where ω_s is the optical frequency of the lateral mode under consideration. If $E_\omega^\pm$ are independent of z, the average photon density in the active layer is given as

$$S(x) = B|E(x,t)|^2 \tag{3.25}$$

with the constant of proportionality [48]

$$B = \frac{2\epsilon_0 n_r n_g}{\hbar\omega h}K \tag{3.26}$$

where K is the longitudinal Peterman-factor [49]

$$K = \frac{(r_1+r_2)(r_1r_2-1)}{2r_1r_2 ln(r_1r_2)}\,, \tag{3.27}$$

and where we have used that the confinement factor Γ is approximately equal to $h|\phi(0)|^2$ with h being the thickness of the active layer. Details are given in Appendix A. For most practical cases the factor K is close to one. n_r is the real passive part of the effective index and n_g is the group index. We will assume that (3.26) is a useful approximation even when longitudinal spatial hole burning makes the field envelope $E_\omega^\pm$ dependent on z.

Solving for β in Eq. (3.10) yields

$$\beta = \frac{\pi p_l}{l} + j\frac{\alpha_m}{2} \tag{3.28}$$

where p_l is an integer denoting the longitudinal mode number and α_m is the distributed mirror loss

$$\alpha_m = -\frac{1}{l}\ln(r_1r_2). \tag{3.29}$$

As we regard only one longitudinal mode we set the real part of (3.28) equal to a reference wave number k_r

$$k_r = \frac{\omega_r}{c} n_r, \tag{3.30}$$

where $\omega_r = 2\pi c/\lambda_r$ is a corresponding reference frequency. When there is no lateral, passive index guiding present in the laser structure, n_r is independent of x. Therefore,

$$\beta = k_r + j\frac{\alpha_m}{2}. \tag{3.31}$$

Taking the square of (3.31) gives approximately

$$\beta^2 \simeq k_r^2 + jk_r\alpha_m. \tag{3.32}$$

The z-averaged effective wave number $k(x)$ may be given the as a function of ω and z-averaged carrier density $N(x)$ [50]:

$$k(x) = \frac{\omega}{c} n(\omega, N(x)) + j\frac{1}{2}\left[g(\omega, N(x)) - \alpha_i\right]. \tag{3.33}$$

Here $n(\omega, N(x))$ is the modal index, g is the modal gain, and α_i is the internal loss all of which are averaged over z. The internal loss includes losses caused by scattering of light at surfaces or at crystal defects, and by free carrier absorption. For the modal gain we assume a simple linear model without any spectral dependence:

$$g \equiv g(\omega_r, N(x)) = \Gamma a(N(x) - N_0). \tag{3.34}$$

Here a is the differential material gain and N_0 is a reference carrier density. The relation between the modal gain and the material gain g_m is $g = \Gamma g_m$. We expand the complex propagation constant around the reference frequency ω_r and the transparency carrier density $N_r = N_0 + \alpha_i/(\Gamma a)$ to first order:

$$k(x) = k_r + \frac{\partial k}{\partial \omega}(\omega - \omega_r) + \frac{\partial k}{\partial N}(N(x) - N_r). \tag{3.35}$$

The gain in general also depends upon intensity through processes such as spectral hole burning and carrier heating. This effect of nonlinear gain may be included by adding an expansion term in (3.35) proportional to the intensity. Normally, the expansion coefficient is negative since high intensity tends to suppress the gain. Nonlinear gain is relevant at high powers. Modeling of

BA lasers using BPM has commonly implied use of linear gain models e.g. [30] [31]. Imitating a quantum-well gain with a nonlinear dependence on the carrier density has also been used in conjunction with BPM [51]. A trend in the modern literature on time-domain methods for BA lasers is to rely on a microscopic treatment [3][4] of the gain material using the semiconductor Maxwell-Bloch equations to describe spectral hole burning such that no phenomenological expression for the gain is needed nor is the introduction of the α-parameter described below. We shall see in Chapter 5 that the adiabatic elimination performed in connection with (3.5) has consequences for a system that includes diffraction of the field. By disregarding the frequency dependence of the gain, the direct-gap semiconductor is reduced to a two-level system without spectral broadening [45]. It is assumed that the charge carriers of the semiconductor are in equilibrium, whereby excited electrons are mainly found at the bottom of the conduction band of the direct bandgap semiconductor material. All events of generation and recombination of electron-hole pairs are hence assumed for carriers of zero wavenumber. In reality, the carriers are not in thermal equilibrium in a semiconductor laser. Furthermore, a linear dependence of the gain upon the carrier density is assumed, neglecting the effect of gain saturation at high pumping rates. In this thesis, we shall not consider cases for currents $I > 1.2I_0$, where I_0 is the approximate threshold current. The reader may find a pump current 20% above the threshold current rather modest. However, in a BA laser, at currents just above threshold, instabilities set in as we shall see in Chapters 4 and 5. Here, the two expansion coefficients in (3.35) are taken to be

$$\frac{\partial k}{\partial \omega} = 1/v_g, \tag{3.36}$$

where $v_g = c/n_g$ is the group velocity, and

$$\frac{\partial k}{\partial N} = \frac{1}{2}\Gamma a(j - \alpha). \tag{3.37}$$

Here α is Henry's linewidth enhancement factor [52] giving the coupling between the real and imaginary parts of the carrier-induced refractive index changes. The linewidth enhancement factor in BA lasers has experimentally been seen to vary with carrier density and wavelength [53]. One could include this by adding higher order terms in the expansion of the wavenumber in (3.35). This, of course, urges that higher order expansion coefficients are available from measurements.

We move on to obtain our desired field equation. The square of k is given as

$$k^2(x) \simeq k_r^2 + 2k_r \left[\frac{\partial k}{\partial \omega}(\omega - \omega_r) + \frac{\partial k}{\partial N}(N(x) - N_r) \right], \tag{3.38}$$

when neglecting the terms quadratic in $\partial k/\partial\omega$ or $\partial k/\partial N$. We can now write the field equations for $E_\omega(x)$ using Eqs. (3.32) and (3.38) in (3.21)

$$\frac{\partial^2}{\partial x^2} E_\omega + 2k_r \left[\frac{\partial k}{\partial \omega}(\omega - \omega_r) + \frac{\partial k}{\partial N}(N(x) - N_r) - j\frac{\alpha_m}{2} \right] E_\omega = f_\omega. \tag{3.39}$$

The field equation in the time-domain becomes

$$\left\{ \frac{\partial^2}{\partial x^2} - j\frac{2k_r}{v_g}\frac{\partial}{\partial t} + 2k_r \left[\frac{\partial k}{\partial \omega}(\omega_s - \omega_r) + \frac{\partial k}{\partial N}(N(x,t) - N_r) - j\frac{\alpha_m}{2} \right] \right\} E(x,t) = f(x,t). \tag{3.40}$$

We may define $\kappa(x,t)$

$$\kappa(x,t) = 2k_r \left[\frac{\partial k}{\partial \omega}(\omega_s - \omega_r) + \frac{\partial k}{\partial N}(N(x,t) - N_r) - j\frac{\alpha_m}{2} \right] \tag{3.41}$$

such that (3.40) becomes

$$\left[\frac{\partial^2}{\partial x^2} - j\frac{2k_r}{v_g}\frac{\partial}{\partial t} + \kappa(x,t) \right] E(x,t) = f(x,t). \tag{3.42}$$

The noise function $f(x,t)$ is obtained from $f_\omega(x)$ via a transformation similar to (3.24).

Next, we must address the z-averaged carrier density. The mean field carrier equation stated in the time-domain reads

$$\frac{\partial}{\partial t} N(x,t) = \mathscr{J}(x,t) + D\frac{\partial^2}{\partial x^2} N(x,t) - \frac{N(x,t)}{\tau_R} - v_g g_m(x,t) S(x,t). \tag{3.43}$$

Here $\mathscr{J}(x,t)$ is the pump rate and D is the ambipolar diffusion coefficient. We assume that the pump rate is the sum $\mathscr{J}(x,t) = J_s(x) + \delta J(x,t)$ of a stationary pump rate $J_s(x)$ and a small modulation-term $\delta J(x,t)$. In the transverse y-direction the double heterostructure limits the diffusion of charge carriers wherefore it is negligible in this direction. In the carrier equation, recombination of electron-hole pairs via processes other than stimulated emission has been described through

$$R(N) = \frac{N}{\tau_R}, \tag{3.44}$$

where the carrier lifetime τ_R is assumed constant. Several recombination mechanisms have thus been lumped together in the rate $1/\tau_R$. They are spontaneous emission, nonradiative emission, and possibly transverse leakage of carriers out of the active layer [54]. A more precise expression for $R(N)$ involves a linear, a quadratic, and a cubic term in N.

We do not to include temperature effects in the analysis. For high pump rates the lateral temperature profile can certainly perturb the wave-guiding properties of wide-aperture lasers [55]. A rise in temperature augments the real part of the refractive index, which in turn causes thermal lensing. In modeling this is normally included by introducing a thermal index coefficient, which serves as a constant of proportionality between the temperature distribution and the thermally induced change in the real refractive index. The temperature distribution can be found by solving the heat equation [40] or simply by assuming a known temperature distribution [56]. In a more rigorous setting, the temperature affects microscopic properties, e.g. changes the bandgap of the active semiconductor, which in turn affects the macroscopic optical properties [57]. Actual devices are mounted with heat sinks, and in experiments thermal effects are often avoided by a slow temporal modulation of the pump current allowing for periodic cooling of the chip [20]. We shall assume that temperature effects are negligible in our calculations.

3.2 A single nonlinear field equation

In time-averaged measurements the near-fields of BA lasers can often be found to consist of a pedestal with a more or less regular ripple superimposed on top, see Figure 2.3 or e.g. [58]. That is to say that the near-fields are not deeply modulated in the way a truncated sinusoidal is. Perhaps motivated by such measurements Mehuys *et al.* [14] assumed a field solution of the form $E(x) = E_0 \exp(a(x) + j\phi(x))$ underneath the metal contact with $a(x) \ll 1$ and $\phi(x)$ being real functions. Analytical approximate calculations involving linearizations give near-fields in rather good quantitative agreement with some experiments at high currents. However, their starting point may be questionable because a solitary BA laser operating at high pump currents is not in a steady state. Measured near-fields that are only moderately and not strongly spatially modulated are most likely a result of time-averages over multi-lateral mode operation or alternatively a highly nonlinear (possibly chaotic) lateral variation in time and space. On the other hand, one can not

rule out that stationary solutions leave traces in time-averaged measurements and from a fundamental point of view it is of interest to know about the stationary solutions of a physical system.

In order to perform a comprehensive study of the lateral modes structure of a BA laser and in addition to investigate stability properties as described in the subsequent chapter, it is very helpful to derive a single equation that includes both the field and the carrier density [1]. The derivation is done under the assumption that carrier diffusion is negligible. This assumption is argued for in [14]: The approximation is good as long as the condition of $k_{lat}^2 L_D^2 \ll 1$ is fulfilled; k_{lat} is the lateral wavenumber and $L_d = \sqrt{D\tau_R}$ is the diffusion length. However, our main reasons to exclude diffusion are given in the following.

Our two main motivations to work with a single equation are: Firstly, in the present chapter we shall show a series of newly found stationary solutions. We have searched for them like searching for needles in a haystack, notably needles whose existence we *a priori* were not aware of. Therefore a convenient computational environment has been a great advantage. Secondly, in Chapter 4 we study the small signal properties of some of the calculated stationary solutions. The mathematical apparatus derived there becomes rather complicated even without diffusion so leaving it out (for now) has been practical. By no means, however, do we rule out the significance of lateral carrier diffusion. In Chapter 5 the carrier diffusion is reintroduced in time-domain calculations and in Chapter 6 also in stationary calculations.

Here we look for staionary solutions ($E_s(x)$, $N_s(x)$, ω_s). Stationary solutions are found as solutions to Eqs. (3.42) and (3.43) for a steady pump term $\mathscr{J} = J_s(x)$ and for $f(x,t) = 0$. Upon neglecting the carrier diffusion

$$N_s(x) - N_0 = \frac{J_s(x)\tau_R - N_0}{1 + |E_s(x)|^2/P_{sat}} \tag{3.45}$$

where

$$P_{sat} = \frac{\hbar\omega h}{2\epsilon_0 n_r c\Gamma a\tau_R K}. \tag{3.46}$$

In obtaining (3.46), Eq. (3.26) was used. The field $E_s(x,t)$ is seen to be in units $\mathrm{V}/\sqrt{\mathrm{m}}$. . Utilization of (3.45) in Eq. (3.41) leads to a single nonlinear

equation, namely

$$\left\{\frac{\partial^2}{\partial x^2}+2k_r\left[\frac{\partial k}{\partial\omega}(\omega_s-\omega_r)+\frac{\partial k}{\partial N}\frac{J_s(x)\tau_R-N_0}{1+|E_s(x)|^2/P_{sat}}-j\frac{\alpha_i+\alpha_m}{2}+\frac{\alpha\alpha_i}{2}\right]\right\}E_s=0. \tag{3.47}$$

Note that the output power scales linearly with P_{sat}. The second part of the operator in (3.47) we define as

$$\kappa_s(x)=2k_r\left[\frac{\partial k}{\partial\omega}(\omega_s-\omega_r)+\frac{\partial k}{\partial N}\frac{J_s(x)\tau_R-N_0}{1+|E_s(x)|^2/P_{sat}}-j\frac{\alpha_i+\alpha_m}{2}+\frac{\alpha\alpha_i}{2}\right] \tag{3.48}$$

and the field equation may simply be written

$$\left[\frac{\partial^2}{\partial x^2}+\kappa_s(x)\right]E_s=0. \tag{3.49}$$

Let the field be defined on the interval $-A\leq x\leq A$. We must specify the boundary conditions. At a position on the x-axis that is sufficiently far away from the metal contact for the intensity to become negligible, Eq. (3.49) can be approximated to

$$\left[\frac{\partial^2}{\partial x^2}+\kappa_{\mathrm{WKB}}(x)\right]E_s=0, \tag{3.50}$$

with

$$\kappa_{\mathrm{WKB}}=2k_r\left[\frac{\partial k}{\partial\omega}(\omega_s-\omega_r)+\frac{\partial k}{\partial N}(J_s(x)\tau_R-N_r)-j\frac{\alpha_m}{2}\right]. \tag{3.51}$$

For a slowly varying $J_s(x)$, one obtains the solution

$$E_s(x)=E_0\exp(\pm j\sqrt{\kappa_{\mathrm{WKB}}}x). \tag{3.52}$$

where E_0 is a real constant. Assume that (3.50) is valid at $\pm A$. Then at $x=\pm A$ the proper signs must be chosen to ensure a solution for the field that decays exponentially when moving away from the metal contact. This gives us the derivatives at $x=-A$

$$\frac{\partial E_s}{\partial x}=j\sqrt{\kappa_{\mathrm{WKB}}}E_s(x) \tag{3.53}$$

and

$$\frac{\partial E_s}{\partial x}=-j\sqrt{\kappa_{\mathrm{WKB}}}E_s(x) \tag{3.54}$$

at $x=A$. We use Eqs. (3.52), (3.53), and (3.54) in the following to specify boundary conditions.

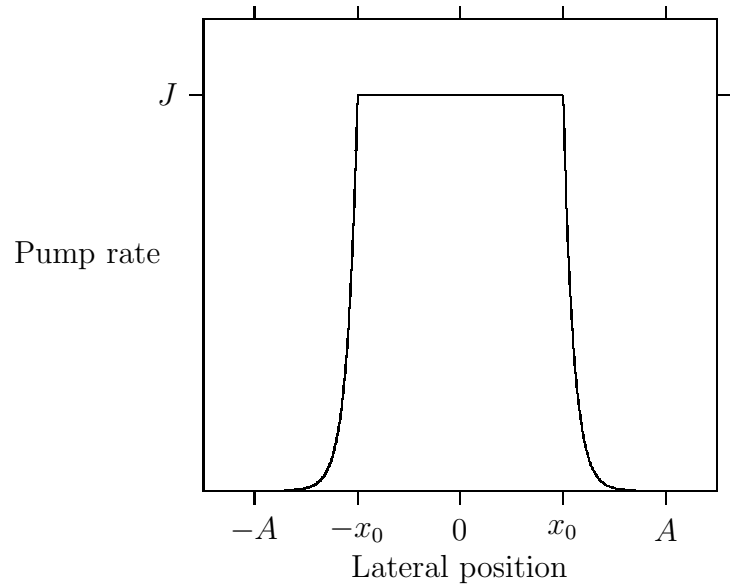

Figure 3.1: Lateral distribution of pump rate. The points $-A$ and A are boundary points

.

3.2.1 Current spreading

We must specify the profile of the pump rate $J_s(x)$. The pump rate is assumed to decay exponentially away from the current stripe, i.e.

$$J_s(x) = \begin{cases} J\exp((x+x_0)/d) & \text{for } x < -x_0 \\ J & \text{for } |x| < x_0 \\ J\exp(-(x-x_0)/d) & \text{for } x > x_0. \end{cases} , \tag{3.55}$$

where J is the pump rate underneath the metal contact and d is a current decay constant. The profile is illustrated in Figure 3.1.

As a unit for the pump rate we introduce J_0. J_0 is the approximate threshold pump rate for the lowest order lateral mode:

$$J_0 = \frac{1}{\tau_R}\left[N_r + \frac{1}{\Gamma a l}\ln\left(\frac{1}{r_1 r_2}\right)\right]. \tag{3.56}$$

The relation between pump rate and current I is $I = qVJ$ where q is the elementary charge and V is the volume of the active region so that $V = 2x_0hl$.

We use the terms pump rate and current interchangeably when distinction is not important.

The idea of the form of $J_s(x)$ is that below threshold but above transparency, the lateral spontaneous emission profile can be measured. Presuming that the intensity distribution due to spontaneous emission is proportional to the carrier density, the decay of carrier density away from the pumped region may be fitted to an exponentional decay while using (3.45) with $|E(x)|^2 = 0$ to obtain d [1]. When including the lateral carrier diffusion, it is common to let the diffusion spread the carrier density outside the pumped region. We do this in the next chapter. To obtain the carrier-density distribution in the active region in a more self-consistent way, procedures involving e.g. the Poisson equation can also be pursued [40][59]. The way one treats the current spreading may certainly affect the obtained output field [60].

Solutions of the nonlinear field equation (3.49) with the profile of the pump rate (3.55) are now to be solved using numerical methods described in the next section.

3.3 Numerical procedures for calculation of modes

With the nonlinear differential equation along with boundary conditions given below, we have a boundary value problem, which must be solved through iterative methods.

3.3.1 Solutions with definite parity

Solutions for which $|E_s(-A)| = |E_s(A)|$ and either $E_s(0) = 0$ or $dE_s(0)/dx = 0$ possess definite parity. For such solutions we employ the numerical procedure of [1]. Due to the finite parity of the field distribution it is only necessary to calculate the field on $-A \leq x \leq 0$. With an initial guess of a real vector $(E_{0,L}, \omega_s)$ the values of field and slope at $x = -A$ become

$$E_s(-A) = E_{0,L} \exp(-j\sqrt{\kappa_{\mathrm{WKB}}}A), \tag{3.57}$$

$$\frac{\partial E_s}{\partial x} = j\sqrt{\kappa_{\mathrm{WKB}}}E_s(-A). \tag{3.58}$$

By (3.49), the field is propagated to $x = 0$ where it is evaluated. A Runge-Kutta method is used for this [61]. When searching for a symmetric solution, $dE_s(0)/dx = 0$ is demanded while for an antisymmetric solution $E_s(0) = 0$ must be fulfilled. From the complex value of $E_s(0)$ or $dE_s(0)/dx$, a Newton-Raphson routine suggests corrections to the values of $(E_{0,L}, \omega_s)$. With corrected $(E_{0,L}, \omega_s)$, the field is again propagated from $x = -A$. This iterative process is repeated until $(E_{0,L}, \omega_s)$ has converged and a stationary solution $(E_s(x), \omega_s)$ is obtained by joining the appropriate part of $E_s(x)$ on $0 < x \leq A$.

3.3.2 Asymmetric solutions

Definite-parity solutions of nonlinear equations of the type $\triangle u(x) + s(u(x))$ can, depending on the function s and the imposed boundary conditions sometimes be shown to bifurcate into asymmetric solutions [62]. Asymmetric solutions are field distributions, which do not possess definite parity. In this case $|E_s(-A)|$ and $|E_s(A)|$ are in general not equal. Then, one must in this case calculate the field distribution on the entire domain $-A \leq x \leq A$. We split the field into two parts. One part is propagated from $x = -A$ with "initial conditions"

$$E_s(-A) = E_{0,L} \exp(-j\sqrt{\kappa_{\mathrm{WKB}}}A). \tag{3.59}$$

$$\frac{\partial E_s}{\partial x} = j\sqrt{\kappa_{\mathrm{WKB}}}E_s(-A) \tag{3.60}$$

to some point x_1 which satisfies $A < x_1 < A$. The other part is propagated from the right ($x = A$) with

$$E_s(A) = E_{0,R} \exp(-j\sqrt{\kappa_{\mathrm{WKB}}}A). \tag{3.61}$$

$$\frac{\partial E_s}{\partial x} = -j\sqrt{\kappa_{\mathrm{WKB}}}E_s(A) \tag{3.62}$$

also to x_1. Let $E_{0,R}$ be a complex constant. At $x = x_1$ we require the complex field and its derivative to be continuous. This requirement renders a total of four conditions. A four-dimensional Newton's method gives corrections to the four unknowns. A solution is found when the iteration converges to give the four unknowns $(\omega_s, E_{0,L}, \mathrm{Re}(E_{0,R}), \mathrm{Im}(E_{0,R}))$. The stationary solution is obtained by connecting the left and the right parts of the field which share the frequency ω_s.

For definite-parity modes and in particular for asymmetric modes it is crucial to have good initial guesses to obtain convergent solutions. With insufficiently good initial guesses either no solutions are found or the solver jumps to a solution far away form the wanted solution in case its existence is known in advance.

3.3.3 Parameter values

Table 3.1: List of parameter values

Parameter	Symbol	Value	Unit
Cavity length	l	1.0	mm
Stripe width	w	200	μm
Active layer thickness	h	0.2	μm
Linewidth enhancement factor	α	3.0	
Linear gain coefficient	a	1×10^{-20}	m^2
Confinement factor	Γ	0.3	
Effective refractive index	n_r	3.5	
Effective group index	n_g	4.0	
Reference wavelength	λ_r	810	nm
Reference carrier density	N_0	1×10^{24}	m^{-3}
Internal loss	α_i	30	cm^{-1}
Carrier lifetime	τ_R	5	ns
Current decay distance	d	10	μm
Left output power reflectivity	r_1^2	0.35	
Right output power reflectivity	r_2^2	0.35	

In this chapter we use the parameter values of Table 3.1. They effectively resemble those of [30][31] where a AlGaAs laser was investigated using BPM. We regard a stripe width of $w = 2x_0 = 200\,\mu$m. We keep this width throughout the thesis. In the calculations presented in this chapter, the output facets will be considered cleaved. As we are not regarding a specific device we have calculatet neither the effective index nor the confinement factor but use the

values in the table. In actual high power devices most often the output facet is antireflection coated while the other facet is high-reflection coated. In this way practically all power is emitted through one of the mirrors only. Moreover, the intensity inside the cavity is reduced leading to less lateral filamentation and to a higher catastrophic power level [63]. For external cavity schemes, an antireflection-coating implies a higher level of feedback from the external reflector to the chip. This has been shown to improve the obtained spatial coherence considerably. The angular dependence of reflectivity of a coated facet is enhanced as compared with a cleaved facet. This could be implemented in a laser model, and is perhaps an overlooked issue in the (modern) literature on modeling of high-power lasers.

The justification of including only one longitudinal mode is based on arguments and measurements found in the literature, e.g. [1]. Spectrally resolved near-fields show that the respective near-fields for individual longitudinal modes appear similar. Similarly, the authors of [64] measured spectrally resolved near-field intensity distributions of a freely running 100 micron wide BA laser. It can be seen that the individual longitudinal modes contain similar lateral properties. That is to say that the read out from the grating spectrometer which is a function of lateral position and wavelength is similar for each longitudinal mode. It may hence be assumed that one can regard one longitudinal mode independently of the others. For a BA laser that lack uniformity in the laser material, the assumption of similar lateral field distributions for each longitudinal may become dubious [65].

3.4 Calculated stationary solutions

We find a systematic structure in the tuning curves, i.e. calculated solutions in the current-frequency plane, and in the stationary solutions they represent. The systematic structure enables us to categorize different types of stationary solutions. Figure 3.2 presents calculated tuning curves in the $(J/J_0, \hat{f})$-plane where $\hat{f} = (\omega_s - \omega_r)/(2\pi)$ is the relative frequency.

We categorize different types of field distributions $E_s(x)$ corresponding to different branches of the curves in Figure 3.2. The figure contains curves for 3 different types of modes. In addition to the 3 categories of modes in Figure 3.2, more exist as we shall see below. First, however, we regard the three categories of Figure 3.2 named type I (m^I), type II (m^{II}), and type III (m^{II}). m is an integer denoting the mode number. Our investigation

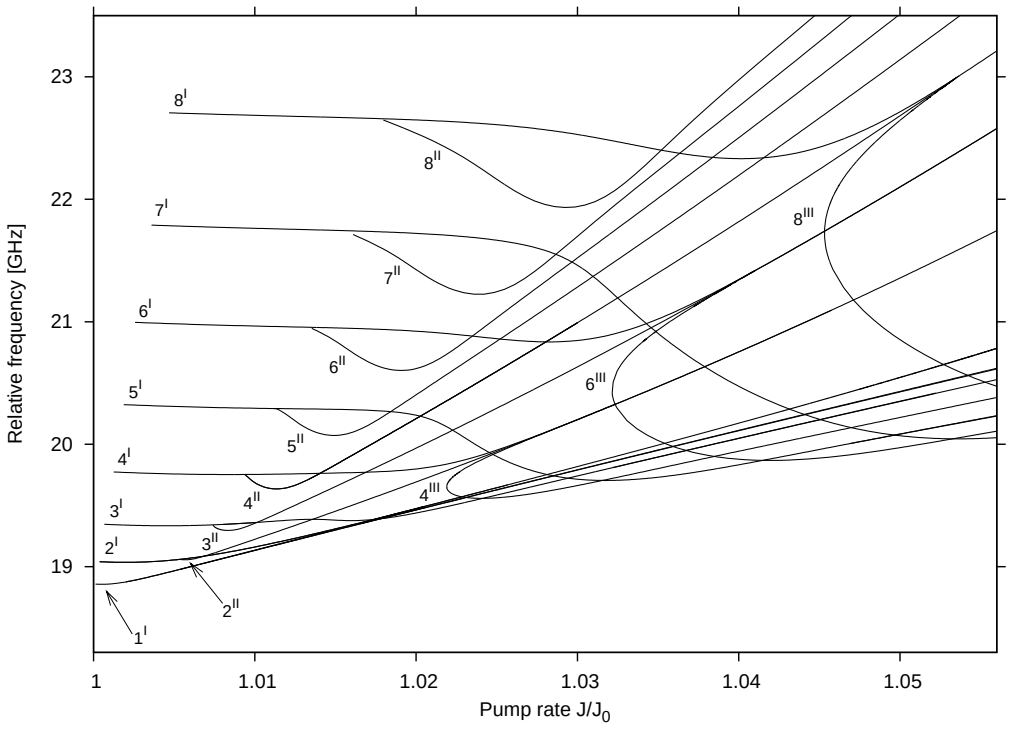

Figure 3.2: Tuning curves of modes-types m^I, m^{II}, and m^{III} for $m = 1$ to $m = 8$. Notice that the threshold pump rate of m^I increases with m and that m^{II} and m^{III} emerge at increasingly high pump rate for increasing m.

focuses on rather modest pump rates. The reason for this is two-fold: Firstly, stability-analyses in the following chapter reveal instabilities at low currents. Secondly, we find a structure in the modes that roughly speaking tells that what happens for a low-order mode also happens for a higher-order mode but at a higher current.

For all types of modes the integer m denotes the number of peaks in its near-field.

Type I modes

The first category of modes was also found in [1] albeit with different parameter values. Type I modes are modes of definite parity. These modes are labeled m^I where m is an odd integer for symmetric modes and m is an even integer for antisymmetric modes. In Figure 3.2 these modes are seen to have

increasing threshold currents for increasing m caused by an increased absorption in the unpumped layers as we shall review in Chapter 6. The lateral outward flow of energy increases with increasing m causing larger losses at threshold for higher order modes. At their respective thresholds m^I are linear gain guided modes. When the pump rate is increased their field distributions become perturbed due to the nonlinearity of the material and change shape, i.e. they do not merely increase in amplitude with an unchanged shape. In Figure 3.3 one can see near-fields for 6^I at 4 different pump rates.

When following the almost horizontal parts of the m^I-tuning curves from threshold and upwards in current, new branches emerge on the lower sides, e.g. at $J = 1.018J_0$ for $m = 8$. These branches are tuning curves of the second kind of modes and will be described in the subsequent subsection. One characteristic feature of the type I modes is a dip in the middle of the near-field which becomes deeper as the current is increased modestly above threshold. An example of this behavior can be seen in Figure 3.3 (a) and (b). This is studied in more detail in Chapter 6.

Further, the symmetric and antisymmetric modes differ in the sense that the symmetric modes (odd m) become increasingly compressed around $x = 0$, whereas the intensity distribution of the antisymmetric modes (even m) becomes increasingly localized near the edges of the metal contact, i.e. near $x = \pm x_0$ as the current is increased. Thus the intensity divides itself in two when the pump rate becomes considerable for a given mode m^I for even m. Near-fields of 6^I (antisymmetric) in Figure 3.3 and 5^I (symmetric) in Figure 3.4 for increasing pump rates show the general behavior of the 2 different parities for $m > 1$.

The far-fields of 6^I in Fig. 3.5 are representive of antisymmetric modes. Just above threshold (a), the far-field is nicely twin-lobed but as the current is increased, nonlinear perturbations deteriorate the twin-lobes by adding more and more structure around the lobes.

The change in far-field for the symmetric modes with increasing current is partly different from the antisymmetric modes. For example, the far-fields of mode 5^I shown in Fig. 3.6 reveal that just above threshold (a) and slightly higher above (b) the twin-lobe structure and the slighty perturbed twin-lobe structure, respectively, are similar to the antisymmetric modes. However, when increasing the current sufficiently the far-field becomes single-lobed as seen in (d). The single lobe is, however, perturbed by side lobes

It is sometimes said that BA lasers have twin-lobed far-fields. This is true

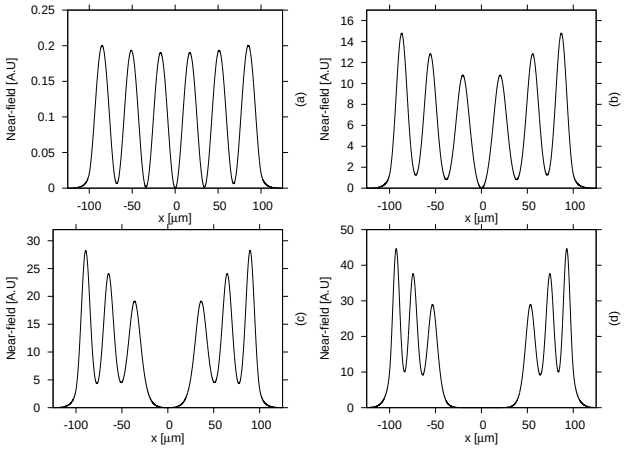

Figure 3.3: Near-field of mode 6^I at different pump rates. (a) Just above threshold $J = 1.0029J_0$; (b) Slightly higher pump rate $J = 1.023J_0$. Note the increased dip around $x = 0$; (c) $J = 1.040J_0$; (d) $J = 1.0675J_0$. For higher currents the intensity becomes more localized near $x = \pm x_0$.

for gain guided modes at threshold. However, when the current is increased this assumption breaks down since the modes become highly nonlinear. Thus even if one could make the laser operate in a single lateral mode of type I the spatial coherence would be poor even for rather low currents. In Chapter 4 we shall se that for $m \geq 3$ all m^I become unstable immediately above threshold or one can say that they are born unstable. Thus if a far-field is measured with a a twin-lobed structure it is most likely a result of the laser being in a time-dependent state over which a detector has averaged in time. Typically, at least for wide BA lasers with $w \geq 100\,\mu$m, the time-averaged far-field is a blurred shape and not a clear twin-lobe like in Figure 3.5 (a) or 3.6 (a).

Type II modes (asymmetric)

The physical system under investigation is symmetric around $x = 0$. Yet we find that stationary solutions without definite parity (asymmetric field distributions) exist due to the nonlinearity in the field equation and possibly also due to the boundary conditions. One type of asymmetric modes is presented in this subsection. This second kind of stationary solutions is denoted m^{II}. At the branch point where they are born in Figure 3.2, e.g.

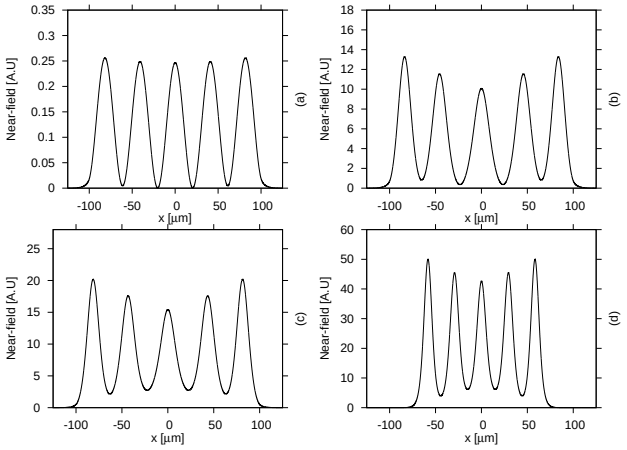

Figure 3.4: Near-field of mode 5^I at different pump rates. (a) Just above threshold $J = 1.0022J_0$; (b) Slightly higher pump rate $J = 1.0199J_0$ Note the increased dip around $x = 0$; (c) $J = 1.0274J_0$; (d) $J = 1.0665J_0$. For the higher currents the intensity becomes compressed around $x = 0$.

$J = 1.018J_0$ for $m = 8$, they have field distributions identical to the respective definite-parity solutions m^I, but for increasing currents they become increasingly compressed on either side of $x = 0$. There are two $\hat{f}$-degenerate solutions for a point on the type II tuning curves: a left one and a right one. It can be seen that the tuning curve of mode m^{II} eventually merges with that of mode $(2m)^I$ when increasing the current. For example 4^{II} merges with 8^I at $J \simeq 1.054J_0$, (a third branch is seen to branch out from this point also as explained in the next subsection). At the point where the m^{II}-mode merges with the $(2m)^I$-mode, the intensity distribution of the m^{II}-mode is localized on the left (right) side of the middle, i.e. on either $-x_0 < x < 0$ or $0 < x < x_0$. At this point in the $(J/J_0, \widehat{f})$-plane the near-fields of the two degenerate m^{II}-modes added together spatially overlap the near-field of $(2m)^I$.

The evolution of a type II mode from its birth to higher currents is illustrated in Figures 3.7, 3.8, and 3.9. The near-field of mode 4^{II} in Figure 3.7 starts out identical to that of 4^I around $J = 1.0093J_0$. When increasing the current, i.e. running along the tuning curve for 4^{II} in Figure 3.2, the near-field initially begins to tilt to either side (remember that asymmetric solutions are doubly degenerate) as seen in 3.7. As the current is increased further the field becomes more and more localized on either side of $x = 0$.

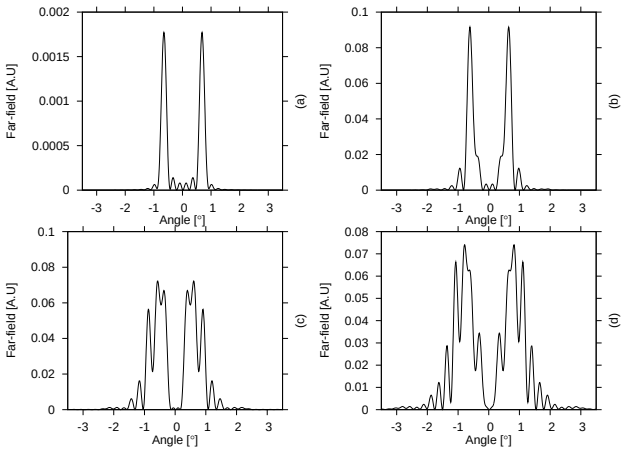

Figure 3.5: Far-fields of mode 6^I at the same pump rates as in Fig. 3.3. As the pump rates is increased, the twin-lobes become increasingly perturbed.

At the highest current represented in Figure 3.7, the near-field has left either side empty. For this current ($J = 1.054J_0$) the tuning curve of 4^{II} merges with the tuning curve of 8^I. For even higher currents 4^{II} becomes more localized near $x = \pm x_0$. The far-field over the same current range as in Figure 3.7 is presented in Figures 3.8 and 3.9 where it can be seen how the initially symmetric twin-lobed far-field becomes increasingly asymmetric and single lobed. Note that the tilt in the far-field is opposite the one in the near-field. I.e. the angle of the dominant single-lobe in the far-field has the opposite sign of the overall slope of the near-field.

That asymmetric solutions of the field equation exist is not obvious, since the physical system is symmetric around $x = 0$. The fact that they emerge from the branch of a m^I-mode is due to saddle-node bifurcations as it will become clearer in Chapter 4. Perhaps m^{II}-modes may be relevant in understanding the way AEC lasers with their spatial filtering can operate because of the single-lobed far-fields of m^{II}. However, also m^{II} will in Chapter 4 be found unstable in such a way that they have to operate in a time-dependent state. Note that 1^{II} *does* exist but its tuning curve is not visible in Figure 3.2 as it lies very close to the surrounding curves.

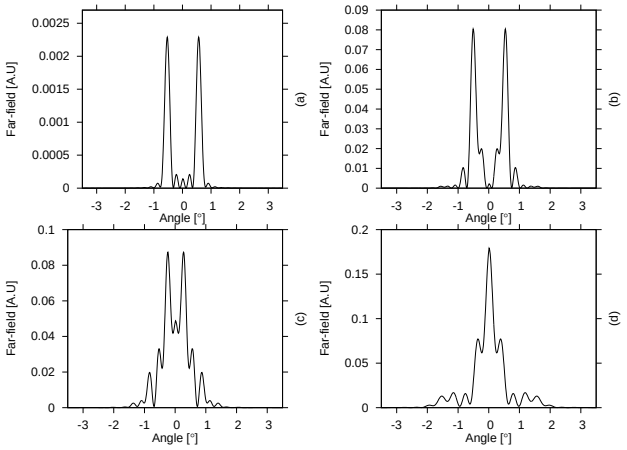

Figure 3.6: Far-fields of mode 5^I at the same pump rates as in Fig. 3.4. As the pump rate is increased the twin-lobe change into a perturbed single-lobe field.

Type III modes (asymmetric)

In addition to modes of type I and type II, Figure 3.2 contains tuning curves labeled m^{III}. These solutions also correspond to asymmetric field distributions. Type III curves for odd m are not visible in the figure as they lie very close to their type I "parents" from which they emerge. At the point where an m^{III}-mode branches out from the m^I-curve, the field distributions of m^I and m^{III} are identical. Similarly to the behavior of type II modes, the near-fields of m^{III} become more and more compressed towards either side of $x = 0$ as the pump rate is increased and they also have an $\hat{f}$-degenerate solution whose intensity distribution is the mirror image with respect to $x = 0$. Unlike m^{II} the near-fields of m^{III} do not tilt considerably as the current is increased. To our findings only one asymmetric mode emerges from 1^I, namely the mode we call 1^{II}. Thus, apparently no m^{III}-mode exists for $m = 1$.

In Figure 3.10 it is evident how the near-field of 5^{III}, representing odd m, is compressed towards either side of the pumped region when the current is augmented. The corresponding far-fields in Figure 3.11 are single-lobed and become asymmetric only to a very little degree and are thus odd-m-m^I-like.

The behavior of m^{III} for even m is slightly more complicated. The near-

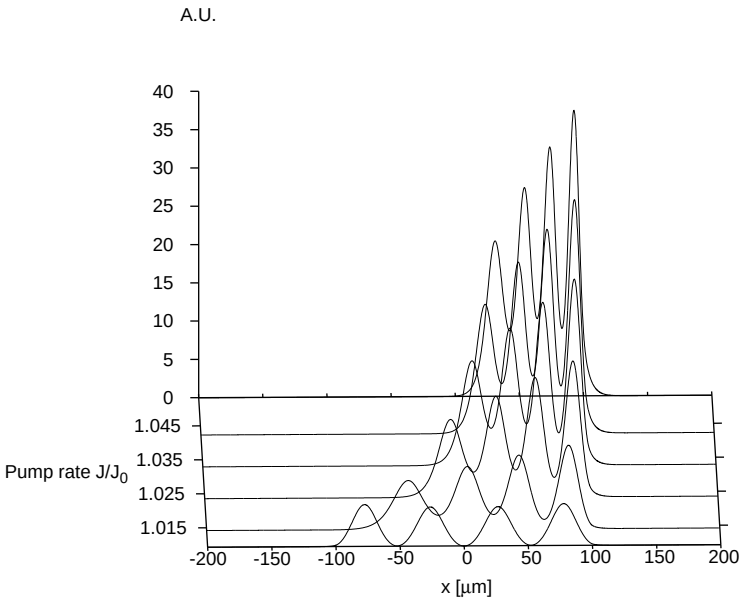

Figure 3.7: Mode 4^{II}: Near-field for pump rates $J = 1.0093J_0$ where the mode emerges through $J = 1.054J_0$ where the tuning curve of the mode merges with the one of 8^I.

and far-fields of 4^{III} are displayed in Figures 3.12 and 3.13. The fields for different currents represent running along the 4^{III}-tuning curve from the branch point on 4^I (a); on to a point where the tuning curve for 4^{III} bends (b); on to a point after the bend (c); and finishing at a point far after the bend (d). It can be seen that the near-field remains centered around $x = 0$ until finally sliding towards either side in (d). The far-field in Figure 3.13 turns single-lobed although the parent 4^I is never single-lobed in the far-field. Therefore, also m^{III} with m even seems odd-m-m^I-like.

When the pump rate becomes relatively high and the intensity distribution of m^{III} (for both even and odd m) is localized on either $-x_0 < x < 0$ or $0 < x < x_0$, its tuning curve merges with the tuning curve of yet another type of modes (labeled m^{IV}) that we have found to exist. This may be seen for 4^{III} in Figure 3.14, where tuning curves are shown.

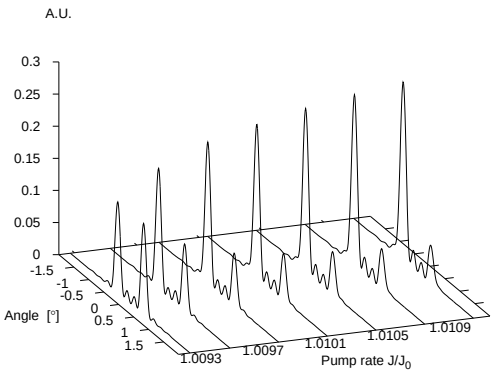

Figure 3.8: Mode 4^{II}: For pump rates $J = 1.0093J_0$ where the mode emerges through $J = 1.011J_0$. The far-field becomes increasingly single-lobed.

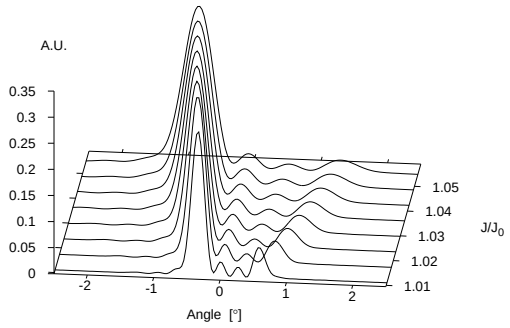

Figure 3.9: Mode 4^{II}: For pump rates $J = 1.011J_0$ through $J = 1.054J_0$ where the tuning curve of the mode merges with the one of 8^I. The dominant lobe moves outwards for increasing current.

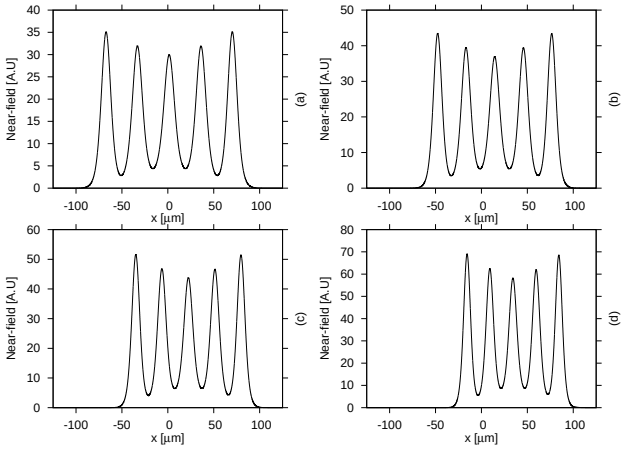

Figure 3.10: Mode 5^{III}: Near-fields. (a) $J = 1.0469J_0$ where mode emerges ; (b) $J = 1.0578J_0$; (c) $J = 1.0684J_0$; (d) $J = 1.0794J_0$. As the current is increased the near-field is compressed towards either edge of the pumped region.

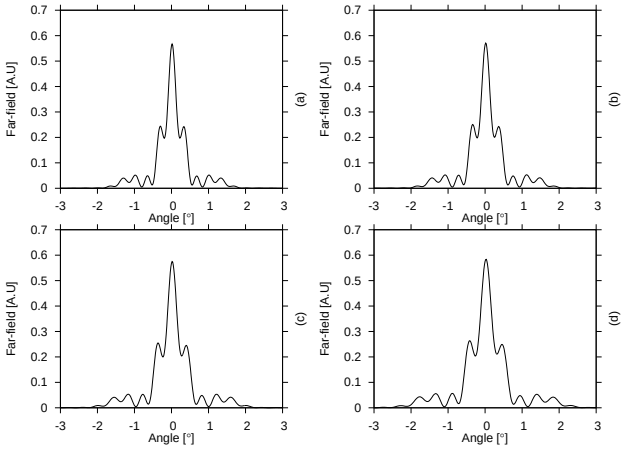

Figure 3.11: Mode 5^{III}: Far-fields. Same pump rates as in Figure 3.10. The far-field is centered at $\theta = 0$ and becomes increasingly perturbed with increasing pump rate. It is only slightly asymmetric even with a strongly asymmetric near-field.

Type IV modes (definite parity)

We move on to present yet another exotic category of modes that we have found to exist. So far we have seen one category of definite parity, namely

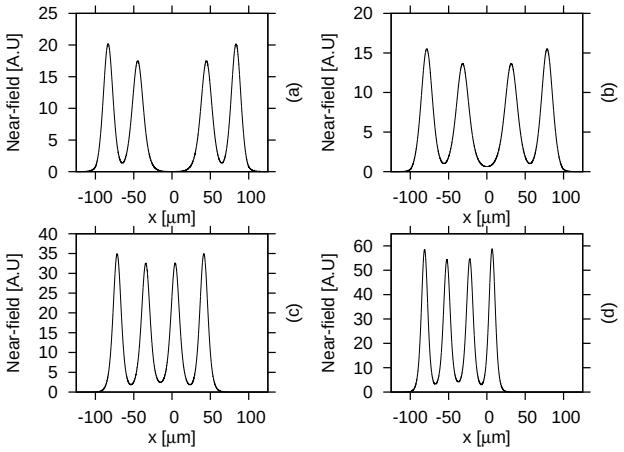

Figure 3.12: Mode 4^{III}: Near-fields.(a) $J = 1.029J_0$; (b) $J = 1.022J_0$; (c) $J = 1.048J_0$; (d) $J = 1.080J_0$. These four pump-rates correspond to following the tuning curve of 4^{III} from where it emerges on 4^{I} and around its bend.

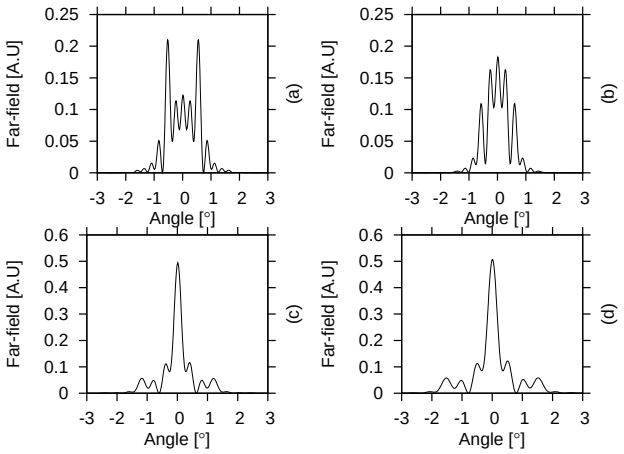

Figure 3.13: Mode 4^{III}: Far-fields. Same pump rates as in Figure 3.12. The far-field goes from being a perturbed twin-lobe to being a perturbed single-lobe. It is only slightly asymmetric even with a strongly asymmetric near-field.

type I. For current levels close to their thresholds they can be viewed as linear gain guided modes perturbed by nonlinear effects. We now come to a category of definite-parity modes which are solely nonlinear in the same way that the asymmetric modes m^{II} and m^{III} cannot exist without the

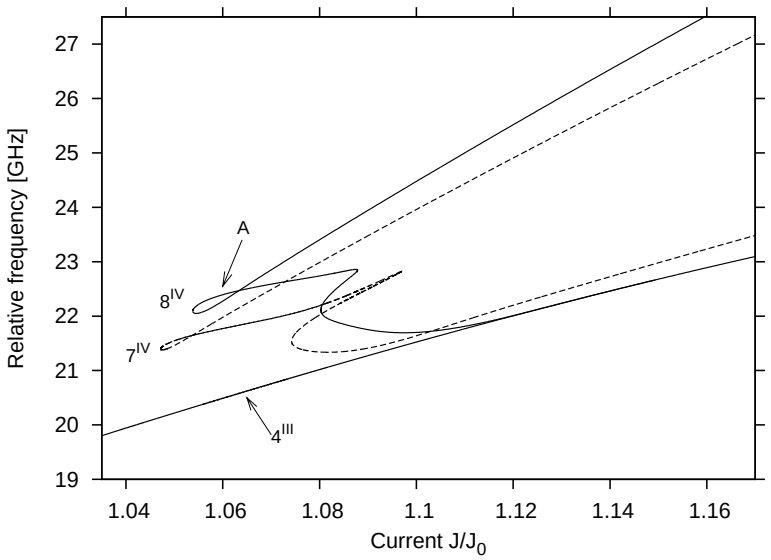

Figure 3.14: Tuning curves of modes 7^{IV}, 8^{IV}, and 4^{III}. It can seen how 4^{III} merges with 8^{IV}. The mark "A" corresponds to near- and far-field shown in Figure 3.15 (a) and (b).

nonlinearity of the gain material. The tuning curves in Fig. 3.14 each showing a loop and a cusp correspond to highly nonlinear finite-parity modes. We denote the modes corresponding to such tuning curves type IV. Examples for 7^{IV} and 8^{IV} are seen in the figure. Again, the tuning curve for 4^{III} is also seen merging with 8^{IV}. When running along the tuning curves of m^{IV} the field distributions change considerably in character. On the upper parts of these curves (the high-frequency part) the near-field is a self-focusing solution which is increasingly localized around $x = 0$ with increasing pump rate. Near- and far-field of 8^{IV} near $(J/J_0 = 1.06, \hat{f} = 22.3$ GHz) (marked "A") can be viewed in (a) and (b) of Figure 3.15. This is an example of a field distribution of the high-frequency part. It is rather remarkable that one can find self-focusing solutions in a system where the near-fields of the "conventional" modes (type I) have slowly varying dips around $x = 0$. So called spatial solitons have been observed in BA optical amplifiers [66]. The spatial solitons were traveling waves with self-focusing field distribution formed inside the BA amplifier. Possibly the self-focusing solutions, that we have found, are related to these experimentally observed solitons.

On the low frequency part of the tuning curve of 8^{IV} the field distributions

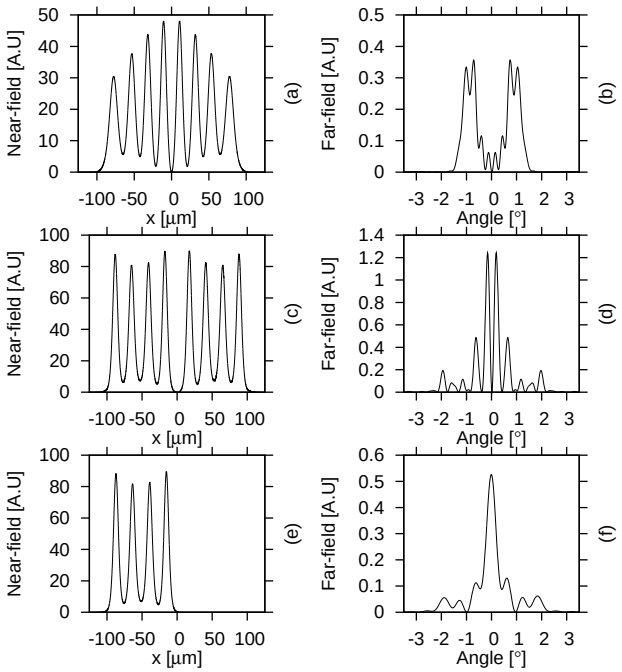

Figure 3.15: Near- and far fields corresponding to points on tuning curves in Figure 3.14. (a) and (b) are near- and far-field corresponding to the mark "A" on tuning curve 8^{IV}. (c) and (d) are near- and far-field of 8^{IV} corresponding to the point where 4^{III} merges with 8^{IV}. (d) and (e) are near- and far-field of 4^{III} at the same point.

are of a different character. In Figure 3.14 it is seen how 4^{III} merges with 8^{IV} around $J = 1.12J_0$. Figure 3.15 shows field distributions for 8^{IV} ((c) and (d)) and 4^{III} ((e) and (f)) at their merging point . At the point where m^{III} and $(2m)^{IV}$ merge, the near-field of either m^{III} (there are two of them) makes up half the near-field of $(2m)^{IV}$, whereas the far-fields are completely different. To our findings, the lowest order m^{IV}-mode is 3^{IV}.

The systematic structure of the BA-laser modes

As can be clearly seen from Figure 3.2, the lateral modes in a BA laser have an underlying systematic structure. Type I modes are the basic stationary states of BA lasers since they are linear gain guided modes at their respective thresholds. The remaining types of modes can exist only due to the nonlinearity of the gain material. The mode with the lowest threshold current is 1^I. Mode 1^{II} branches out from 1^I and merges with 2^I. Mode 2^{II} bifurcates from 2^I and merges with 4^I. In addition mode 2^{III} branches out from 2^I at a higher current than 2^{II}. Mode 2^{III} also merges with a mode at a higher current, namely mode 4^{IV}. Hence modes m^{II} emerge from m^I and eventually merge with $(2m)^I$. Also, modes m^{III} emerge from m^I and merge with modes $(2m)^{IV}$. The exception is that "1^{III}" does not exist.

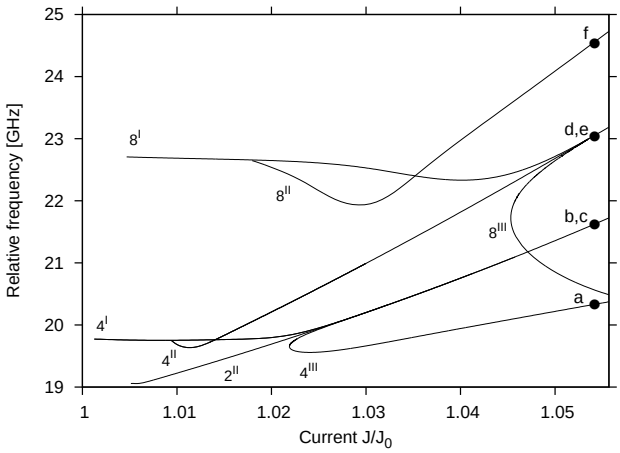

Figure 3.16: Exert of 3.2 summarizing part of the systematic structure of the BA-modes. Modes 2^{II}, 4^I, 4^{II}, 4^{III}, 8^I, 8^{II}, and 8^{III} are shown. The bullets correspond to near-fields in Figure 3.17 and far-fields in Figure 3.18.

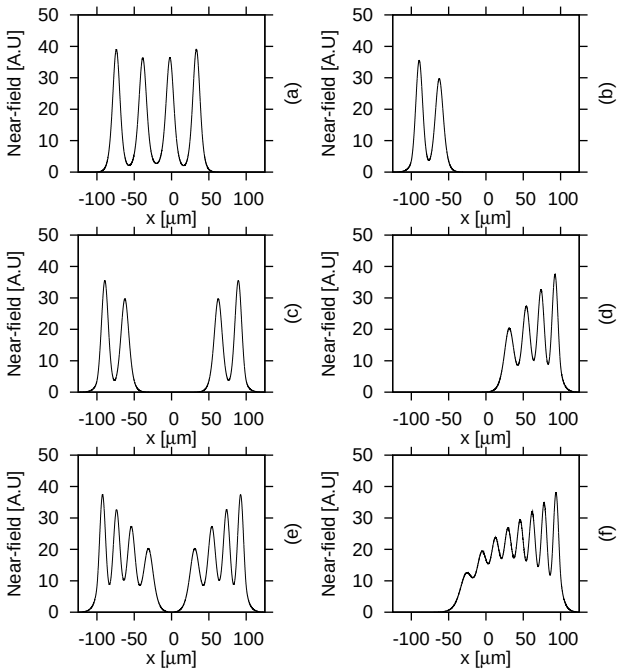

Figure 3.17: Near-fields corresponding to bullets in Figure 3.16. (a) 4^{II}; (b) 2^{II}; (c) 4^{I}; (d) 4^{II}; (e) 8^{I}; (f) 8^{II}.

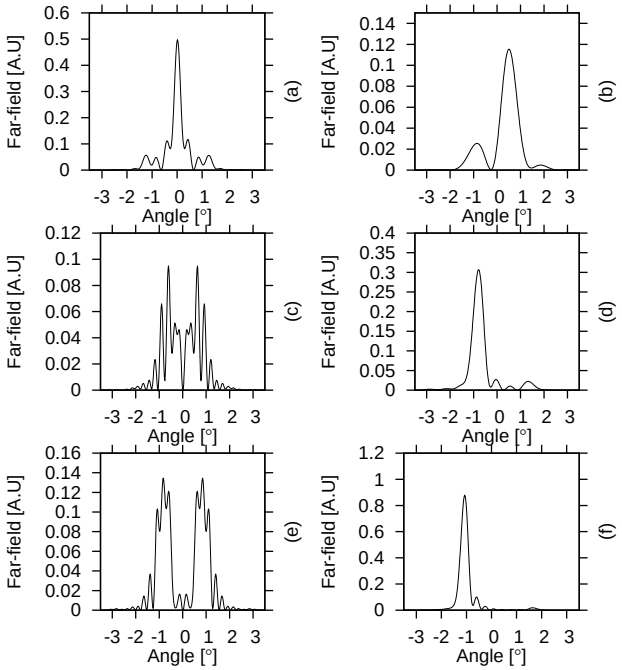

Figure 3.18: Far-fields corresponding to bullets in Figure 3.16. (a) 4^{II}; (b) 2^{II}; (c) 4^{I}; (d) 4^{II}; (e) 8^{I}; (f) 8^{II}.

An exert of the structure with only tuning curves for 2^{II}, 4^{I}, 4^{II}, 4^{III}, 8^{I}, 8^{II}, and 8^{III} is displayed in Figure 3.16. The points labeled (a)-(f) are different examples of the just mentioned six modes at $J = 1.054J_0$ (the current at which 4^{II} and 8^{I} merge). The corresponding near-fields are found in Figure 3.17 and the far-fields in Figure 3.18. In these two figures (a) is 4^{III} with a near-field that is asymmetric but almost untilted. Note that its far-field is single-lobed and centered around an angle of 0 degrees. (b) and (c) are 2^{II} and 4^{I} at a higher current than where 2^{II} merges with 4^{I}. The near-field of 2^{II} is localized near $-x_0$ or x_0 and is seen to constitute "half the near-field" of 4^{I}. Similarly, (d) and (e) are 4^{II} and 8^{I} at their merging point. (f) is 8^{II}.
A close-up of 2^{III} branching out from 2^{I} is displayed in Figure 3.19. Also here 1^{II} merges with 2^{I}. This figure is then a close-up of Figure 3.2.

The remarkable systematics of the mode structure that we have found is different from the mode structure of a DFB laser where symmetry-breaking field solutions also exist. A multitude of solutions can indeed be found in the case of a semiconductor DFB laser [67]. We believe that the structure applies to all mode orders m as we checked for higher for orders, e.g. $m = 15$. Asymmetric modes may also be found in stripe geometry lasers [68].

Additional types of modes

In addition to the different modes mentioned so far, we have found two further types of modes. They are asymmetric modes likely to bifurcate from m^{IV}. We leave them to future work.

Light-current characteristics

The light current characteristics corresponding to the tuning curves in 3.2 are displayed in Figure 3.20. Thus, displayed are light-current characteristics for m^{I}, m^{II}, and m^{III} for m equal to 1 through 8. The total output power is given as (see Eq. (A.11))

$$P_{out} = 2\epsilon_0 n_r c \alpha_m l K \int_{-\infty}^{\infty} |E_s(x)|^2 dx. \tag{3.63}$$

As an example, modes 6^{I}, 6^{II}, and 6^{III} are shown separately in Figure 3.21. As expected the branch points are located at the same pump rates as for corresponding tuning curves.

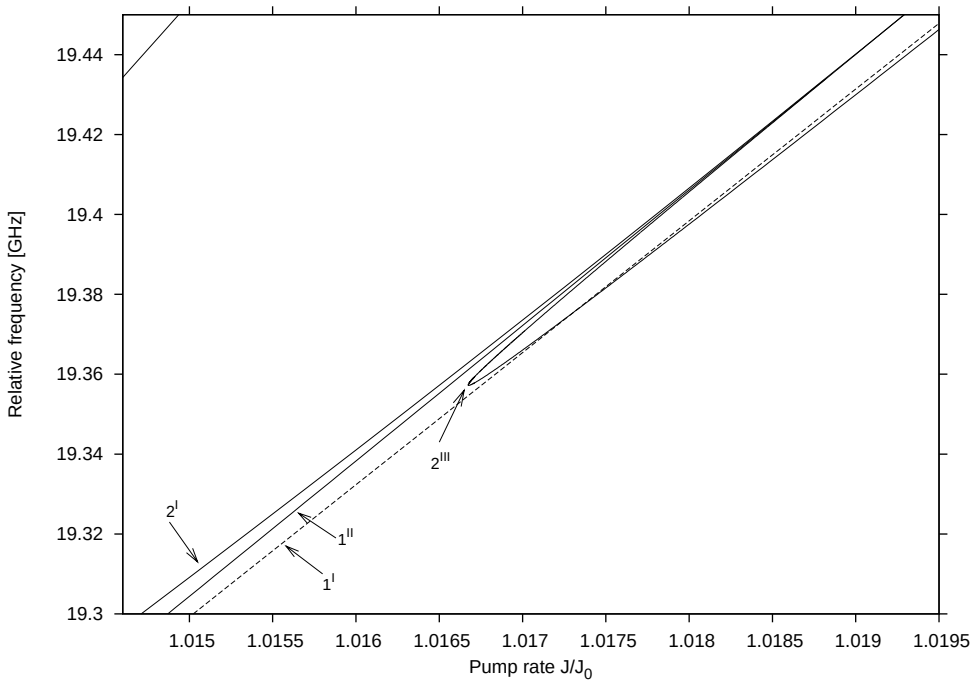

Figure 3.19: Tuning curve: Close-up of Figure 3.2. Mode 2^{III} branches out from 2^I and 1^{II} merges with 2^I.

3.5 Summary

In this chapter we have studied the lateral mode structure of a BA laser. The stationary solutions were found using a mean field approximation, which lead to equations in 1 spatial dimension. The simple lateral geometry of a gain guided laser proved to contain a rich and systematic structure of modes and not only "standard" gain guided modes that we have labeled type I modes (they in themselves show interesting properties). We introduced 3 other categories of modes, and all four types of modes were seen to be interrelated in spatial shape and through the structure of their tuning curves. Of particular interest were the asymmetric type II modes as their far-fields resemble the single-lobed far-field of the AEC laser presented in Chapter 2. In the following chapter we will test the stability of type I and type II.

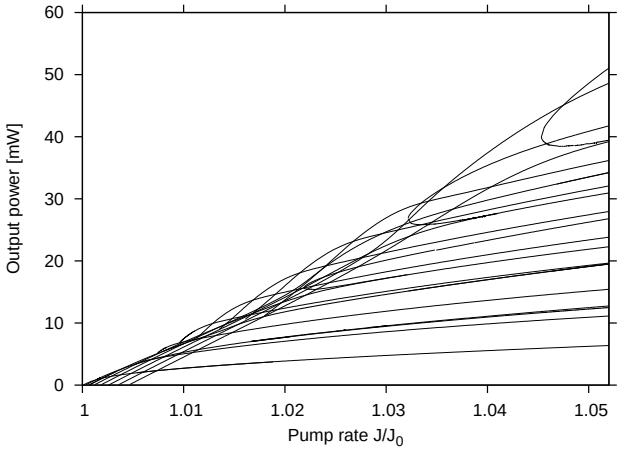

Figure 3.20: Light-current characteristics of modes m^I, m^{II}, and m^{III} for m going from 1 to 8. That is, P_{out} as a function of J/J_0.

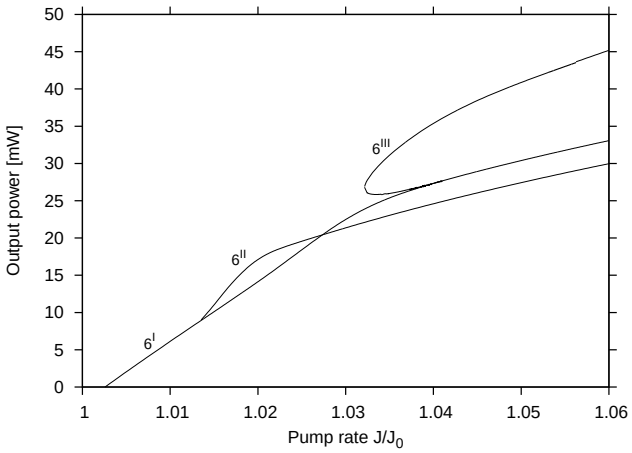

Figure 3.21: Light-current characteristics of modes 6^I, 6^{II}, and 6^{III}.

Chapter 4

Small-signal analysis using Green's functions: Stability properties and responses

In the Chapter 3 we found stationary solutions using the nonlinear field equation (3.49). In this chapter we shall study the small-signal properties of some of them, namely type I and type II. First and foremost we want to perform a stability analysis. Lasers are nonlinear systems whose stationary solutions in a small-signal analysis can be classified as stable or unstable. In semiconductor-laser theory it can sometimes be said that the stationary solution having the lowest threshold gain of all modes is the dominant mode as the gain clamps at threshold. BA lasers are known to become pulsating at very low continuous pump currents, showing multi-mode or even what is likely to be chaotic behavior and the gain of a given mode does not clamp at threshold due to spatial hole burning. Thus, there is no indication that such an assumption is generally valid for a BA laser.

In a small signal analysis, one may talk about two different kinds of stability, namely local stability and global stability [67]. A locally stable mode is stable with respect to small-signal fluctuations. Fluctuations present in the physical system will make a locally unstable mode go to a different stationary solution or a time-dependent state. A local instability is also called an instability of the saddle-point type. If a mode is locally stable it is not necessarily globally stable. Other than the saddle-point-type instability, a mode may suffer from a self-pulsating instability, which must also be tested for before a mode can be called globally stable. Specifically, if the system

determinant $D(s)$ has two zeroes lying symmetrically around the real s-axis in the right half s-plane, then the system is in a time-dependent state. This is an instability of the Hopf-type. Here $s = j\Omega$, where Ω is the baseband frequency. Instabilities of the saddle-point type, on the other hand, are associated with a zero of $D(s)$ lying on the real s-axis in the right half s-plane. A saddle-point instability may be associated with a saddle-point bifurcation where a zero of $D(s)$ moves along the real s-axis from the left half s-plane into the right. Similarly an instability of the Hopf-type may appear in conjunction with a Hopf-bifurcation where the two complex conjugate zeroes of $D(s)$ move from the left to the right half plane, e.g. when the pump current of the laser is increased. The reason why we distinguish between, say, a pulsating instability of the Hopf-type and an actual Hopf bifurcation is that, as it shall become clear in this chapter, stationary solutions may be "born" unstable, such that an actual bifurcation cannot be detected; only the instability of a mode is detectable in this case.

Laser models, where the photon and carrier density are effectively treated without spatial dependence, usually yield an algebraic expression for the system determinant, whose zeroes in the complex frequency-plane are found by graphical or iterative methods. The stationary solutions found in the previous chapter have a spatial dependence in the lateral direction. To carry out a stability analysis on these modes, we employ a Green's function method [69]. The method in its original form was derived for DFB lasers. For lateral gain guided modes, new small-signal equations must be derived. For saddle-point bifurcations we have, thanks to the work presented in the previous chapter, the great advantage of knowing where new branches emerge on tuning curves. When the small-signal analysis "predicts" a saddle-point bifurcation, perturbation theory tells us that one or more new branches of solutions will appear in a bifurcation diagram. We will be able to test the results of the stability analysis by looking for one or more emerging branches on the regarded tuning curve. When discussing bifurcations, intrinsicly one must define one or more bifurcation parameters. When varying the bifurcation parameter(s) a given stationary state, or rather the dependent variables associated with it, can be followed along curves in e.g. the $(J/J_0, \hat{f})$-plane, where J/J_0 is the bifurcation parameter. In fact the pump rate will be the only bifurcation parameter considered in the present thesis.

4.1 Small signal analysis using the logarithmic field

We start out by linearizing our field equation and carrier equation. We have to perform the linearization of the two equations separately in order to introduce the spectral part of the carrier density properly. Our inhomogeneous field equation in the time domain reads

$$\left[\frac{\partial^2}{\partial x^2} + \kappa(x,t) - j\frac{2k_r}{v_g}\frac{\partial}{\partial t}\right] E = f(x,t). \tag{4.1}$$

Upon neglecting carrier diffusion the carrier distribution is given by

$$\frac{\partial N(x,t)}{\partial t} = \mathscr{J}(x,t) - \frac{N(x,t)}{\tau_R} - v_g g_m(x,t) S(x,t), \tag{4.2}$$

Finding the small-signal properties of various stationary solutions involves a linear expansion around a specific calculated mode. For convenience we first introduce the logarithmic field b:

$$b = \ln E. \tag{4.3}$$

It is noteworthy that $\mathrm{Re}(b) = ln|E|$ and $\mathrm{Im}(b) = \phi_E$, where ϕ_E is the phase of E. The first and second derivatives of the logarithmic field are then

$$\frac{d}{dx}b = \frac{1}{E}\frac{d}{dx}E \tag{4.4}$$

and

$$\frac{d^2}{dx^2}b = \frac{1}{E}\frac{d^2}{dx^2}E - \frac{1}{E^2}\left(\frac{d}{dx}E\right)^2 \tag{4.5}$$

or from (4.4)

$$\frac{d^2}{dx^2}b = \frac{1}{E}\frac{d^2}{dx^2}E - \left(\frac{d}{dx}b\right)^2. \tag{4.6}$$

Hence, from Eq. (4.1) the logarithmic wave equation is seen to be

$$\frac{d^2}{dx^2}b + \left(\frac{d}{dx}b\right)^2 + \kappa(x,t) - j\frac{2k_r}{v_g}\frac{\partial}{\partial t}b = \frac{f(x,t)}{E}. \tag{4.7}$$

Next, we linearize the obtained logarithmic wave equation. Taking the differential on both sides of Eq. (4.7) yields

$$\frac{d^2}{dx^2}\delta b + 2(\frac{d}{dx}b)(\frac{d}{dx}\delta b) + \delta\kappa - j\frac{2k_r}{v_g}\frac{\partial}{\partial t}\delta b = \frac{f(x,t)}{E_s(x)}. \tag{4.8}$$

Here $E_s(x)$ is a stationary solution. As κ is independent of $E_s(x)$, the differential $\delta\kappa$ is found to be

$$\delta\kappa(x,t) = 2k_r\frac{\partial k}{\partial N}\delta N(x,t). \tag{4.9}$$

The small-signal expansion of (4.2) is found to be

$$\frac{\partial}{\partial t}\delta N = \delta J - \frac{\delta N}{\tau_R} - av_gB\left[\delta N|E_s|^2 + (N_s - N_0)(E_s^*\delta E + E_s\delta E^*)\right]. \tag{4.10}$$

From Eq. (4.3) we get $\delta b = \delta E/E_s$ and thus $\delta E = \delta b E_s$ and $\delta E^* = \delta b^* E_s^*$. Substituting into Eq. (4.10) results in

$$\frac{\partial}{\partial t}\delta N = \delta J - \frac{\delta N}{\tau_R} - \frac{1}{P_{sat}\tau_R}\left[\delta N|E_s|^2 + 2(N_s - N_0)|E_s|^2\mathrm{Re}(\delta b)\right]. \tag{4.11}$$

Going to the baseband frequency domain implies taking the Fourier transform

$$s\widetilde{\delta N} = \widetilde{\delta J} - \frac{\widetilde{\delta N}}{\tau_R} - \frac{1}{P_{sat}\tau_R}\left[\widetilde{\delta N|E_s|^2} + 2(N_s - N_0)|E_s|^2\widetilde{\mathrm{Re}(\delta b)}\right], \tag{4.12}$$

since E_s is stationary in time. A tilde over a symbol denotes that it is a function in the baseband frequency Ω by $s = j\Omega$. Solving for $\widetilde{\delta N}$ gives

$$\widetilde{\delta N}(x,s) = \frac{\widetilde{\delta J}(x,s)\tau_R}{1 + s\tau_R + |E_s|^2/P_{sat}} - \frac{J_s(x)\tau_R - N_0}{1 + |E_s|^2/P_{sat}}\frac{|E_s|^2/P_{sat}}{1 + s\tau_R + |E_s|^2/P_{sat}}2\widetilde{\mathrm{Re}(\delta b)}. \tag{4.13}$$

We divide the logarithmic field into real and imaginary parts by introducing the vector

$$\boldsymbol{\psi} = \begin{pmatrix} \mathrm{Re}(\delta b) \\ \mathrm{Im}(\delta b) \end{pmatrix}, \tag{4.14}$$

implying Eq. (4.8) in a new form:

$$\frac{d^2}{dx^2}\boldsymbol{\psi} + \boldsymbol{M_1}\frac{d}{dx}\boldsymbol{\psi} + k_r\Gamma a\delta N\begin{pmatrix} -\alpha \\ 1 \end{pmatrix} + \boldsymbol{M}_\omega\frac{\partial}{\partial t}\boldsymbol{\psi} = \boldsymbol{f}, \tag{4.15}$$

where

$$\boldsymbol{M}_1 = 2 \begin{pmatrix} \mathrm{Re}(\frac{db}{dx}) & -\mathrm{Im}(\frac{db}{dx}) \\ \mathrm{Im}(\frac{db}{dx}) & \mathrm{Re}(\frac{db}{dx}) \end{pmatrix}, \tag{4.16}$$

$$\boldsymbol{M}_\omega = \frac{2k_r}{v_g} \begin{pmatrix} 0 & 1 \\ -1 & 0 \end{pmatrix}, \tag{4.17}$$

and the noise is gathered in the vector $\boldsymbol{f}$ defined as

$$\boldsymbol{f} = \frac{1}{E_s} \begin{pmatrix} \mathrm{Re}f \\ \mathrm{Im}f \end{pmatrix}. \tag{4.18}$$

The Fourier transform of Eq. (4.15) yields the frequency domain equation

$$\frac{d^2}{dx^2}\widetilde{\boldsymbol{\psi}} + \boldsymbol{M}_1 \frac{d}{dx}\widetilde{\boldsymbol{\psi}} + \boldsymbol{M}\widetilde{\boldsymbol{\psi}} = \widetilde{\boldsymbol{f}} + \widetilde{\boldsymbol{j}} \tag{4.19}$$

where the matrix $\boldsymbol{M}$ is the sum

$$\boldsymbol{M} = \widetilde{\boldsymbol{M}_0} + s\boldsymbol{M}_\omega. \tag{4.20}$$

$\widetilde{\boldsymbol{\psi}}$ is the Fourier transform of $\boldsymbol{\psi}$ and

$$\widetilde{\boldsymbol{M}_0} = 2k_r\Gamma a \frac{J_s(x)\tau_R - N_0}{1 + |E_s|^2/P_{sat}} \frac{|E_s|^2/P_{sat}}{1 + s\tau_R + |E_s|^2/P_{sat}} \begin{pmatrix} \alpha & 0 \\ -1 & 0 \end{pmatrix}. \tag{4.21}$$

The current modulation term is given as

$$\widetilde{\boldsymbol{j}} = k_r\Gamma a \frac{\widetilde{\delta J}(x,s)\tau_R}{1 + s\tau_R + |E_s|^2/P_{sat}} \begin{pmatrix} \alpha \\ -1 \end{pmatrix}. \tag{4.22}$$

Now, Eq. (4.19) is the small-signal equation for the field and carrier density, for which Eq. (4.13) has been utilized. Note that for $\mathrm{Im}(s) \neq 0$, $\widetilde{\boldsymbol{\psi}}$ is in general complex.

Eq. (4.19) may be solved using Green's functions [70]. For convenience and for historical reasons we utilize the Green's function of the adjoint of the differential operator of (4.19) instead. The operator

$$L = \frac{d^2}{dx^2} + \boldsymbol{M}_1 \frac{d}{dx} + \boldsymbol{M} \tag{4.23}$$

has the adjoint operator

$$L^\dagger = \frac{d^2}{dx^2} - \frac{d}{dx}\boldsymbol{M}_1^\dagger + \boldsymbol{M}^\dagger. \tag{4.24}$$

Assume that $\boldsymbol{\zeta}_i(x', x, s)$ is the Green's function for $L^\dagger$. Then

$$\frac{d^2}{dx'^2}\boldsymbol{\zeta}_i - \frac{d}{dx'}(\boldsymbol{M}_1^\dagger\boldsymbol{\zeta}_i) + \boldsymbol{M}^\dagger\boldsymbol{\zeta}_i = \hat{\boldsymbol{e}}_i\delta(x'-x) \tag{4.25}$$

for $i = 1, 2$ and

$$\hat{\boldsymbol{e}}_1 = \begin{pmatrix} 1 \\ 0 \end{pmatrix} \text{ and } \hat{\boldsymbol{e}}_2 = \begin{pmatrix} 0 \\ 1 \end{pmatrix}. \tag{4.26}$$

In the following we shall first derive an expression giving $\widetilde{\boldsymbol{\psi}}$ for a given driving term $\widetilde{\boldsymbol{f}} + \widetilde{\boldsymbol{j}}$. After deriving this general form of the response, we evaluate the Green's functions $\boldsymbol{\zeta}_i$.

Partial integration of $\boldsymbol{\zeta}_i^\dagger(x', x, s)L\boldsymbol{\psi}(s, x')$ gives

$$\begin{aligned}
&\int_{-A}^{A} \boldsymbol{\zeta}_i^\dagger(x', x, s)\left(\frac{d^2}{dx'^2} + \boldsymbol{M}_1\frac{d}{dx'} + \boldsymbol{M}\right)\boldsymbol{\psi}(x', s)dx' = \\
&\int_{-A}^{A}\left(\frac{d^2}{dx'^2}\boldsymbol{\zeta}_i^\dagger(x', s) - \frac{d}{dx'}\left(\boldsymbol{\zeta}_i^\dagger(x', x, s)\boldsymbol{M}_1\right) + \boldsymbol{\zeta}_i^\dagger(x', x, s)\boldsymbol{M}\right)\boldsymbol{\psi}(x', s)dx' + \\
&\left[\boldsymbol{\zeta}_i^\dagger(x', x, s)\frac{d}{dx'}\boldsymbol{\psi}(x', s)\right]_{-A}^{A} + \left[\boldsymbol{\zeta}_i^\dagger(x', x, s)\boldsymbol{M}_1\boldsymbol{\psi}(x', x, s)\right]_{-A}^{A} - \left[\frac{d}{dx'}\boldsymbol{\zeta}_i^\dagger(s, x', x)\boldsymbol{\psi}(x', s)\right]_{-A}^{A}.
\end{aligned} \tag{4.27}$$

Alternatively, by manipulating the parenthesis in the right hand side integrand taking adjoints of both the interior and exterior, (4.27) may be put

$$\begin{aligned}
&\int_{-A}^{A} \boldsymbol{\zeta}_i^\dagger(x', x, s)\left(\frac{d^2}{dx'^2} + \boldsymbol{M}_1\frac{d}{dx'} + \boldsymbol{M}\right)\boldsymbol{\psi}(x', s)dx' = \\
&\int_{-A}^{A}\left(\frac{d^2}{dx'^2}\boldsymbol{\zeta}_i(x', x, s) - \frac{d}{dx'}\left(\boldsymbol{M}_1^\dagger\boldsymbol{\zeta}_i(x', x, s)\right) + \boldsymbol{M}^\dagger\boldsymbol{\zeta}_i(x', x, s)\right)^\dagger\boldsymbol{\psi}(x', s)dx' + \\
&\left[\boldsymbol{\zeta}_i^\dagger(x', x, s)\frac{d}{dx'}\boldsymbol{\psi}(x', s)\right]_{-A}^{A} + \left[\boldsymbol{\zeta}_i^\dagger(x', x, s)\boldsymbol{M}_1\boldsymbol{\psi}(s, x')\right]_{-A}^{A} - \left[\frac{d}{dx'}\boldsymbol{\zeta}_i^\dagger(x', x, s)\boldsymbol{\psi}(x', s)\right]_{-A}^{A}.
\end{aligned} \tag{4.28}$$

We demand that $\boldsymbol{\zeta}_i$ fulfill the boundary conditions

$$\frac{d}{dx'}\boldsymbol{\zeta}_i(x', x, s) = \boldsymbol{M}_1^\dagger(x', s)\boldsymbol{\zeta}_i(x', x, s) \tag{4.29}$$

at $x' = \pm A$. In addition, it is presumed that the term $d\boldsymbol{\psi}/dx$ is negligible at $x' = \pm A$ (see Appendix B). Then by inserting (4.19) and (4.25) in Eq. (4.28) we obtain

$$\int_{-A}^{A} \boldsymbol{\zeta}_i^\dagger(x', x, s)\widetilde{\boldsymbol{F}}dx' = \int_{-A}^{A} \delta(x' - x)\boldsymbol{e}_i^T\widetilde{\boldsymbol{\psi}}(x', s)dx' \tag{4.30}$$

which leads to the general expression for the response

$$(\widetilde{\boldsymbol{\psi}}(x, s))_i = \int_{-A}^{A} \boldsymbol{\zeta}_i^\dagger(x', x, s)(\widetilde{\boldsymbol{f}}(x', s) + \widetilde{\boldsymbol{j}}(x', s))dx'. \tag{4.31}$$

With Eq. (4.31) we have obtained the response for the noise $\widetilde{\boldsymbol{f}}(x, s)$ and a linear change of the pumping $\widetilde{\delta J}(x, s)$. In other words the expression can be used to calculate noise spectra and modulation responses. The notation "$(\widetilde{\boldsymbol{\psi}})_i$" means the ith component of the vector $\widetilde{\boldsymbol{\psi}}$.

The solution $\boldsymbol{\zeta}_i$ of Eq. (4.25) can be found by solving the homogeneous equation on each of the two intervals $-A < x' < x$ and $x < x' < A$. By integrating both sides of (4.25) on a small interval around x, the boundary condition

$$\left[\frac{d}{dx'}\boldsymbol{\zeta}_i(x', x, s) - \boldsymbol{M}_1^\dagger(x', s)\boldsymbol{\zeta}_i(x', x, s)\right]_{x'=x-}^{x'=x+} = \hat{\boldsymbol{e}}_i, \qquad i = 1, 2 \tag{4.32}$$

is obtained. We have used that $\boldsymbol{M}^\dagger\boldsymbol{\zeta}_i$ in (4.25) is continuous and made the interval of integration arbitrarily small so that the integral over this term vanishes.

Inspired by the DFB-laser case in [69], we evaluate the Green's function near the left boundary. Thus, we find the solution for $x = -A + \epsilon$, where ϵ is an arbitrarily small distance. For simplicity we shall define $\boldsymbol{\zeta}_i(x, s) = \boldsymbol{\zeta}_i(x, -A+, s)$ for $x > -A$, and denote $\boldsymbol{\zeta}_i(-A, s)$ the limit of $\boldsymbol{\zeta}_i(x, s)$ for $x \to -A+$. Solving Eq. (4.25) with the conditions (4.29) for $\boldsymbol{\zeta}_i(-A, s)$ then corresponds to solving the homogeneous equation

$$\frac{d^2}{dx^2}\boldsymbol{\zeta}_i - \frac{d}{dx}(\boldsymbol{M}_1^\dagger\boldsymbol{\zeta}_i) + \boldsymbol{M}^\dagger\boldsymbol{\zeta}_i = 0 \tag{4.33}$$

with the boundary conditions

$$\frac{d}{dx}\boldsymbol{\zeta}_i - \boldsymbol{M}_1^\dagger \boldsymbol{\zeta}_i = \hat{\boldsymbol{e}}_i \tag{4.34}$$

for $x = -A$ and

$$\frac{d}{dx}\boldsymbol{\zeta}_i - \boldsymbol{M}_1^\dagger \boldsymbol{\zeta}_i = 0 \tag{4.35}$$

for $x = A$.

Having formulated the homogeneous differential equation (4.33) with boundary conditions (4.34) and (4.35) we set out to find relations for $\boldsymbol{\zeta}_i$. Upon introducing the 4-dimensional vector

$$\boldsymbol{u}_i = \begin{pmatrix} \frac{d}{dx}\boldsymbol{\zeta}_i - \boldsymbol{M}_1^\dagger \boldsymbol{\zeta}_i \\ \boldsymbol{\zeta}_i \end{pmatrix} \equiv \begin{pmatrix} \boldsymbol{v}_i \\ \boldsymbol{\zeta}_i \end{pmatrix} \tag{4.36}$$

and the 4×4 matrix

$$\boldsymbol{M}_u = \left(\begin{array}{c|c} \boldsymbol{0} & -\boldsymbol{M}^\dagger \\ \hline \boldsymbol{I} & \boldsymbol{M}_1^\dagger \end{array} \right), \tag{4.37}$$

the homogeneous equation (4.33) may be put in the form

$$\frac{d}{dx}\boldsymbol{u}_i = \boldsymbol{M}_u \boldsymbol{u}_i. \tag{4.38}$$

In Eq. (4.37) the entity $\boldsymbol{0}$ is the 2×2 null matrix and $\boldsymbol{I}$ is the 2×2 identity matrix. We may also split Eq. (4.38) into the two equations

$$\frac{d}{dx}\boldsymbol{v}_i = -\boldsymbol{M}^\dagger \boldsymbol{\zeta}_i \tag{4.39}$$

and

$$\frac{d}{dx}\boldsymbol{\zeta}_i = \boldsymbol{M}_1^\dagger \boldsymbol{\zeta}_i + \boldsymbol{v}_i. \tag{4.40}$$

With the intention to solve Eq. (4.38) for $\boldsymbol{u}_i$ we form the linear combination

$$\boldsymbol{u}_i = \sum_{j=1}^{4} a_{ij} \boldsymbol{y}_j. \tag{4.41}$$

One may also write (4.41) in matrix form

$$\boldsymbol{u}_i(x, s) = \boldsymbol{Y}(x, s) \boldsymbol{a}_i(s), \tag{4.42}$$

where $\boldsymbol{Y}$ is the matrix

$$\boldsymbol{Y} = \{\boldsymbol{y}_1, \boldsymbol{y}_2, \boldsymbol{y}_3, \boldsymbol{y}_4\} \tag{4.43}$$

with column vectors $\boldsymbol{y}_i$. $\boldsymbol{a}_i$ are column vectors with components

$$(\boldsymbol{a}_i)_j = a_{ij}. \tag{4.44}$$

From (4.38) and (4.42) the equation for $\boldsymbol{Y}$ is stated

$$\frac{d}{dx}\boldsymbol{Y}(x,s) = \boldsymbol{M}_u\boldsymbol{Y}(x,s). \tag{4.45}$$

We choose the "initial conditions" at $x = -A$ for $\boldsymbol{Y}$ to be

$$\boldsymbol{Y}(-A,s) = \boldsymbol{I}. \tag{4.46}$$

Here $\boldsymbol{I}$ is the 4×4 identity matrix. Equation (4.45) renders 4 linear coupled differential equations. With the condition (4.46) we can calculate $\boldsymbol{Y}(x,s)$ with a standard numerical routine for ordinary differential equations [61]. The 4 vector functions $\boldsymbol{y}_i$ obviously have linearly independent initial conditions (4.46) such that the linear combination in Eq. (4.41) is valid.

We introduce 4-dimensional unity vectors $(\boldsymbol{e}_j)_i = \delta_{ij}$. From (4.34), (4.35), and (4.38) the boundary conditions at $x = \pm A$ for $\boldsymbol{u}_i$ are seen to be

$$\boldsymbol{e}_1^T\boldsymbol{u}_i = (\boldsymbol{e}_i)_1 \tag{4.47}$$

$$\boldsymbol{e}_2^T\boldsymbol{u}_i = (\boldsymbol{e}_i)_2 \tag{4.48}$$

at $x = -A$ and

$$\boldsymbol{e}_1^T\boldsymbol{u}_i = 0 \tag{4.49}$$

$$\boldsymbol{e}_2^T\boldsymbol{u}_i = 0 \tag{4.50}$$

at $x = -A$. In matrix form these boundary conditions become

$$\boldsymbol{Q}(s)\boldsymbol{a}_i(s) = \boldsymbol{e}_i \tag{4.51}$$

where

$$\boldsymbol{Q}(s) = \begin{Bmatrix} \boldsymbol{e}_1^T\boldsymbol{Y}(-A,s) \\ \boldsymbol{e}_2^T\boldsymbol{Y}(-A,s) \\ \boldsymbol{e}_1^T\boldsymbol{Y}(A,s) \\ \boldsymbol{e}_2^T\boldsymbol{Y}(A,s) \end{Bmatrix}. \tag{4.52}$$

The shall need the adjoint of the matrix $\boldsymbol{Q}$ for the system determinant:

$$\boldsymbol{Q}^{\dagger}(s) = \{\boldsymbol{q}_1, \boldsymbol{q}_2, \boldsymbol{q}_3, \boldsymbol{q}_4\} \tag{4.53}$$

with column vectors

$$\boldsymbol{q}_1(s) = \boldsymbol{Y}^{\dagger}(-A, s)\boldsymbol{e}_1 \tag{4.54}$$

$$\boldsymbol{q}_2(s) = \boldsymbol{Y}^{\dagger}(-A, s)\boldsymbol{e}_2 \tag{4.55}$$

$$\boldsymbol{q}_3(s) = \boldsymbol{Y}^{\dagger}(A, s)\boldsymbol{e}_1 \tag{4.56}$$

$$\boldsymbol{q}_4(s) = \boldsymbol{Y}^{\dagger}(A, s)\boldsymbol{e}_2. \tag{4.57}$$

Because of Eq. (4.46) $\boldsymbol{Q}$ becomes

$$\boldsymbol{Q}(s) = \left\{ \begin{array}{c} \boldsymbol{e}_1^T \\ \boldsymbol{e}_2^T \\ \boldsymbol{e}_1^T\boldsymbol{Y}(A, s) \\ \boldsymbol{e}_2^T\boldsymbol{Y}(A, s) \end{array} \right\}. \tag{4.58}$$

The vectors $\boldsymbol{a}_i(s)$ are calculated through

$$\boldsymbol{a}_i(s) = \boldsymbol{Q}^{-1}(s)\boldsymbol{e}_i \qquad i = 1, 2 \tag{4.59}$$

whereby $\boldsymbol{u}_i$ can be found. The system determinant is given as

$$D(s) = \det\boldsymbol{Q}^{\dagger}(s) \tag{4.60}$$

which is simply

$$D(s) = (\boldsymbol{q}_3(s))_3(\boldsymbol{q}_4(s))_4 - (\boldsymbol{q}_3(s))_4(\boldsymbol{q}_4(s))_3. \tag{4.61}$$

We have thus expressed the system determinant in terms of $\boldsymbol{Y}(A, s)$ which can be calculated numerically. By studying the complex zeroes of $D(s)$ we will be able to determine the stability properties of a given stationary solution. The reason for the Hermitian conjugation "†" in (4.60) is that $\boldsymbol{Q}(s)$ appears in the denominator when calculating $\boldsymbol{a}_i$. Therefore it is the complex conjugate that appears in Eq. (4.31).

4.2 Local Stability

We introduce the stability parameter σ

$$\sigma = \frac{d}{ds}D(0). \tag{4.62}$$

In Appendix C it is shown that for large positive s the system determinant $D(s)$ is given as

$$D(s) \simeq \frac{1}{4}s' e^{2\sqrt{2s'}A} \tag{4.63}$$

where $s' = (2k_r/v_g)s$. Then $D(s) \to +\infty$ for real $s \to +\infty$. Below, we also show that $D(s)$ has a fixed zero at $s = 0$. These two properties of $D(s)$ imply the following: If $\sigma < 0$ then $D(s)$ is negative in an interval $(0, s_0)$ on the real s-axis and $D(s)$ has an odd number of zeroes since $D(s) \to +\infty$ for real $s \to +\infty$. Hence, if $\sigma < 0$ for a given stationary solution, it is unstable and its instability is of the saddle-point type. In case $\sigma > 0$, we declare the mode locally stable. If $\sigma > 0$, the given mode can, however, not be declared globally stable since there may be zeroes of $D(s)$ in the right half s-plane off the real axis. In principle, when $\sigma > 0$, $D(s)$ may have an even number of zeroes on the real axis in the right half s-plane. However, after doing some tests we have not seen this happening. Regardless, when $\sigma > 0$ further investigations must be carried out before calling a mode at a given pump rate globally stable. A method to analyze global stability is described in a subsequent section. When calculating σ as a function of the pump current a change in the sign of σ implies a saddle-point bifurcation. For $\sigma = 0$ we are at a bifurcation point where two or more tuning curves meet in a $(J/J_0, \hat{f})$-diagram.

To make use of σ we must first show that $D(s)$ has a fixed zero in $s = 0$. From Eq. (4.45) we obtain

$$\frac{d}{dx}\boldsymbol{Y}^\dagger(x,s) = \boldsymbol{Y}^\dagger(x,s)\boldsymbol{M}_u^\dagger \tag{4.64}$$

The second column of $\boldsymbol{M}_u^\dagger$ is seen to be

$$\boldsymbol{M}_u^\dagger \boldsymbol{e}_2 = -s\frac{2k_r}{v_g}\boldsymbol{e}_3 \tag{4.65}$$

Multiplying by $\boldsymbol{e}_2$ on both sides of (4.64) and then using (4.65) give

$$\frac{d}{dx}\boldsymbol{Y}^\dagger(x,s)\boldsymbol{e}_2 = -s\frac{2k_r}{v_g}\boldsymbol{Y}^\dagger(x,s)\boldsymbol{e}_3. \tag{4.66}$$

In the limit of $s = 0$ it follows that

$$\frac{d}{dx}\boldsymbol{Y}^\dagger(x,s)\boldsymbol{e}_2 = 0 \tag{4.67}$$

and $\boldsymbol{Y}^\dagger(x,s)\boldsymbol{e}_2$ (i.e. the second row of $\boldsymbol{Y}^*$) is thus constant and equal to its initial value. That is,

$$\boldsymbol{q}_4(0) = \boldsymbol{Y}^\dagger(-A,0)\boldsymbol{e}_2 = \boldsymbol{e}_2 \tag{4.68}$$

Of course when calculating $\boldsymbol{Y}$ numerically, this should hold true which we indeed find it to do. Inserting (4.68) in Eq. (4.61) leads to

$$D(0) = 0. \tag{4.69}$$

Thus $D(s)$ has a fixed zero at $s = 0$, and σ is a valid parameter deciding the local stability of a calculated stationary solution. This makes it considerably easier to learn about the local stability of a mode, in fact we will now derive a semianalytical expression for σ in terms of the matrix $\boldsymbol{Q}$ so that a direct numerical calculation of the derivative $dD(0)/ds$ using finite differences becomes unnecessary.

By Eqs. (4.61) and (4.68) we find

$$\frac{d}{ds}D(0) = (\boldsymbol{q}_3(0))_3\frac{d}{ds}(\boldsymbol{q}_4(0))_4 - (\boldsymbol{q}_3(0))_4\frac{d}{ds}(\boldsymbol{q}_4(0))_3 \tag{4.70}$$

or by using (4.56) and (4.57)

$$\frac{d}{ds}D(0) = (\boldsymbol{y}_3(A,0))_1\frac{d}{ds}(\boldsymbol{q}_4(0))_4 - (\boldsymbol{y}_4(A,0))_1\frac{d}{ds}(\boldsymbol{q}_4(0))_3. \tag{4.71}$$

To obtain the derivative $\frac{d}{ds}\boldsymbol{q}_4$ for $s = 0$, we differentiate (4.66) with respect to s and then take the limit $s \to 0$:

$$\frac{\partial^2}{\partial x \partial s}\boldsymbol{Y}^\dagger(x,0)\boldsymbol{e}_2 = \frac{-2k_r}{v_g}\boldsymbol{Y}^\dagger(x,0)\boldsymbol{e}_3. \tag{4.72}$$

Integrating Eq. (4.72) gives

$$\frac{\partial}{\partial s}\boldsymbol{Y}^\dagger(x,0)\boldsymbol{e}_2\Big|_{x=-A}^{x=A} = -\frac{2k_r}{v_g}\int_{-A}^{A}\boldsymbol{Y}^\dagger(x,0)\boldsymbol{e}_3 dx. \tag{4.73}$$

As $\boldsymbol{Y}^{\dagger}(x,s) = \boldsymbol{I}$ at $x = -A$ for all s, we use Eq. (4.57) to end up with

$$\frac{d}{ds}\boldsymbol{q}_4(0) = -\frac{2k_r}{v_g}\int_{-A}^{A}\boldsymbol{Y}^{\dagger}(x,0)\boldsymbol{e}_3 dx = -\frac{2k_r}{v_g}\int_{-A}^{A}[(\boldsymbol{y}_1)_3\,(\boldsymbol{y}_2)_3\,(\boldsymbol{y}_3)_3\,(\boldsymbol{y}_4)_3]^{\dagger}dx. \tag{4.74}$$

The i'th component of the vector $\frac{d}{ds}\boldsymbol{q}_4(0)$ is then

$$\left(\frac{d}{ds}\boldsymbol{q}_4(0)\right)_i = -\frac{2k_r}{v_g}\int_{-A}^{A}(\boldsymbol{y}_i(x,0))_3^* dx. \tag{4.75}$$

With (4.75) the stability parameter σ can be calculated from Eq. (4.71) when $\boldsymbol{y}_1$ and $\boldsymbol{y}_2$ are known. Note that we have kept the complex conjugate in the integrand in Eq. (4.75) although $\boldsymbol{y}_i$ are always real for $s = 0$. When a saddle-point bifurcation occurs σ is supposed to be zero [71]. Therefore when calculating σ as a function of current we expect it to change sign when the tuning curve along which we are moving branches into one or more additional tuning curves.

4.3 Calculation of y

We briefly comment on the calculation of $\boldsymbol{y}_i$. Antisymmetric stationary solutions have zeroes at $x = 0$. The matrix $\boldsymbol{M}_1$ defined in Eq. (4.16) suffers from a singularity at $x = 0$ when $E_s(x)$ is antisymmetric as seen from Eq. (4.4). When calculating $\boldsymbol{y}_i$ for these odd-parity solutions, we choose to smoothen the "potential" given by $\boldsymbol{M}_1(x)$ at x. We do this by introducing the function $h(x)$

$$h(x) = \frac{x}{x + j\epsilon_y}\frac{df}{dx}. \tag{4.76}$$

Here the entity ϵ_y is a small real number. Obviously as $\epsilon_y \to 0$, $h(x) \to df/dx$. Then for antisymmetric solutitions we replace df/dx by $h(x)$ in $\boldsymbol{M}_1(x)$. In $h(x)$, evaluation of df/dx is still needed for $h(0)$. We avoid this by averaging over the nearest discrete neighboring points: $h(0) \simeq (h(\Delta x_r) + h(-\Delta x_l))/2$. In this way a smooth potential is obtained. The small number ϵ_y is a free parameter whose appropriate value is determined as follows: Denote the pump rate at which σ changes from positive to negative J_σ for a given ϵ_y. For an ϵ_y well large we find that σ will change from positive to negative at a current a bit too high as compared with the bifurcation point on the relevant

tuning curve. Decreasing ϵ_y will lead to a smaller value of J_σ. At some point increasing ϵ_y will not lead to a lower value of J_σ. We find that when this occurs, J_σ will equal the current at which the solution actually bifurcates, i.e. where a new branch emerges on the tuning curve. Typically $\epsilon_y \sim 10^{-6}$ m.

4.4 Global stability

With a stationary solution whose $\sigma > 0$ it is necessary to evaluate its global stability before naming it stable or unstable. In order to determine the global stability of a mode at some current, we must know the signs of the real parts of the zeroes of the system determinant $D(s)$. Instead of finding all zeroes of D we define a real function of the imaginary part of s that will show a peak whenever $D(s) = 0$. Regard the expansion around a zero of $D(s)$ denoted s_0

$$D(s) \simeq b(s - s_0). \tag{4.77}$$

Next, we introduce the ratio

$$\frac{1}{D}\frac{\partial D}{\partial s} \simeq \frac{1}{[s - j\mathrm{Im}(s_0)] - \mathrm{Re}(s_0)} \tag{4.78}$$

and state a function $\rho(s)$, which is defined only for purely imaginary s, i.e. for $\mathrm{Re}(s) = 0$:

$$\rho(s) = \mathrm{Re}\left\{\frac{1}{D}\frac{\partial D}{\partial s}\right\}. \tag{4.79}$$

By comparison with (4.78)

$$\rho(s) \simeq \frac{-\mathrm{Re}(s_0)}{[\mathrm{Im}(s) - \mathrm{Im}(s_0)]^2 + [\mathrm{Re}(s_0)]^2}. \tag{4.80}$$

If $\rho(s)$ is plotted, peaks in the curve will imply $\mathrm{Im}(s) = \mathrm{Im}(s_0)$. Thus at $\mathrm{Im}(s) = \mathrm{Im}(s_0)$

$$\rho(s) \simeq -\frac{1}{\mathrm{Re}(s_0)}. \tag{4.81}$$

Then for $\rho(s = \mathrm{Im}(s_0)) < 0$ for a given zero, the viewed mode is unstable at the given current as it implies a positive $\mathrm{Re}(s_0)$. In contrast if $\rho(s = \mathrm{Im}(s_0)) > 0$ the zero does not contribute to an instability since $\mathrm{Re}(s_0) < 0$ in this case.

The function $\rho(s)$ is calculated numerically using Eq. (4.61) and a finite difference is used to obtain the derivative $\frac{\partial D}{\partial s}$. The derivative $\frac{\partial D}{\partial s}$ for $s \to 0$ calculated numerically should of course agree with σ. We find this to be the case.

4.5 Results of stability analysis

4.5.1 Local stability of type I modes

In Figure 3.2 we saw how type II modes were born in conjunction with branches emerging from the branches of type I modes. We expect a saddle-point bifurcation to occur when varying the bifurcation parameter (the pump rate) through a value where a branch point is located. However we cannot *a priori* tell which branches are locally stable or unstable. With the stability parameter σ, however, we are able to determine the local stability of a mode as a function of the bifurcation parameter. A type I mode undergoes a saddle-point bifurcation in conjunction with an emerging type II asymmetric mode. E.g. mode 5 bifurcates at approximately $J = 1.0113J_0$. This family of saddle-point bifurcations is seen to occur at an increasingly high current for increasing mode number. In Figure 3.2 there are 8 such bifurcations (for $m = 1$ the 1^{II}-branch is not visible as it lies close to the 1^{II}-branch).

Figure 4.1 shows examples of calculated σ-curves for type I modes. The regarded modes are 1^I, 3^I,4^I, and 5^I. The question we want the small-signal analysis to answer is: on which side of the bifurcation point is $\sigma > 0$ yielding local stability and on which side is $\sigma < 0$ yielding local instability. σ must cross zero at the pump rate of the bifurcation point (where m^{II} emerges) to be in agreement with bifurcation theory.

Very reassuringly, indeed the σ-curves cross zero at the respective values of the pump rate that correspond to the values where the modes bifurcate and type II modes emerge! Moreover, the actual result from the local stability analysis is that $\sigma > 0$ for pump rates below the bifurcation point and $\sigma < 0$ above the bifurcation point. We hence find that the m^I-modes are locally stable on the interval of the pump rate going from threshold to the bifurcation point and lose their stability for higher pump rates. We have found this to be the case for all m^I with $1 \leq m \leq 8$. In order to be able to conclude that all m^I-modes carry this behavior we also investigated mode 15^I, for which σ turns negative at $1.037J_0$. Again, this is the pump rate at which 15^{II}

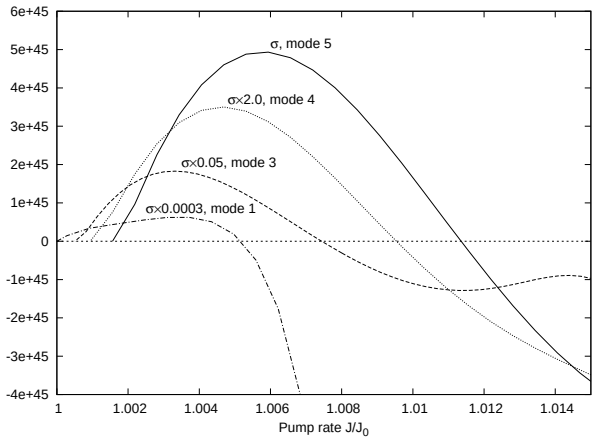

Figure 4.1: σ as a function of pump rate for modes 1^I, 3^I, 4^I, and 5^I. The curves cross zero where their corresponding stationary states saddle-point bifurcate. This means that modes m^I are locally stable for pump rates below the pump rate at which m^{II} emerge.

emerges.

We are rather confident that the above picture holds true for all m. Of course no mathematical proof has been given here. Recall that m^{II} is doubly degenerate for a given m; both a left- and a right-m^{II} exist. Therefore two (not one) branches emerge from the bifurcation point. Consequently we can label the saddle-point bifurcations regarded here as pitchfork bifurcations [72].

4.5.2 Local stability of type II modes

Bifurcation theory predicts that the emerging type II branches correspond to locally stable modes m^{II} since m^I turned unstable for currents above the respective bifurcation points. A similar case where a symmetric solution saddle-point bifurcates into an asymmetric one can be seen for DFB lasers [71]. At the bifurcation point where type I meets type II for some m, $\sigma = 0$ and their field distributions are identical. However, while σ becomes negative for m^I as the current is increased, σ for m^{II} increases from zero to an increasingly large positive value as the current becomes higher. The asymmetric modes m^{II} are hence locally stable. As an example, 6^{II}, $\sigma(J)$ is presented in Fig. 4.2. The truncation of σ-curves at the lower-current end is

tricky as the fields of m^I and m^{II} become very similar near the bifurcation point. Regardless, we find that all m^{II} are locally stable since $\sigma(J)$ increases uniformly. The result that type II modes are locally stable is interesting considering results of chapter 3. The far-fields of m^{II} at currents well above the bifurcation points at which they emerge are single-lobed and relatively coherent spatially. We note that we have not investigated the behavior of σ near the pump rates at which m^{II} merge with $(2m)^{II}$.

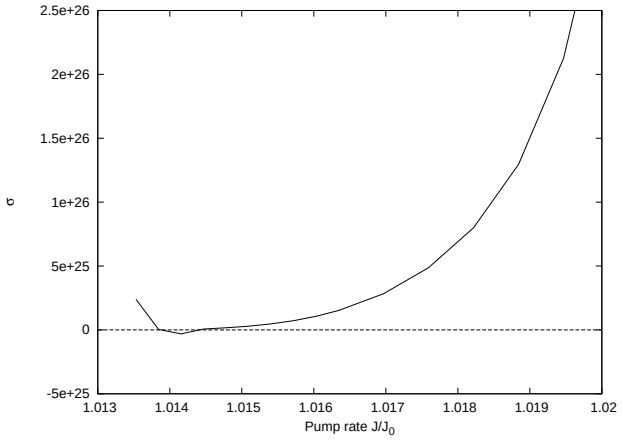

Figure 4.2: σ as function of pump rate. Above the pump rate of the bifurcation point where the branch for 6^{II} emerges from 6^I, $\sigma > 0$ and uniformly increasing with increasing pump rate.

4.5.3 Global stability of type I modes

From the analysis of the local stability of modes m^I we found above that these modes were stable for pump rates going from their respective thresholds to the bifurcation point involving m^{II} at which they underwent a saddle-point bifurcation thus losing their local stability. In this current range the global stability is now investigated using the function $\rho(s)$ defined in Eq. (4.79).

Let us begin with the fundamental mode 1^I for which the results can be summarized in short terms: Mode 1^I is globally stable from its threshold pump rate $J = 1.0001J_0$ until it already Hopf-bifurcates at approximately $J = 1.0010J_0$. Note how 1^I becomes unstable at a current that is higher than the threshold current of 2^I. Also as a reference, 1^I saddle-point bifurcates at $J \simeq 1.005J_0$. To illustrate how the Hopf-bifurcations occur, we show

$\rho(s)$ for the case of 1^I in Figure 4.3 whose abscissa is $\mathrm{Im}(s)/(2\pi)$. Graph 1 corresponds to a pump rate of $J = 1.00028J_0$. At this pump rate there are no peaks below zero, and 1^I is stable. Graph 2 represents a higher pump rate $J = 1.00153J_0$. Here two peaks have become negative corresponding to 2 pairs of complex conjugate zeroes of $D(s)$ moving into the right half s-plane. These two Hopf-bifurcations occur where $\mathrm{Im}(s)/(2\pi)$ is approximately 0.2 GHz and 0.5 GHz. These two frequencies reveal side-mode coupling for 1^I to mode 2^I and mode 3^I, respectively, since the modespacings between 1^I and 2^I and between 1^I and 3^I in Figure 3.2 lie very close to these Hopf-frequencies. Note that since the 0.2 GHz-peak is less sharp than the 0.5 GHz-peak, the pair of zeroes corresponding to 0.2 GHz-peak have entered the right half s-plane for a lower current than the pair of zeroes corresponding to the 0.5 GHz-peak. For a further augmentation of the current, more and more negative peaks appears as seen from graph 3, which has 3 negative peaks.

Similar behavior is seen for mode 2^I which is globally stable from its threshold at $J = 1.00035J_0$ until it Hopf bifurcates at $1.00160J_0$. The evolution of $\rho(s)$ for 2^I is given in Figure 4.3. Graph 1 represents $J = 1.00053J_0$. Graph 2 is calculated at $J = 1.00163J_0$ where a peak is seen to have turned negative at 0.7 GHz. It should be noted that since 2^I is antisymmetric we must rely on the parameter ϵ_y. Therefore the current at which 2^I bifurcates and the frequency s of the instability may depend on the utilized value of ϵ_y. By comparing Figure 4.4 where the detuning of the zeros crossing the imaginary s-axis is 0.7 GHz with Figure 3.2 where 4^I lies 0.7 GHz above 2^I tells us that, most likely, the lowest-current Hopf-bifurcation of 2^I is associated with side-mode coupling to 4^I.

Modes $m \geq 3$ lose their stability immediately above their thresholds. Alternatively they are all "born" unstable. As an example, the stability of mode $m = 3$ was evaluated at $\sim 2 \cdot 10^{-5}J_0$ above its threshold where the mode is clearly unstable with two negative peaks in $\rho(s)$.

As an example of ρ for $m \geq 3$, Figure 4.5 displays $\rho(s)$ for mode 5^I for 3 different currents. Graph 1 is calculated at $J = 1.00188J_0$ corresponding to $7 \cdot 10^{-5}J_0$ above modal threshold. Graphs 2 and 3 represent higher currents, where more and more peaks become negative. For the sake of generality we have in addition to the cases of $1 \leq m \leq 8$ calculated ρ for the higher order mode 15^I and we find ρ to have several negative peaks immediately above threshold. Hence, we find good reason to believe that all modes of type m^I for $m \geq 3$ are globally unstable immediately above threshold and most likely remain unstable for all higher currents.

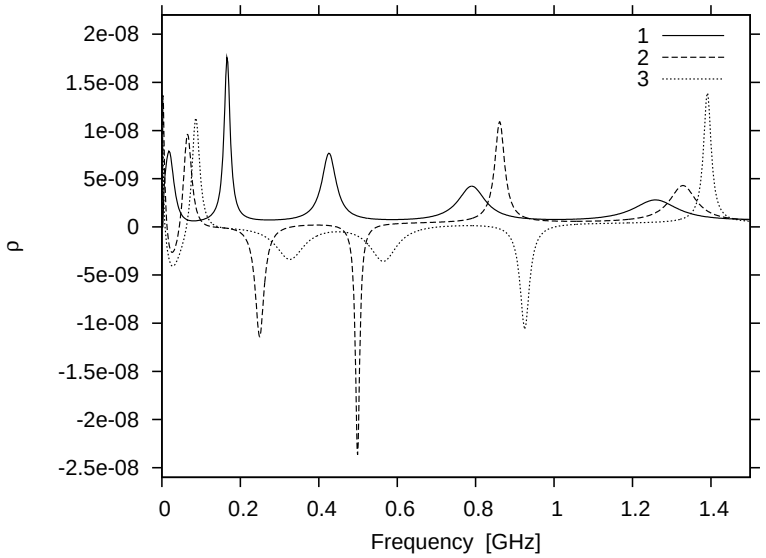

Figure 4.3: Mode 1^I: ρ is plotted as a function of frequency $\mathrm{Im}(s)/(2\pi)$ for 3 different pump rates. Graph 1: For $J = 1.00028J_0$, ρ has no peaks with negative values and the mode is therefore globally stable. Graph 2: For $J = 1.00153J_0$, 2 peaks have become negative at 0.2 GHz and 0.5 GHz and the mode is globally unstable. Graph 3: For $J = 1.00247J_0$, a third peak has become negative. When increasing the pump rate even further, more more peaks will turn negative.

It is intuitively appealing that 1^I does not lose its stability at a current where no other modes are above their threshold, since one associates a Hopf-bifurcation with one or several emerging side-modes through side-mode coupling. There have been reports on experimental configurations designed to make BA lasers operate in the fundamental lateral mode only [64]. These schemes rely on making the losses of the fundamental mode considerably lower than those of the higher order modes by means of spatial filtering. With the notion that the fundamental mode cannot Hopf-bifurcate at a current below the threshold currents of the modes of higher order, such filtering schemes not only ensure that the fundamental mode be the only mode above threshold but also ensure its global stability at currents higher than the current at which it loses its stability in a solitary laser. It is also conceivable that modes of higher order than 2 can be stable if by some means they are filtered to have the lowest threshold current; see [73].

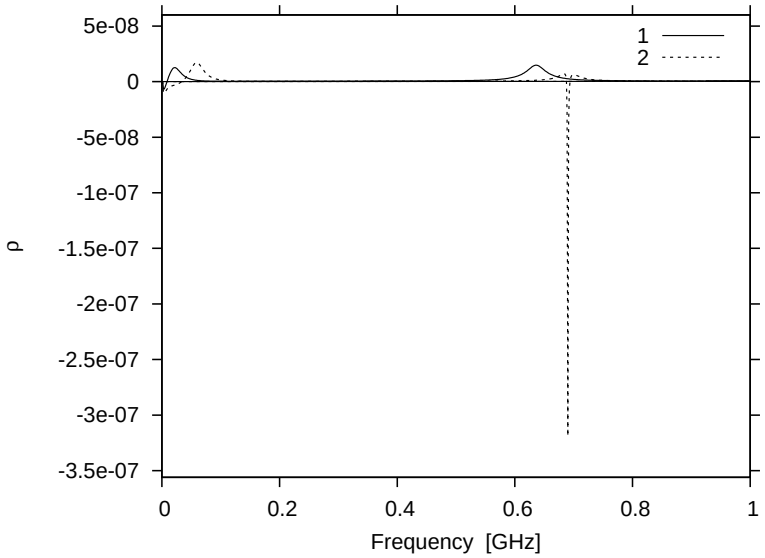

Figure 4.4: Mode 2^I: ρ is plotted as a function of frequency $\mathrm{Im}(s)/(2\pi)$ for 2 different pump rates. Graph 1: For $J = 1.000531J_0$, ρ has no peaks with negative values and the mode is therefore globally stable. Graph 2: For $J = 1.00163J_0$, a peak has turned negative at 0.7 GHz and the mode is globally unstable.

We have seen that the fundamental mode 1^I loses its global stability at a very low pump rate, namely $1.0010J_0$ (again, its threshold was $1.0001J_0$). In [25] a 100 micron-wide AlGaAs BA laser operating at 810 nm was investigated near its threshold (recall that we study a laser of width $w = 200\,\mu$m). It was found that the single mode operation with the fundamental mode stopped at a current $1.01I_0$ where instabilities set in. It must be noted that an external cavity with a plane mirror (no spatial filtering) was included in the set-up. However, a plane external mirror has not been found to stabilize lateral behavior in a BA laser [24]. Therefore we believe that it is relevant to compare our results with this experiment. Most likely the lateral mode-coupling becomes stronger with increasing width and a 200-micron wide laser made from the same wafer as the device in [25] would suffer from an instability at a lower current when normalizing by the respective threshold currents due to the smaller lateral modespacing. We must also remember that the parameter values in our calculations are not taken from a specific device. In any case, the experiment reports a very low pump rate as "threshold" for

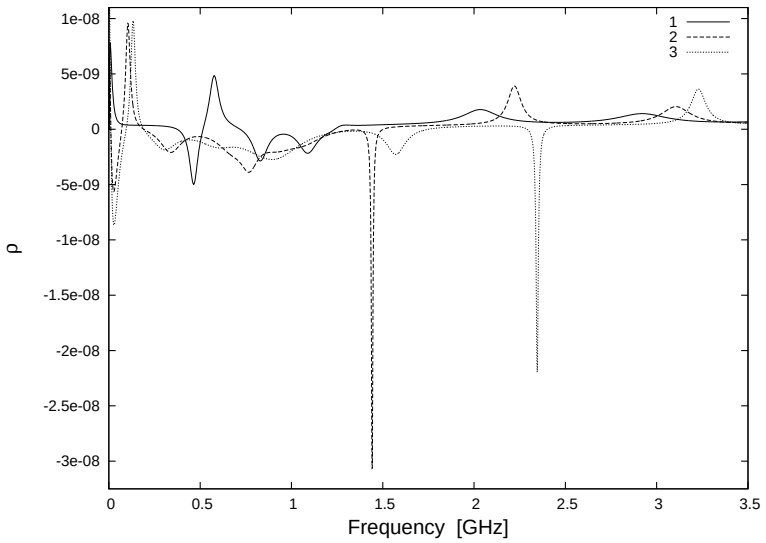

Figure 4.5: Mode 5^I: ρ is plotted as a function of frequency $\mathrm{Im}(s)/(2\pi)$ for 3 different pump rates. Graph 1: For $J = 1.001875J_0$, very close to modal threshold, ρ has several negative peaks and the mode is therefore globally stable. Graph 2 and Graph 3: When increasing the pump rate more and more peaks become negative.

lateral instabilities, suggesting that our small-signal analysis can give good predictions on the lateral modal behavior of a BA laser at very low pump rates.

4.5.4 Global stability of type II modes

We found earlier that modes m^{II} were locally stable. However, we find all type II modes to be globally unstable. For $m > 1$, $\rho(s)$ behaves similarly to $\rho(s)$ for m^I (for $m \geq 3$). The mode 1^{II} stands out to a small degree by having a low-frequency instability: at currents very close to the branch point where 1^{II} is born the mode only has a zero causing a low-frequency instability at around 50 MHz. The explanation for this is most likely a coupling to 2^{II} which lies 50 MHz above 1^{II} in the tuning diagram. However already at around $J = 1.0065J_0$ a higher-frequency instability at 0.66 GHz appears; probably in conjunction with mode 4^I according to the tuning curves. Regardless of this small abnormality, we have not found globally stable type II

modes.

4.5.5 Summary of stability properties

By investigating the small-signal stability properties of modes of type I and type II we conclude that in a solitary BA laser with the parameter values used here, only modes 1^I and 2^I are globally stable at very low pump rates only. One experimental report for a 100 micron-wide BA laser confirms that indeed stable, single-mode operation can only occur at very low pump rates.

All modes m^I are locally stable for pump rates lower than the one at which a saddle-point bifurcation occurs in conjunction with the birth of m^{II}. However they are globally unstable immediately above threshold for $m \geq 3$. Modes m^{II} were found to be globally unstable for all m. Since they are locally stable they may in principle operate in some time-dependent state (just as m^I may for pump rates where they are locally stable). Since m^{II} could be related to the time-averaged single-lobed far-field of the AEC laser, this is of our interest. However, since the AEC laser is a device that usually operates at high pump rates, we can not conclude anything about this based on our analysis at low currents.

Why do BA lasers in general not operate in a single lateral (per longitudinal) mode but rather in an either multimode state or a complex apparently chaotic state? In general terms the above stability analysis has given the small-signal answer to this question: All modes are unstable except for pumping at very low currents.

We have not investigated the stability of modes m^{III} and m^{IV}. We leave this to future work. Even if some of these modes are stable, which one could intuitively doubt, then they will probably not be seen in a solitary BA laser where the large-signal behavior appears to be chaotic. The trajectory in some phase-space will never find a stable stationary solution when the BA laser is well above threshold. In general one cannot expect that a laser will operate in a cw-mode even if one or more stable stationary solutions exist. For example, in external cavity lasers (with one lateral mode) with strong optical feedback, time-domain calculations show that limit-cycle operation, chaotic behavior, and mode hopping may occur in spite of the presence of stable stationary solutions [74].

4.6 Linewidth

We move on to demonstrate the use of Eq. (4.31). In this section we will calculate the linewidth for mode 1^I. The linewidth is the low frequency limit of the frequency noise spectrum. To calculate small-signal noise spectra from using (4.31) one must know the diffusion matrix $\boldsymbol{D}(x,s)$ in the correlation relation for $\widetilde{\boldsymbol{f}}(x,s)$

$$\left\langle \widetilde{\boldsymbol{f}}(x,s)\widetilde{\boldsymbol{f}}^{\dagger}(x,s)\right\rangle = \boldsymbol{D}(x,s)\delta(x-x')2\pi\delta(\Omega-\Omega'), \tag{4.82}$$

where $s=j\Omega$, $s'=j\Omega'$, and "$\langle\rangle$" denotes ensemble averaging. In Appendix D the diffusion matrix is determined from the correlation relations for the Langevin noise function $F_\omega(x,y,z)$ in Eq. (3.7). The diffusion matrix is approximated to be independent of frequency

$$\boldsymbol{D} \simeq \frac{D_f(x,\omega_s)}{2|E_s|^2}\boldsymbol{I}, \tag{4.83}$$

where

$$D_f(x,\omega_s) \simeq \frac{2\omega_s^3\hbar}{c^3\epsilon_0 l}Kn_r g n_{sp}. \tag{4.84}$$

The inversion factor n_{sp} is given by [75]

$$n_{sp} = \frac{N}{N-N_0}. \tag{4.85}$$

The Fourier transform of the instantaneous frequency deviation $\dot{\phi}_E = d(\boldsymbol{\psi})_2/dt$ is $s\widetilde{(\boldsymbol{\psi})}_2$. The frequency noise spectrum is the spectral density of the instantaneous frequency deviation

$$S_{\dot{\phi}_E}(s) = \lim_{T\to\infty}\frac{1}{T}\left\langle |s(\widetilde{\boldsymbol{\psi}})_2(s)|^2\right\rangle \tag{4.86}$$

By inserting (4.31) for $i=2$ and $\widetilde{\boldsymbol{j}}=0$ in Eq. (4.86) while using (4.82) one obtains the expression for the frequency spectrum at $x=-A+$

$$S_{\phi_E}(s) = |s|^2\int_{-\infty}^{\infty}\boldsymbol{\zeta}_2^{\dagger}(x,s)\boldsymbol{D}(x,s)\boldsymbol{\zeta}_2(x,s)dx. \tag{4.87}$$

In the limit $s\to 0$ one obtains the spectral linewidth

$$\Delta\nu = S(0)/2\pi. \tag{4.88}$$

For the purpose of obtaining the linewidth we need to know $\lim_{s\to 0} s\boldsymbol{\zeta}_2$. Let us now derive an expression for $\boldsymbol{\zeta}_2$ in terms of individual components of $\boldsymbol{y}_i$. From Eq. (4.42)

$$\boldsymbol{\zeta}_2(x,s) = \begin{pmatrix} \boldsymbol{e}_3^T \boldsymbol{Y} \boldsymbol{a}_2 \\ \boldsymbol{e}_4^T \boldsymbol{Y} \boldsymbol{a}_2 \end{pmatrix}. \tag{4.89}$$

By Eq. (4.51) and (4.58)

$$\boldsymbol{a}_2^\dagger(s) = \boldsymbol{e}_2^T (\boldsymbol{Q}^{-1})^\dagger = \frac{1}{D(s)} \begin{bmatrix} 0 & 1 & (\boldsymbol{q}_3)_4^*(s) & -(\boldsymbol{q}_3)_3^*(s) \end{bmatrix}. \tag{4.90}$$

and then

$$\boldsymbol{\zeta}_2(x,s) = \frac{1}{D(s)} \begin{pmatrix} (\boldsymbol{y}_2)_3 + (\boldsymbol{y}_3)_3 (\boldsymbol{y}_4(A))_1 - (\boldsymbol{y}_4)_3 (\boldsymbol{y}_3(A))_1 \\ (\boldsymbol{y}_2)_4 + (\boldsymbol{y}_3)_4 (\boldsymbol{y}_4(A))_1 - (\boldsymbol{y}_4)_4 (\boldsymbol{y}_3(A))_1 \end{pmatrix}. \tag{4.91}$$

In (4.91) all $\boldsymbol{y}_i$ are functions of s respectively x except those evaluated in $x = A$. The definition of σ in Eq. (4.62) gives

$$\lim_{s\to 0} s\boldsymbol{\zeta}_2(x,s) = \frac{1}{\sigma} \begin{pmatrix} (\boldsymbol{y}_2)_3 + (\boldsymbol{y}_3)_3 (\boldsymbol{y}_4(A))_1 - (\boldsymbol{y}_4)_3 (\boldsymbol{y}_3(A))_1 \\ (\boldsymbol{y}_2)_4 + (\boldsymbol{y}_3)_4 (\boldsymbol{y}_4(A))_1 - (\boldsymbol{y}_4)_4 (\boldsymbol{y}_3(A))_1 \end{pmatrix}. \tag{4.92}$$

In (4.92) all $\boldsymbol{y}_i$ are functions of x except those evaluated in $x = A$. Having obtained $s\boldsymbol{\zeta}_2$ in the limit $s \to 0$ we can calculate the linewidth from (4.87) using (4.92) and (4.83). Figure 4.6 displays the calculated linewidth of 1^I for two different pump rates. The linewidth at $J = 1.009 J_0$, just below the pump rate at which the mode Hopf-bifurcates is found to be $\Delta\nu = 8.0$ GHz. For $J = 1.00028 J_0$, close to its threshold $J = 1.0001 J_0$, the linewidth $\Delta\nu = 33.0$ GHz. One expects the linewidth of a laser to drop for increasing current near threshold [76].

One could proceed to calculate the full frequency spectrum in (4.87) and other types of noise spectra. We have not succeeded in doing so as of yet.

4.7 Static Frequency tuning

With the general expression Eq. (4.31) one can also calculate the response due to a current modulation $\widetilde{\delta J}(x,s)$ by inserting the current modulation term (4.22) in (4.31) and setting $\widetilde{\boldsymbol{f}} = 0$. The change in frequency when the current is changed staticly is then given by

$$\delta\omega(0) = k_r \Gamma a \int_{-A}^{A} \lim_{s\to 0} s\boldsymbol{\zeta}_2^\dagger(x,s) \begin{pmatrix} \alpha \\ -1 \end{pmatrix} \frac{\tau_R \widetilde{\delta J}(x,s)}{1 + |E_s(x)|^2/P_{sat}} dx. \tag{4.93}$$

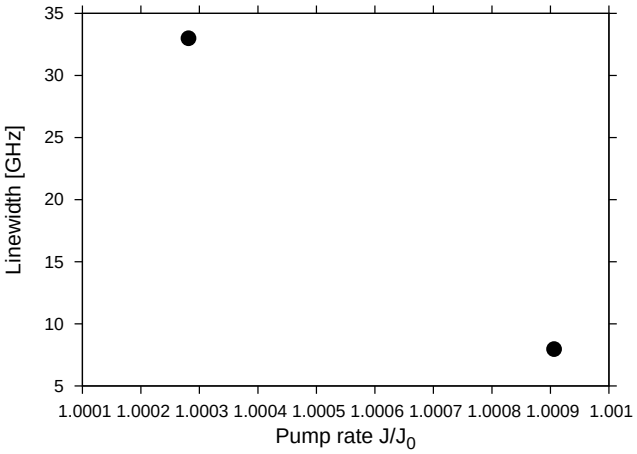

Figure 4.6: The linewidth of mode 1^I calculated for two pump rates. At $J = 1.001J_0$, the mode Hopf-bifurcates.

where we again use the contracted notation $\boldsymbol{\zeta}_2^\dagger(x,s) \equiv \boldsymbol{\zeta}_2^\dagger(x,-A+,s)$. Using Eq. (4.36)

$$\boldsymbol{\zeta}_2^\dagger(s,x)\begin{pmatrix}\alpha\\-1\end{pmatrix} = \alpha(\boldsymbol{u}_2(x,s))_3 - (\boldsymbol{u}_2(x,s))_4 = \boldsymbol{u}_2^\dagger(x,s)(\alpha\boldsymbol{e}_3 - \boldsymbol{e}_4) \quad (4.94)$$

and then inserting the adjoint of $\boldsymbol{u}_2$ from Eq. (4.42) gives

$$\boldsymbol{\zeta}_2^\dagger(x,s)\begin{pmatrix}\alpha\\-1\end{pmatrix} = \boldsymbol{a}_2^\dagger \boldsymbol{Y}^\dagger(x,s)(\alpha\boldsymbol{e}_3 - \boldsymbol{e}_4). \quad (4.95)$$

By Eq. (4.51) and (4.58)

$$\boldsymbol{a}_2^\dagger(s) = \boldsymbol{e}_2^T(\boldsymbol{Q}^{-1}(s))^\dagger = \frac{1}{D(s)}\begin{bmatrix} 0 & 1 & (\boldsymbol{q}_3(s))_4^* & -(\boldsymbol{q}_3(s))_3^* \end{bmatrix}. \quad (4.96)$$

Using the definition of σ in Eq. (4.62) we obtain

$$\lim_{s\to 0} s\boldsymbol{a}_2^\dagger = \frac{1}{\sigma}\begin{bmatrix} 0 & 1 & (\boldsymbol{y}_4)_1(A) & -(\boldsymbol{y}_3)_1(A) \end{bmatrix}. \quad (4.97)$$

Then it follows that,

$$\lim_{s\to 0} s\boldsymbol{\zeta}_2^\dagger(s,x)\begin{pmatrix}\alpha\\-1\end{pmatrix} = \\ \sigma^{-1}\left\{(\boldsymbol{y}_4)_1(A)\left[\alpha(\boldsymbol{y}_3)_3(x) - (\boldsymbol{y}_3)_4(x)\right] - (\boldsymbol{y}_3)_1(A)\left[\alpha(\boldsymbol{y}_4)_3(x) - (\boldsymbol{y}_4)_4(x)\right]\right\}. \quad (4.98)$$

The small signal frequency tuning is then obtained by substituting (4.98) into (4.93).

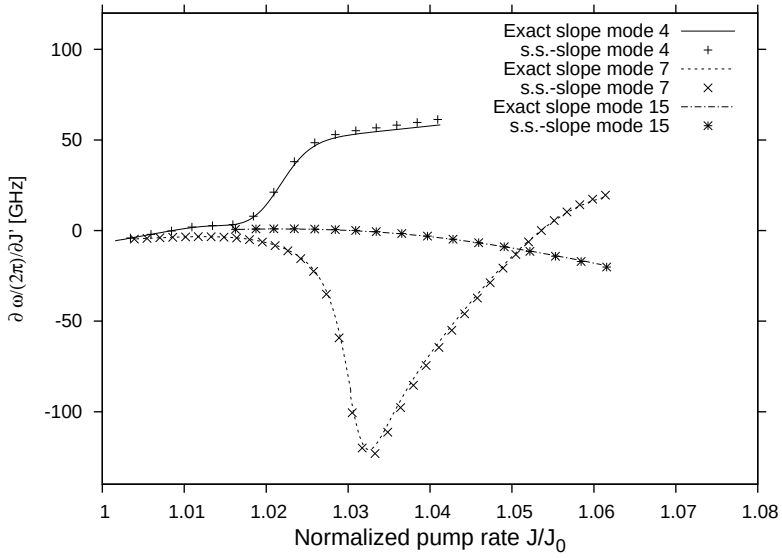

Figure 4.7: Comparison between small-signal frequency tuning denoted s.s.-slope and the exact slope of tuning curves denoted "Exact slope" for modes 4^I, 7^I, and 15^I in Fig. 3.2. J' is the normalized pump rate J/J_0.

For a calculated stationary solution in the $(J/J_0, \widehat{f})$-plane it is thus possible to calculate the local slope of the tuning curve by means of the small-signal analysis. By local we mean at the current at which the stationary solution was calculated. We present a few examples of the calculated small-signal frequency tuning as a function of pump current in Fig. 4.7. For modes 4, 7, and 15 (all type I) we first directly calculated the slopes of actual tuning curves in Fig. 3.2. These curves labeled "Exact slope" thus represent the "exact" slope of the tuning curves. The small-signal frequency tuning curves as calculated using Eq. (4.93) are labeled "s.s.-slope". We find that the precision of the small-signal frequency tuning is very good for currents ranging from the threshold of modes m^I to currents past the bifurcation point where modes m^{II} are born. The discrepancy typically increases a little for larger currents.

4.8 Summary

In this chapter we have performed a small-signal analysis on lateral modes in a BA laser. We employed a Green's function approach to include the spatial dependence of the stationary solutions.

The main focus was on a stability analysis. The general result was brutal but in correspondence with the known experimental and theoretical time-domain behavior of BA lasers: Except for the case of very low pump rates, all investigated modes were found unstable. Albeit brutal, the result is appealing from a theoretical point of view since the highly non-stationary output of BA lasers conceivably has its origin in linear instabilities (i.e. instabilities predictable by a small-signal analysis). The only modes found to be globally stable were the two lowest order modes of type I. However, as the pump rate is increased from the threshold of the laser the fundamental mode 1^I becomes unstable at already $J = 1.0010J_0$ and the next higher order mode 2^I loses its global instability at the slightly higher pump rate around $J = 1.0016J_0$. All higher order type I modes are suffer from instabilities of the Hopf-type immediately above threshold. In connection with the birth of type II modes, type I modes bifurcates to also suffer from a saddle-point instability. The asymmetric type II were found to suffer from instabilities of the Hopf-type.

We also demonstrated the calculation of the linewidth of the fundamental lateral mode and found plausible values for the linewidth of a single lateral mode just above threshold. Finally, we showed examples of frequency tuning giving the change in oscillation frequency due to a static change in pump rate.

Chapter 5

Time-domain calculations

The output of BA lasers fluctuates in time and space even at small pump currents. This is known experimentally [25] and from time-domain large-signal theory including microscopic descriptions of the gain material [3][4]. Our analysis of the stationary states and their stability properties are in correspondence with this known behavior; no stationary output from a BA laser is possible except for at very low pump rates. When a stationary state Hopf-bifurcates into a limit cycle it could possibly be recognized in a time-domain simulation at a current just above the current of the bifurcation in case the limit cycle associated with the Hopf-bifurcation is stable. However, judging from the long time reported chaotic behavior of BA lasers, where no perfectly periodic mode of operation is seen for considerable currents, this is only conceivable near threshold. In order to be able to compare results in chapters 3 and 4 with time-domain results, one could also do large-signal time-domain calculations at very low currents and compare spectra obtained from time-domain simulations (large-signal) with noise spectra (small-signal); in particular the field power spectrum. This was done successfully for a single-mode EC laser in [74]. We shall not pursue such a comparison here. Instead we turn to the time-domain considering a higher pump rate, where we seek to imitate the experimentally observed behavior of the asymmetric external cavity (AEC) laser.

Of particular interest here is modeling of the AEC laser. In [73] BPM was utilized for this. The field was propagated through the cavity of the chip and the external cavity until a steady-state was reached. However, at pump currents slightly above threshold, the method becomes unstable, i.e. the field distribution differs from one round-trip to another. BPM being a method for

finding steady-state solutions, such a variation is not acceptable. However, the instability of BPM does add to the suspicion that even with the spatial filtering in the external cavity the AEC laser is not a cw-laser. Therefore we have pursued a time-domain approach. One could also try to extend the methods of chapters 3 and 4 to include an external cavity and perhaps even include the spatial filtering, and then find stationary solutions. In addition a stability analysis should be performed. However, recognizing the complexity of EC lasers in general this could become rather involved.

In the following we integrate the field- and carrier equations in the time-domain and for the AEC laser we add a filtered delay term in the field equation as it will be described. As mentioned in chapter 2, taking the phenomenological description of the semiconductor to the time-domain in a diffractive gain guided system is not without problems. Spatial Fourier components of the field with large spatial frequencies may be amplified unphysically. We have experienced this first-hand by solving the coupled PDEs for the field and the carrier density. The problem can be relieved by implementing an *ad hoc* part found in the literature in the field equation. We discuss this in more detail after the derivation of the needed equations. The advantage of the phenomenological approach as opposed to the microscopic approach is a smaller computational load and also a more transparent description of dynamic filamentation in BA lasers. Furthermore, to be able to compare with our stationary results it is convenient to be able to use the same parameters in the time domain. In the semiconductor Maxwell-Bloch equations, one has to insert dephasing times as parameters. We note that the numerical scheme that we use to solve the PDEs for the field and carrier density can be extended to include a microscopic treatment of the gain material.

5.1 Time-domain equations

In the time-domain we now consider the one-dimensional field equation and carrier-density equation that we obtained from the mean-field approximation. One may call these equations macroscopic. A set of similar one-dimensional macroscopic equations coupled to the semiconductor Maxwell-Bloch equations applied to a BA laser were used in [22] with apparent success. We therefore believe that the one-dimensional treatment of BA lasers in the

time-domain generally is a good approximation.

From Eq. (3.40) the time-domain field equation without external feedback reads

$$\frac{j}{2k_r}\frac{\partial^2}{\partial x^2}E + \frac{1}{v_g}\frac{\partial}{\partial t}E - \frac{1+j\alpha}{2}\Gamma a(N-N_r)E + \left(\frac{\alpha_m}{2}\right)E = f(x,t) \qquad (5.1)$$

where we have assumed $\omega_s = \omega_r$. We choose this frequency to obtain an equation similar to what is commonly found in the literature. In this chapter we include carrier diffusion such that the carrier-density equation becomes

$$\frac{\partial}{\partial t}N(x,t) = \mathscr{J}(x,t) + D\frac{\partial^2}{\partial x^2}N - \frac{N(x,t)}{\tau_R} - v_g g_m(x,t)B|E(x,t)|^2. \qquad (5.2)$$

In the present chapter the current-profile is a square, i.e. for $|x| > x_0$ we set $\mathscr{J} = 0$. Instead the carrier diffusion spreads the current. Further, the lateral boundary conditions are specified as

$$\frac{\partial E}{\partial x} = j\sqrt{\kappa_{WKB}}E \qquad , x = -A \qquad (5.3)$$

and

$$\frac{\partial E}{\partial x} = -j\sqrt{\kappa_{WKB}}E \qquad , x = A \qquad (5.4)$$

for the field. For the carrier density we utilize boundary conditions [77]

$$\frac{\partial N}{\partial x} = c_2 N \qquad , x = -A \qquad (5.5)$$

$$\frac{\partial N}{\partial x} = -c_2 N \qquad , x = A. \qquad (5.6)$$

The constant c_2 is the ratio between the surface recombination velocity and the diffusion coefficient, i.e. $c_2 = v_{sr}/D$ [78]. Thus $x = \pm A$ are considered the lateral boundaries of the chip. We integrate Eqs. (5.1) and (5.2) numerically using the hopscotch method. We return to the subject of this method briefly in Section 5.4 and in Appendix E. In the following two sections we derive an additional term describing external feedback that is to be included in the field equation.

5.2 External feedback without filtering

We now continue to consider a BA laser with an external mirror placed like in Figure 2.2. To get started, we regard the case where the external mirror provides no filtering. The field equation (5.1) shall be extended to include the feedback from an external reflector. Here we consider the case of small to moderate levels of feedback.

When an external reflector is placed in front of the right facet, the effective right reflectivity is the reflectivity of a Fabry-Perot etalon [50]

$$r_R(\omega) = \frac{r_2 + r_3 e^{-j\omega\tau_{ext}}}{1 + r_2 r_3 e^{-j\omega\tau_{ext}}} \tag{5.7}$$

Here r_3 the effective external amplitude reflectivity. The effective reflectivity includes reflection by the external mirror and any losses in the feedback path. τ_{ext} is the round-trip time of the external cavity. If r_3 is small Eq. (5.7) can be approximated using the expansion $1/(1+x) \simeq 1 - x$:

$$r_R(\omega) = r_2 + r_3(1 - r_2^2)e^{-j\omega\tau_{ext}} \tag{5.8}$$

where terms with r_3 of order higher than first have been neglected. Now, instead of the mirror loss of the solitary-laser field $\alpha_m/2 = -\ln r_1 r_2/(2l)$ we must consider the amplitude mirror loss of the compound cavity:

$$-\frac{1}{2l}\ln r_1 r_R = -\frac{1}{2l}\left[\ln(r_1 r_2) + \ln(1 + \gamma e^{-j\omega\tau_{ext}})\right], \tag{5.9}$$

where

$$\gamma = \frac{(1 - r_2^2)r_3}{r_2} \tag{5.10}$$

is the feedback parameter. In the limit of $\gamma \ll 1$ the compound cavity mirror loss can be approximated using $\ln(1+x) \simeq x$:

$$-\frac{1}{2l}\ln r_1 r_R \simeq -\frac{1}{2l}(\ln(r_1 r_2) + \gamma e^{-j\omega\tau_{ext}}). \tag{5.11}$$

Replacing the mirror loss of the solitary laser in Eq. (5.1) with the compound cavity loss in Eq. (5.11) yields the field equation with full (unfiltered) feedback

$$\begin{aligned}\frac{1}{v_g}\frac{\partial}{\partial t}E = &-\frac{j}{2k_r}\frac{\partial^2}{\partial x^2}E + \frac{1+j\alpha}{2}\frac{\partial g}{\partial N}(N - N_r)E \\ &- \frac{\alpha_m}{2}E + \frac{1}{2l}\gamma e^{-j\omega_r\tau_{ext}}E(-x, t - \tau_{ext}) + f(x,t).\end{aligned} \tag{5.12}$$

Eq. (5.12), then, is the field equation introduced by Lang and Kobayahsi [79] except that diffraction is included in (5.12). Note, however, also the negative sign in front of x in the argument of E in the feedback term, as shall be explained in section 5.3. It stems from the cavity of length $2f$, which includes a lens in the middle and therefore two Fourier transforms. The diffraction in the external cavity is thus included in (5.12).

From the view point of applied mathematics, differential equations including a temporally delayed term such as the term including $E(t - \tau_{ext})$ in (5.12) are called delay differential equations. Bifurcation theory and numerical bifurcation packages have been applied to single-mode EC lasers to study the birth of external cavity modes as well as their stability properties when some bifurcation parameter is varied [80]. Of particular interest in this thesis is the inclusion of the lateral dimension x. One possible path to follow is to include the lateral field distribution as a fixed Gaussian shape whose only degree of freedom is to change amplitude, that is to "breathe" as a function of time [81]. By doing so, however, one presumably dismisses the possibility of any lateral instability, which we in Chapter 4 have found to be of great importance for BA lasers, and therefore the stability properties of the external cavity modes in Ref. [81] are very similar to those found without including the lateral dimension, i.e. similar to the stability properties of a single-mode EC laser. Of course a reduced computational load is in favor of this approach, but it can only give insight in the behavior concerning the fundamental lateral mode.

Often the motivation for delayed feedback systems is to stabilize the fluctuating output of the regarded solitary system. If one *a priori* is aware of a characteristic temporal period in an unstable nonlinear system, stabilization of the system may possibly be achieved by using a delay of the known period to obtain a stable motion [82].

5.3 Spatially filtered feedback

Unless some kind of spatial filtering is introduced in the feedback we cannot expect a stabilization of a BA laser. It has been seen experimentally in [24], where a BA laser was subject to an external mirror with no filtering, that no stabilization or spectral narrowing was achieved when compared to a solitary laser. In [83] a BA laser subject to a delayed spatially filtered

feedback was studied theoretically, where the filter function was a Gaussian $\widetilde{F}(k_x) = \exp(-k_x^2/\zeta)$ for some constant ζ. However, the authors regarded an infinite lateral structure, i.e. they imposed no lateral boundary conditions. Such a Gaussian filter has theoretically been shown to stabilize the field of the infinitely wide semiconductor laser otherwise unstable without the external filter [84]. We saw in Chapter 3 that the stationary lateral mode structure is much affected by the lateral gain guiding wherefore the assumption of an infinitely wide structure is mainly of theoretical or rather mathematical interest. As mentioned earlier, feedback from an external mirror with a finite radius of curvature has been shown to have a stabilizing effect on BA lasers experimentally [21] and theoretically [22] where the length of the delay was of significance in addition to the spatial filtering.

We regard the filtering in the Fourier-plane of a laser, see Figure 2.2. A thin lens of focal length f is placed at $(z = l + f)$ and an appropriate filtering reflector is put at $(z = l + 2f)$. The feedback term to be included in the field equation should include propagation from chip to the lens; the phase added to the field by the lens; propagation from lens to the Fourier-plane; reflection and filtering due to the external mirror; and propagation back to the chip through the lens. The crucial thing here is to notice that the Fourier transform due to propagation from chip to the external mirror has the same direction (i.e. the same sign in the exponential function of the Fourier integral) as the one due to the propagation from the external mirror to the chip; the field sees the same lens twice. Thus the filtered field entering the chip becomes

$$E_{fb}(x,t) = r_3(1-r_2^2)e^{-j\omega_r\tau_{ext}}\mathscr{F}\{\widetilde{C}(k_x)\mathscr{F}[E(x,t-\tau_{ext})]\}, \tag{5.13}$$

where $\mathscr{F}$ denotes a forward Fourier transform and $\widetilde{C}(k_x)$ is the filter function in the k_x-domain. Thus

$$E_{fb}(x,t-\tau_{ext}) = r_3(1-r_2^2)e^{-j\omega_r\tau_{ext}}\int\int\int E(x',t-\tau_{ext})C(x'')e^{-jk_x(x'+x''+x)}dx'dx''dk_x \tag{5.14}$$

leading to

$$E_{fb}(x,t) = r_3(1-r_2^2)e^{-j\omega_r\tau_{ext}}\int\int E(x',t-\tau_{ext})C(x'')\delta(-x-x'-x'')dx'dx'' \tag{5.15}$$

and

$$E_{fb}(x,t) = r_3(1-r_2^2)e^{-j\omega_r\tau_{ext}} \int E(x', t-\tau_{ext})C(-x-x')dx' \qquad (5.16)$$

or

$$E_{fb}(x,t) = r_3(1-r_2^2)e^{-j\omega_r\tau_{ext}} \int E(-x-x'', t-\tau_{ext})C(x'')dx''. \qquad (5.17)$$

Note the minus in front of the unprimed x. This sign makes a very significant difference. With a full plane mirror in the Fourier-plane $\widetilde{C}(k_x) = 2\pi \cdot constant$ one gets a delta-function filter function $C(x)$. The minus sign in front of x in the feedback term of (5.12) is justified, and it is in agreement with [30] where BPM was used for a BA laser with unfiltered feedback. For an unfiltered feedback, the minus sign in (5.12) says that the reflected field that reenters the chip through the front facet, reenters at a position opposite to the point at which it was emitted. Omitting the minus sign, i.e. convolving the filter function and field does not represent the optical system displayed in Figure 2.2. In the case of a spatially filtered feedback we find that it causes very different feedback conditions when the minus is left out. We shall return to this point later in this chapter.

With a general spatial filtering we get the field equation

$$\begin{aligned} \frac{1}{v_g}\frac{\partial}{\partial t}E = &-\frac{j}{2k_r}\frac{\partial^2}{\partial x^2}E + \frac{1+j\alpha}{2}\frac{\partial g}{\partial N}(N-N_r)E - \frac{\alpha_m}{2}E \\ &+ \frac{1}{2l}\gamma e^{-j\omega_r\tau_{ext}} \int_{-\infty}^{\infty} C(-x-x')E(x', t-\tau_{ext})dx' + f(x,t). \end{aligned} \qquad (5.18)$$

It should be noted that the filtering in Eq. (5.18) cannot be achieved without a finite distance between the output facet and the filtering reflector because the two Fourier transforms are required. An optical system serves as an attractive environment for combining nonlinear phenomena with delay and filtering.

5.3.1 Single stripe mirror

We consider the filter function relevant for the AEC laser. It represents a single stripe mirror placed in the Fourier plane. Hence the width of the

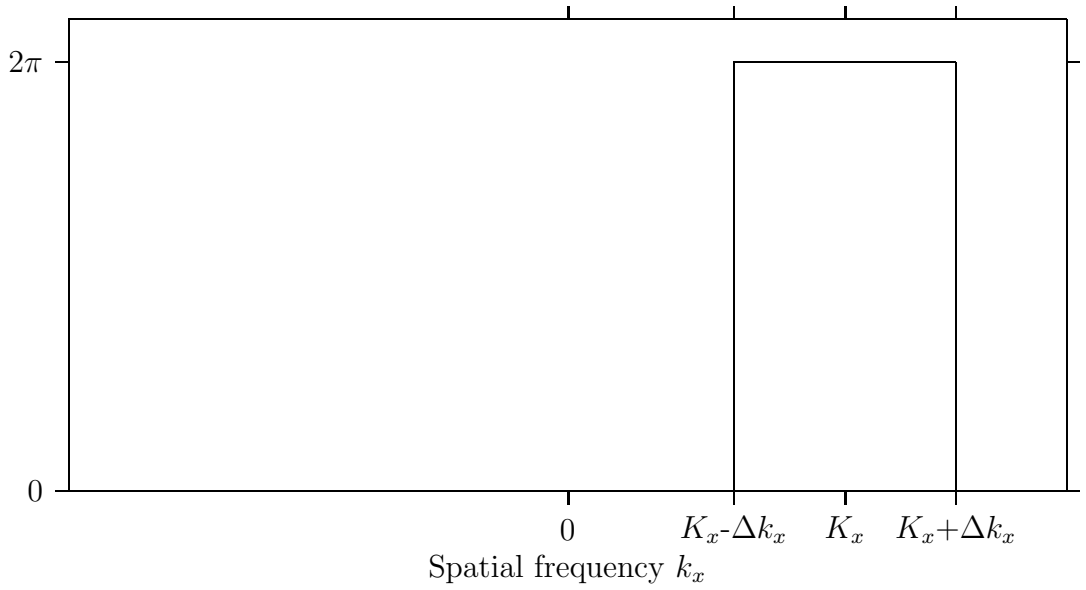

Figure 5.1: Single stripe filter in the k_x-domain.

mirror represents the range in spatial frequency or, alternatively, an angular range. Regard the filter function representing a stripe mirror in the far-field

$$\widetilde{C}(k_x) = 2\pi\frac{1}{2}\left[\mathrm{sgn}(K_x - k_x + \Delta k_x) + \mathrm{sgn}(-K_x + k_x + \Delta k_x)\right] \tag{5.19}$$

where $\mathrm{sgn}(x)$ is the signum function. K_x represents the center of the mirror while Δk_x is the half width in spatial frequency. See Figure 5.1. This filter is the only type considered in this thesis. In position space we get

$$C(x) = \frac{e^{j(\Delta k_x + K_x)x} - e^{-j(\Delta k_x - K_x)x}}{jx}. \tag{5.20}$$

Often one wants the angle in the Fourier plane:

$$\theta = \arcsin\frac{k_x}{k_0}. \tag{5.21}$$

We acknowledge that the actual filter function may be more involved in an experiment. The width of the reflector is sometimes defined by two razor blades in front of the actual reflector. The adjustable distance between the razor blades then translates into a Δk_x. Such an arrangement may cause undesired scattering of light. However, we assume that such scattering losses are included in r_3.

5.4 Hopscotch method

The numerical method utilized in this chapter is the hopscotch method. It is a method originally made to solve the parabolic equation $u_t = u_{xx}$ [85]. It is an explicit-implicit finite-difference scheme which has been found to be very numerically stable [86]. The hopscotch method may also be used for nonlinear PDEs such as Korteweg-de Vries equation [87]. In our case, we are to solve the nonlinear system of PDEs in Eqs. (5.1) and (5.2). Details are given in Appendix E.

We find that the exact values of the "decay constants" in (5.3) through (5.6) are not important as it also found in e.g. [77]. If the boundary conditions on the x-domain are imposed well away from $|x| = x_0$ the field and the carrier density at the boundaries become very small. In an actual device one certainly wants the field to be vanishingly small at the lateral edges of the chip in order to avoid lateral lasing phenomena [88]. Also, it is convenient not having to know the actual magnitude of the surface recombination rate. The noise term in the field equation drives the laser above threshold. We add Gaussian very-low level noise in the simulation. When the laser is above threshold, the effect of the noise is negligible. For purely explicit integration of the PDE $\mathscr{D}u_t = u_{xx}$, one has the numerical stability criterion $\mathscr{D}\Delta t/(\Delta x)^2 < 1$. For comparison we use $v_g/(2k_r)\frac{\Delta t}{(\Delta x)}^2 < 2.5 \cdot 10^{-2}$. As already stated the macroscopic PDEs treated here can be used in conjunction with the semiconductor Maxwell-Bloch equations. Moreover, extending the hopscotch method to include z-dependence appears straight forward. Including the semiconductor Maxwell-Bloch equations and/or 2 spatial dimensions are aimed for large-scale computing. For this purpose the hopscotch method is very well suited for parallel computing [89].

5.5 The problem with adiabatic elimination

When integrating Eqs. (5.1) and (5.2) using the hopscotch method we have experienced first-hand that field components of high spatial frequencies may become amplified in an unphysical manner when the field is calculated with a relatively high spatial resolution. This behavior becomes clear when calculating the far-field, i.e. the spatial spectrum, in which the highest spatial frequencies of the Fourier window grow orders of magnitude above the phys-

ical far-field localized within ±3 degrees around zero degrees (the laser axis). It turns out that the reason for this undesired behavior is not to be blamed on the hopscotch method; it is not a numerical instability. Rather the fault lies in the phenomenological description of the gain and amplitude-phase coupling [41]. Due to the adiabatic elimination of the polarization variable, variations of high spatial and temporal frequency in the permittivity are disregarded. A plane-wave linear stability analysis of equations similar to Eqs. (5.1) and (5.2) shows that plane waves with high k_x grow exponentially when perturbed (they are unstable) [77]. Although this stability analysis deals with a laterally infinite system, it captures that spatial Fourier components of the field with high spatial frequencies are inherently unstable. Again, this is not a physical result but a mathematical consequence of the introduction of the simple linear gain model along with the α-parameter in a system with diffraction. As already implied, in a numerical integration of (5.1) and (5.2) with a relatively high resolution in x, i.e. a relatively small Δx, the Fourier window becomes large and Fourier components with a relatively high spatial frequency k_x grow unphysically. As a result Δx must be kept relatively large. A way to amend the high-k_x instability while retaining the phenomenological description has been suggested [41] [77]. The idea is to *ad hoc* introduce a small imaginary part in the factor $1/(2k_r)$ in (5.1), i.e. $1/(2k_r) \rightarrow (1 + j\epsilon)/(2k_r)$ with $\epsilon \geq 0$. The introduction of ϵ may be understood by transforming (5.1) into the k_x-domain:

$$\frac{j+\epsilon}{2k_r}k_x^2 E + \frac{1}{v_g}\frac{\partial}{\partial t}E - \frac{1+j\alpha}{2}\Gamma a(N-N_r)E + \left(\frac{\alpha_m}{2}\right)E = f(k_x,t) \quad (5.22)$$

It can seen that $\epsilon > 0$ introduces a loss that depends parabolically on k_x whereby the components of high spatial frequency are dampened. Of course the effect on the physically relevant k_x-values should be minimal when introducing ϵ. We have found that a value of $\epsilon = 7.5 \cdot 10^{-3}$ does not raise the background carrier-density level significantly. With this value of ϵ we can run calculations with $\Delta x = 1.33\,\mu$m for a BA laser of width $w = 200\,\mu$m while keeping the high k_x-components dampened for a pump rate $J = 1.2J_0$. The spatial resolution reported in the streak-camera experiment in [2] was 3 microns for a BA laser of a width of 100 microns (the time resolution was 50 ps). Thus the obtained numerical resolution is acceptable. On the other hand a higher resolution could be desirable for which a microscopic treatment of the semiconductor is necessary. In other words for a higher spatial resolution one could couple the macroscopic PDEs to the semiconductor Maxwell-Bloch

equations through the polarization variable.

At threshold the background carrier density is approximately $2.35N_0$ with the utilized parameters. The additional loss due to the introduction of the small number ϵ must not significantly raise this level. One should be concerned with the background carrier density or alternatively the average carrier density within $|x| \leq x_0$ or rather how much it differs from the carrier density outside the pumped region, as it is an important geometric factor having a significant influence on the shape of modes. This can be seen when finding stationary modes.

As an alternative to a microscopic treatment of the gain material one could consider adding more terms in the expansion of the lateral wave number in Eq. (3.35). If one included nonlinear gain in the phenomenological model, the problem of high-k_x instability would, however, not necessarily be eliminated, as it seems to appear even at low powers. The problems associated with a phenomenological treatment of BA lasers in the time-domain really underlines the complexity of the spatio-temporal behavior of BA lasers; wide-aperture multistripe index-guided laser arrays can be treated phenomenologically without similar problems. As examples 1-dimensional modeling of a laser array of width 100 μm (10 stripes) [90] and similar 2-dimensional modeling of an array of width 50 μm (5 stripes) [86] were performed for high pump currents using linear gain and the α-parameter.

5.6 Time-domain results

Our motivation for doing time-domain simulations is to try and capture the experimentally observed behavior of the AEC laser. First, however we regard the freely running (solitary) laser as a reference. Then we turn to the AEC laser. We are mainly concerned with the post-relaxation behavior of the laser since BA lasers are rarely used as switched devices. We change a few parameter values as compared with Chapter 3. They are listed in Table 5.1. The length of the chip is now 500 μm, which is half of the length used in chapter 3. Further, we change the rear facet reflectivity to $r_1 = 1$ so that we have the same distributed mirror loss as in chapter 3. Thus the rear facet is now assumed anti-reflection coated, while the front facet is still assumed cleaved.

Table 5.1: List of parameter values

Parameter	Symbol	Value	Unit
Cavity length	l	500	μm
Stripe width	w	200	μm
Active layer thickness	h	0.2	μm
Linewidth enhancement factor	α	3.0	
Linear gain coefficient	a	1×10^{-20}	m^2
Confinement factor	Γ	0.3	
Effective refractive index	n_r	3.5	
Effective group index	n_g	4.0	
Reference wavelenght	λ_r	810	nm
Transparency carrier density	N_0	1×10^{24}	m^{-3}
Internal loss	α_i	30	cm^{-1}
Carrier lifetime	τ_R	5	ns
Front facet reflectivity	r_2^2	0.35	
Rear facet reflectivity	r_1^2	1.0	
Diffusion coefficent	D	30	$\mathrm{cm}^2\mathrm{s}^{-1}$
External cavitity round-trip time	τ_{ext}	0.33	ns
Feedback parameter	γ	0.15	

5.6.1 Freely running laser

The dynamics of BA lasers has been studied extensively especially theoretically and perhaps to a lesser extend experimentally. Let us just let the phenomenological model demonstrate the characteristics of a solitary BA laser. It captures the filamentation process qualitatively well. Even with a microscopic treatment of the semiconductor gain material it is difficult to say how good the quantitative agreement with experiment is [2]. Figures 5.2 and 5.3 show the turn-on behavior and the post-relaxation behavior of the total output power and the laterally averaged carrier density as a function of time. The pump rate $J = 1.2J_0$ is applied at $t = 0$. Following the relaxation oscillations, which are quickly "smeared out" due to lateral dynamics, the output

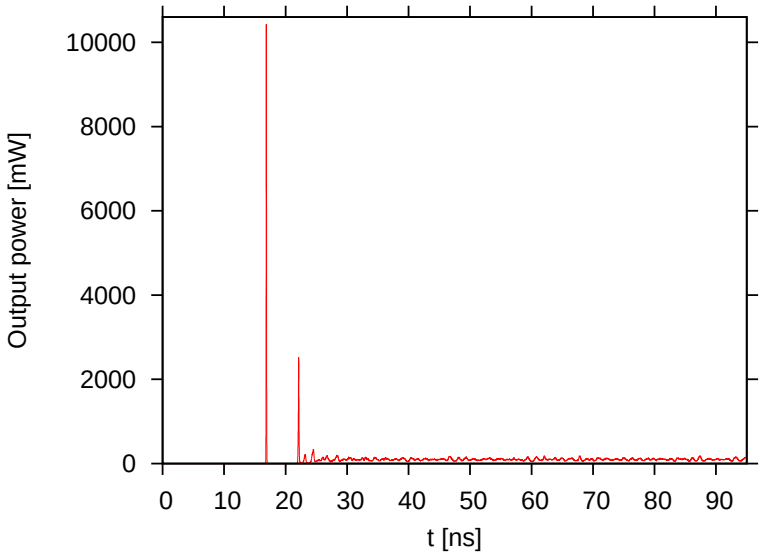

Figure 5.2: Output power as a function of time for freely running laser; $J = 1.2J_0$. After the few relaxation peaks the laser enters a fluctuating state and never finds a steady state.

power goes into a state where it fluctuates between 40 mW and 200 mW. The carrier density finds a background level $N_B(t) \simeq 2.4N_0$ around which it fluctuates but never finds a steady-state. One expects $N_B(t)$ to lie slightly above the steady-state threshold $2.35N_0$ due to spatial hole burning. This indicates that the introduction of the wavenumber-dependent loss through the small number ϵ, has not significantly changed the loss for the relevant k_x-range.

The time-averaged near-fields reported from various measurements can be described as a pedestal with a ripple on top. The time-averaged near-field in Figure 5.4 (a) shows those characteristics. For BA lasers of width, say, 200 μm or more, the reported far-fields are usually blurred shapes localized within an angular range depending on the width of the laser, the pump current, laser parameters, and design. Such a blurred shape is seen in Figure 5.4 (b) where the time-averaged far-field corresponds to the near-field in (a). Lastly, the corresponding time-averaged carrier density is seen in (c). Note the "ears" near the edges of the contact at $\pm x_0$. These are a consequense of the global guiding mechanism mentioned in Chapter 2; the real part of the

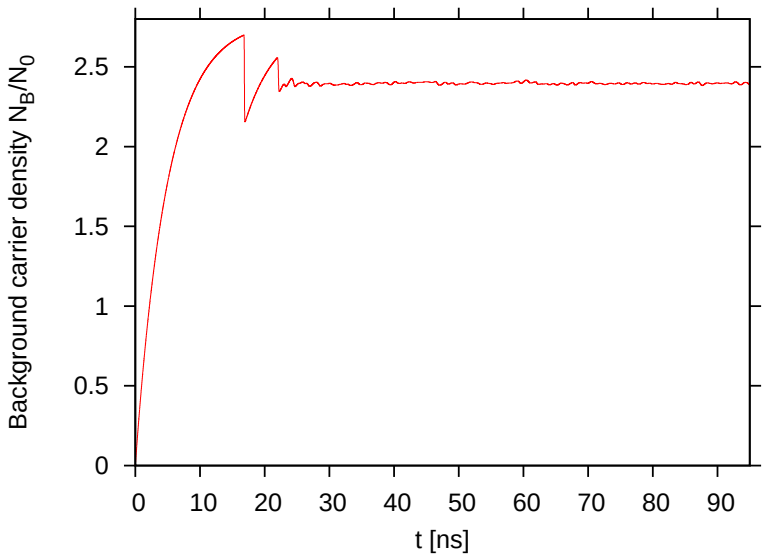

Figure 5.3: Background carrier density as a function of time for freely running laser. Same case as Figure 5.2.

refractive index is relatively high in the middle of the active region.

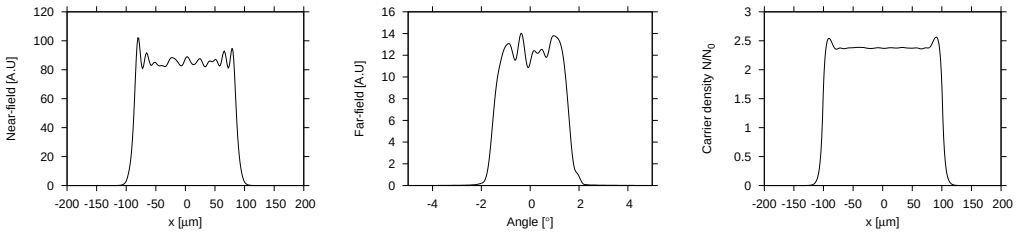

(a) (b) (c)

Figure 5.4: Lateral distributions of freely running laser for $J = 1.2J_0$. (a) Time-averaged near-field; (b) time-averaged far-field; (c) time-averaged carrier density. The averages were made over 60 ns.

Time-averaged fields only tell us a small part of how the laser operates. The complexity of the dynamics of a BA laser is demonstrated in Figures 5.5 and 5.6 where the near-field and far-field, respectively, are shown over a duration of 10 ns. The evolution of the near-field shows how filaments move laterally as a function of time and change direction randomly causing the characteristic zig-zag patterns. This behavior is also found with a microscopic description of the semiconductor. The far-field shows a highly irregular behavior very far from a steady pattern.

5.6.2 Asymmetric external cavity laser

The motivation for the AEC laser is an improved spatial coherence or alternatively a higher beam-quality as compared with the solitary BA laser. The single lobe of the output can, at least after additional spatial filtering has been performed, resemble a Gaussian beam. Our aim here is to reproduce, numerically, what we believe is the basic mode of operation for the AEC laser.

Spatial coherence has been shown to depend on the position of the stripe mirror in the far-field [34]. In other words there is a position of the stripe mirror that gives optimum spatial coherence for a given pump current. More specifically this optimum position gives the lowest full width at half maximum of the single lope and least possible intensity at other angles in the far-field. Experimentally it is seen that increasing the pump current invokes a need of adjusting the stripe-mirror in an outward direction to retain optimum spatial coherence [91]. However, again, this observation is based on time-

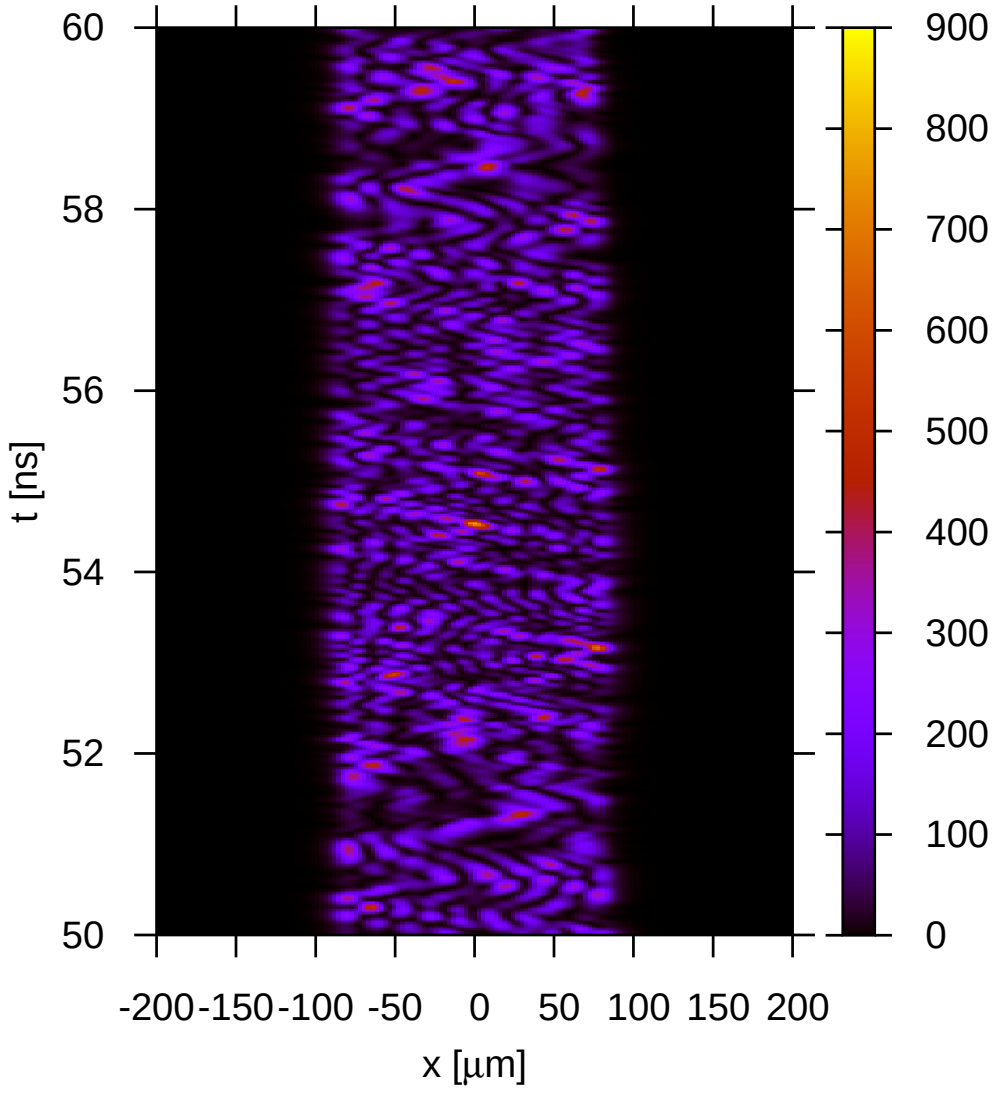

Figure 5.5: Near-field emission over 10 ns of freely running laser for $J = 1.2J_0$. Dynamic filamentantion causes zig-zag patterns.

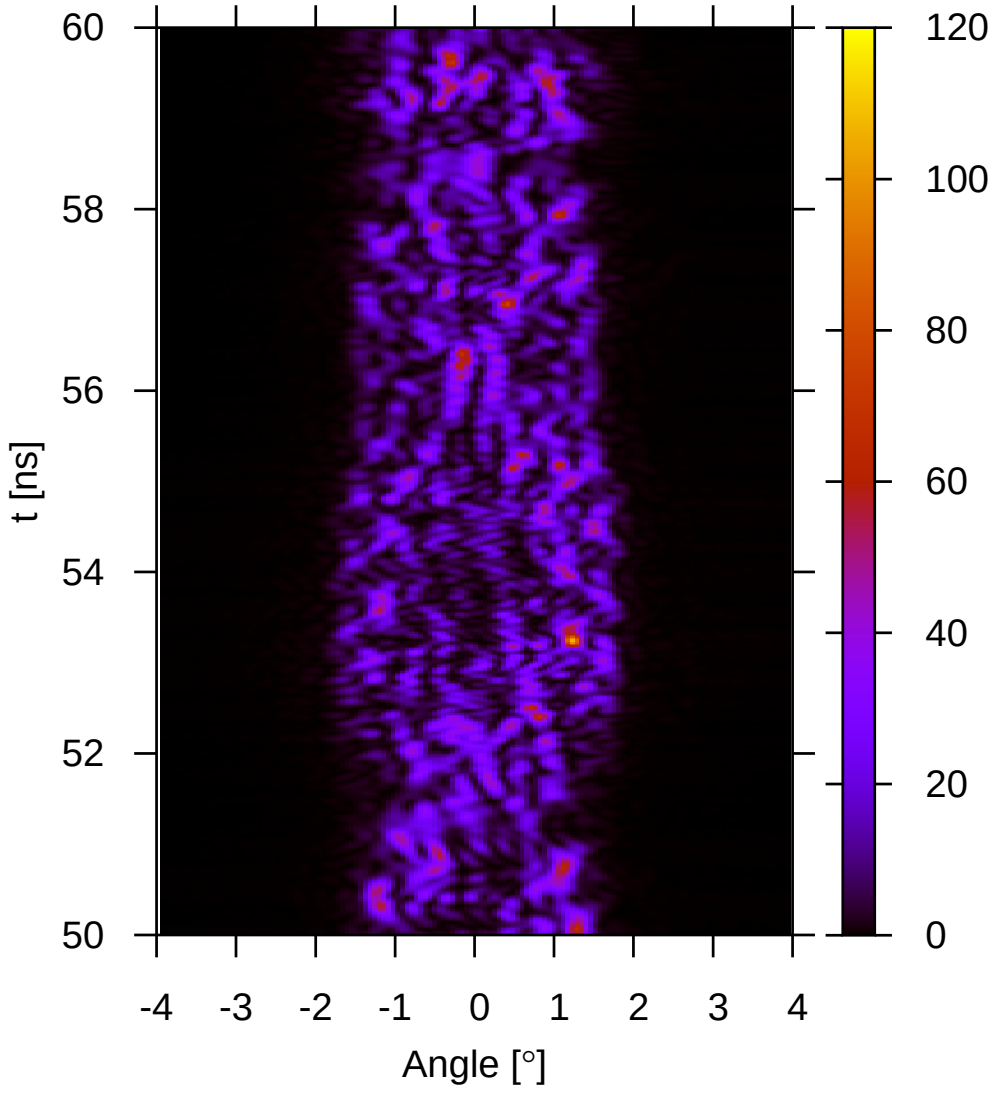

Figure 5.6: Far-field emission over 10 ns of freely running laser for same case as Figure 5.5.

averaged measurements and therefore it is difficult to tell what an increased current actually causes. Notably, we saw in Chapter 3 that for the stationary solutions m^{II}, the lobes in the far-field moved outwards (towards higher angles) as the current was increased.

We are not aware of the actual feedback levels due to the external mirror in AEC lasers; they can conceivably be obtained by measurements, however [24] [92]. For single-mode EC lasers, there exist different regimes of behavior in terms of stability and linewidth depending on, among other things, the feedback level; see e.g. [42]. No similar identification of regimes exists for AEC lasers.

Based on the perspective of this thesis, which is inclined towards spatial properties more than spectral properties, feedback levels of external cavity spatial filters can be divided into (at least) two regimes. We have seen in Chapter 3 that asymmetric field distributions exist in the regarded symmetric system. Since m^{II}-modes have single-lobed far-fields, they are interesting when regarding AEC lasers. If the asymmetric filtered feedback is relatively weak, one can expect that it "helps" the laser to operate in such an asymmetric state by introducing a small asymmetry and by lowering the mirror loss for the particular m^{II}. This regime is mainly likely at low pump currents. The second regime would be a regime where the reflectivity of the external stripe mirror is so large that the regarded physical system (the chip and external cavity) possesses a considerable asymmetry so that also linear solutions to the field equation could be highly asymmetric. This second regime would be relevant for high currents.

Measurements of output-intensity distributions of AEC lasers with mirror reflectors have to our knowledge all been time-averaged. Considering the dynamics of solitary BA lasers it is somewhat questionable that placing a stripe in the Fourier plane should completely stabilize the laser temporally. Spectral measurements have shown that the spectrum of an AEC laser with a mirror reflector has roughly the same width as the spectrum for the solitary laser [37]. With a grating reflector the reduction of the width of the spectrum is about an order of magnitude (in wavelength) [35]. The role of the finite length of the external cavity is not clear as no experiments have been reported where a systematic investigation of the dependence of the AEC laser on either the length of the external cavity or the feedback level have been performed.

While the role of the length of the external cavity is unclear, it has been established that in the Fourier-plane of the laser one angular position (or

rather two $\pm\theta$ due to symmetry) is optimum for a given pump current. Again, optimum means an angular position of the external reflector at which a single-lobe on the opposite side of the laser axis in the far field is enhanced as much as possible relative to the remaining parts the far-field. As it will be shown below, we do not find that this optimum position of the mirror translates into a field in a stationary state at a pump rate of $J = 1.2J_0$. We can, however, not rule out the existence of stable stationary solutions for an AEC laser. To be able to do so, one would have to include the full field equation with filtered delay in a stability analysis. However, this is probably mainly relevant at very low pump currents.

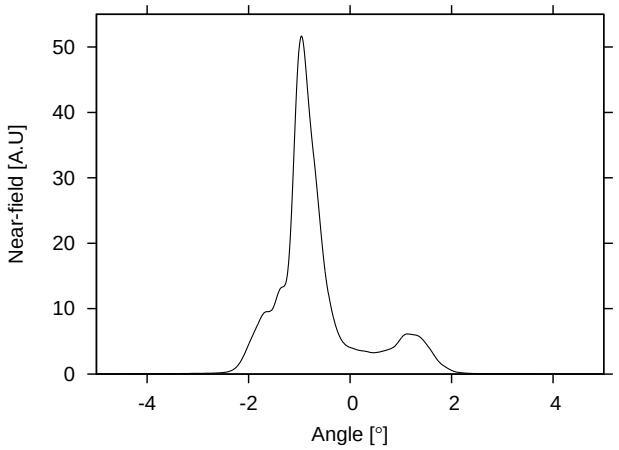

Figure 5.7: Far-field (time averaged) of asymmetric external cavity laser for $J = 1.2J_0$. The stripe-mirror has been centered at angle $\theta = 0.832°$. The single lobe peaks at $\theta = -0.96°$. The average was made over 60 ns.

Fig. 5.7 illustrates a time-averaged single-lobed far-field for a AEC laser where the angular position of the external mirror is close to optimum. The main peak of the far-field is located at $\theta = -0.96°$. The laser is again pumped at $J = 1.2J_0$ and the time average was performed over 60 ns from $t = 50$ ns to $t = 110$ ns. The external mirror is centered at $\theta = 0.832°$. The angular span of the mirror is $2\Delta\theta = .59°$, which is similar to the values in the original paper on AEC lasers [29]. The feedback parameter γ has the value 0.15 which is the value used in the original paper by Lang and Kobayashi [79]. With $r_2^2 = 0.35$ this value of γ corresponds to $r_3^2 = 1.86 \cdot 10^{-2}$. The length of the external cavity is 5 cm equivalent to $\tau_{ext} = 0.33$ ns. Recall that *measuring* a

far-field like the calculated one in Figure 5.7 requires that a beam-splitter is inserted in the cavity just just before the stripe mirror in the Fourier plane to get the entire far-field, i.e. both negative *and* positive angles. We find that the far-field in Figure 5.7 is in a good qualitative agreement with the example of a measured far-field in Figure 2.4. We will discuss the agreement further after looking at the near-field and carrier density.

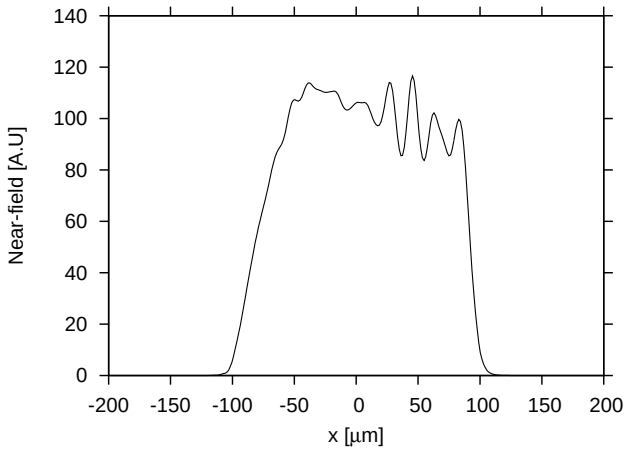

Figure 5.8: Near-field (time-averaged) of asymmetric external cavity laser. Same case as in Figure 5.7. Note how the field tilts to theright, while the single-lobe in the far-field is located at an negative angle.

The time-averaged near-field can be seen in Figure 5.8. It has 8-10 peaks. Note how the near-field tilts to the right, i.e. the left edge of the field is higher than the right edge of the field. It thus tilts to the opposite side of the single lobe in the far-field. The orientation of the tilt is in agreement with the experiment of [33] shown in Figures 2.3 and 2.4, where the same orientation of the near-field compared to the far-field was seen.

Due to the intensity distribution in the time-averaged near-field, the time-averaged carrier-density distribution in Figure 5.9 forms a "cradle" in the carrier density on the left side implying a nonlinear waveguide since the refractive index is relatively high where the carrier density is relatively low. We note that the tilt in the near-field is opposite to the one we found for the modes m^{II} in Chapter 3. The near-field of m^{II} with its single lobe at, say, a negative angle, has a positive "global" slope, see e.g. 8^{II} in Figures 3.17 (f) and 3.18 (f). However, in the present time-domain calculation we are at a considerably higher current, and we have to remember that m^{II} were found

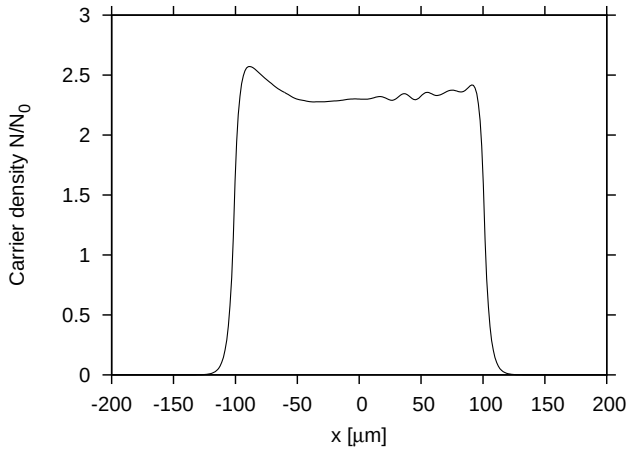

Figure 5.9: Carrier-density distribution (time-averaged) of asymmetric external cavity laser. Same case as in Figure 5.8.

to be globally unstable.

For an AEC laser it was shown experimentally in [73] that for pump currents close to threshold it was possible to pick out lateral modes (due to the external stripe-mirror) that resemble m^{II}-modes, i.e. the single lobe in the far-field and the edge of the near-field with highest intensity were oriented oppositely. When they increased the current, however, the situation changed to the one we find in this chapter and that was found in [33]: the single-lobe in the far-field and the edge with highest intensity in the near-field have same orientation.

In [34] the peak angle of the single lobe was 2.1 degrees for a 200 micron wide laser lasing at 810 nm and driven at 2 times threshold. In experiments, the angle at which the single lobe is centered moves outwards as the current is increased [91]. Our calculation at 1.2 times threshold gives a smaller value than 2.1 degrees as expected. In any case we would not expect to be able to theoretically obtain exact agreement with an experiment without knowing relevant parameter values of that very experiment.

In experiments it is seen that the output-beam quality of the AEC laser benefits greatly from using an anti-reflection (AR) coated output facet. Power reflectivities as low as 10^{-5} are obtainable [73]. We cannot readily include such low reflectivities in the Lang-Kobayashi-type field equation. When comparing the time-averred far-field in Fig. 5.7 with an experimental one we notice that the pedestal on the left side of the single lope is higher than

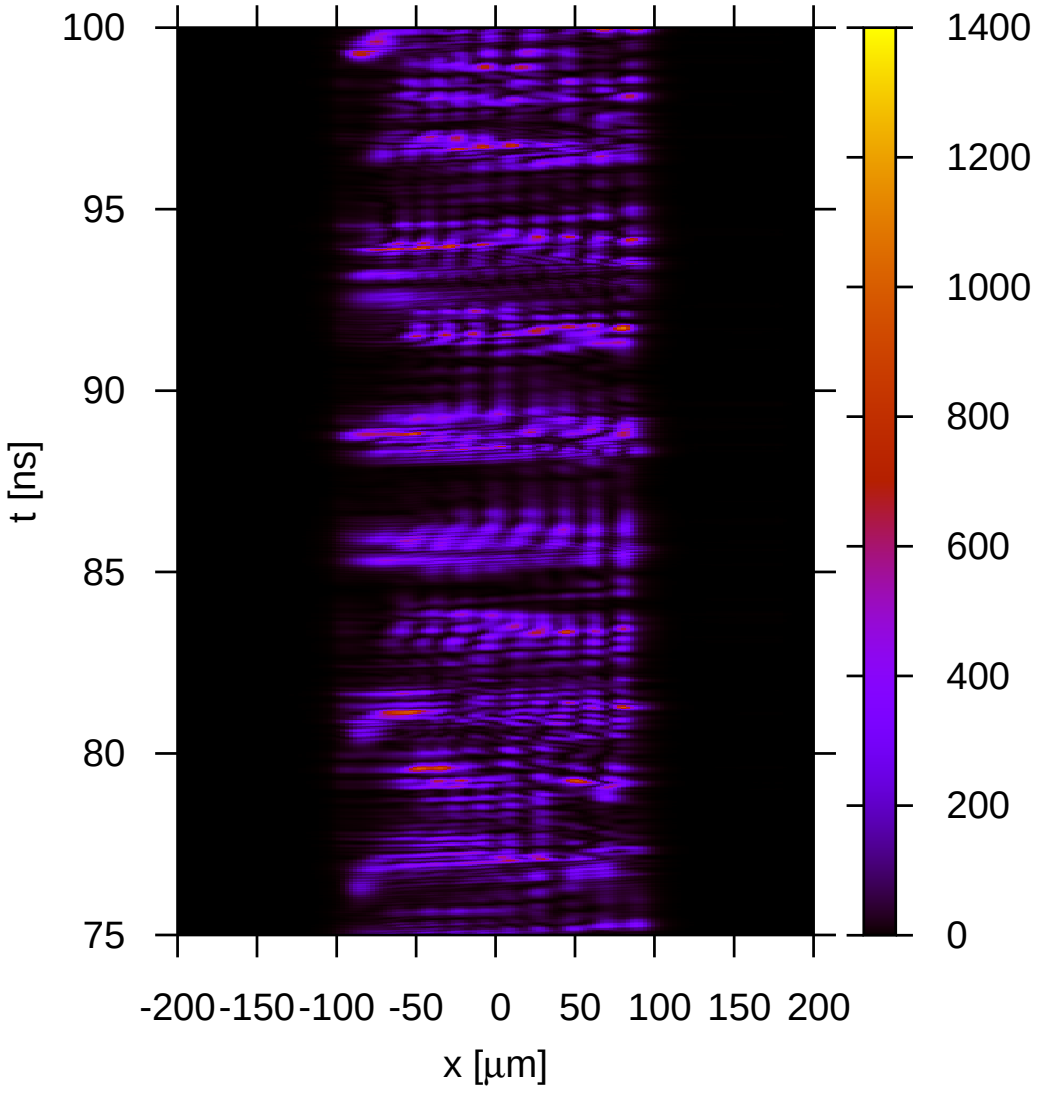

Figure 5.10: Near-field emission over 25 ns of asymmetric external cavity laser for $J = 1.2J_0$. The zig-zagging of filaments has been inhibited due to the external mirror.

what is usually seen experimentally. We partly owe this to the lack of AR coating in the simulation. Moreover, we could probably perform additional optimization in our calculations by adjusting the width Δk_x of the external mirror. We have not optimized this parameter. Nevertheless, we are rather confident that the mode of operation, which we have found numerically, is the one seen experimentally. Particularly because there exists only one optimum angular position, which is rather tricky to find, where the AEC laser behaves optimally single-lobed. We find this to be the case numerically as it is found experimentally [91].

We now turn to the dynamics underlying the time-averaged behavior. Figure 5.10 shows a 25 ns interval of the near-field. We see how the lateral movement of filaments has been almost stopped. Instead the filaments now more tend to stick to each their "lane". This behavior resembles the dynamics of a lasr array. We also see that the nice coherent parts of the time series are actually located on the right side despite the fact that in the time-averaged near-field we saw that the intensity was globally higher on the left side. However violent bursts of intensity to the left of the middle causes the tilt in the time-averaged near-field. Therefore a relation to the m^{II}-modes is perhaps conceivable. However, the spatio-temporal evolution is still irregular..

For applications the far-field is the most relevant and naturally the temporal irregularities of the near-field translate to the far-field in Figure 5.11. The main intensity peaks are around -1° as expected from the time-averaged far-field. The time variation is still complex in spite of filtering provided by the external stripe-mirror.

There is thus no indication that the stripe-mirror in the external cavity can force the behavior on the chip into a steady state in spite of the improved spatial coherence. Nor is there a clear sign of a characteristic time period of the system to which τ_{ext} can be tuned to match. When looking closely at the intensity at $x = 0$ one can see fluctuatuins close to τ_{ext}, but the time variation is not periodic. Recently, (periodic) picosecond-pulse generation in a BA laser was demonstrated experimentally with an AEC-like laser which had a grating as the reflector in the external cavity [93]. The BA laser in the experiment was AR-coated. It is presumable that a grating reflector is attractive to force the laser into a state that is periodic in time.

We briefly return to the discussion of the sign in the convolution in conjunction with a stripe-mirror filter. By omiting the minus sign, we find that it

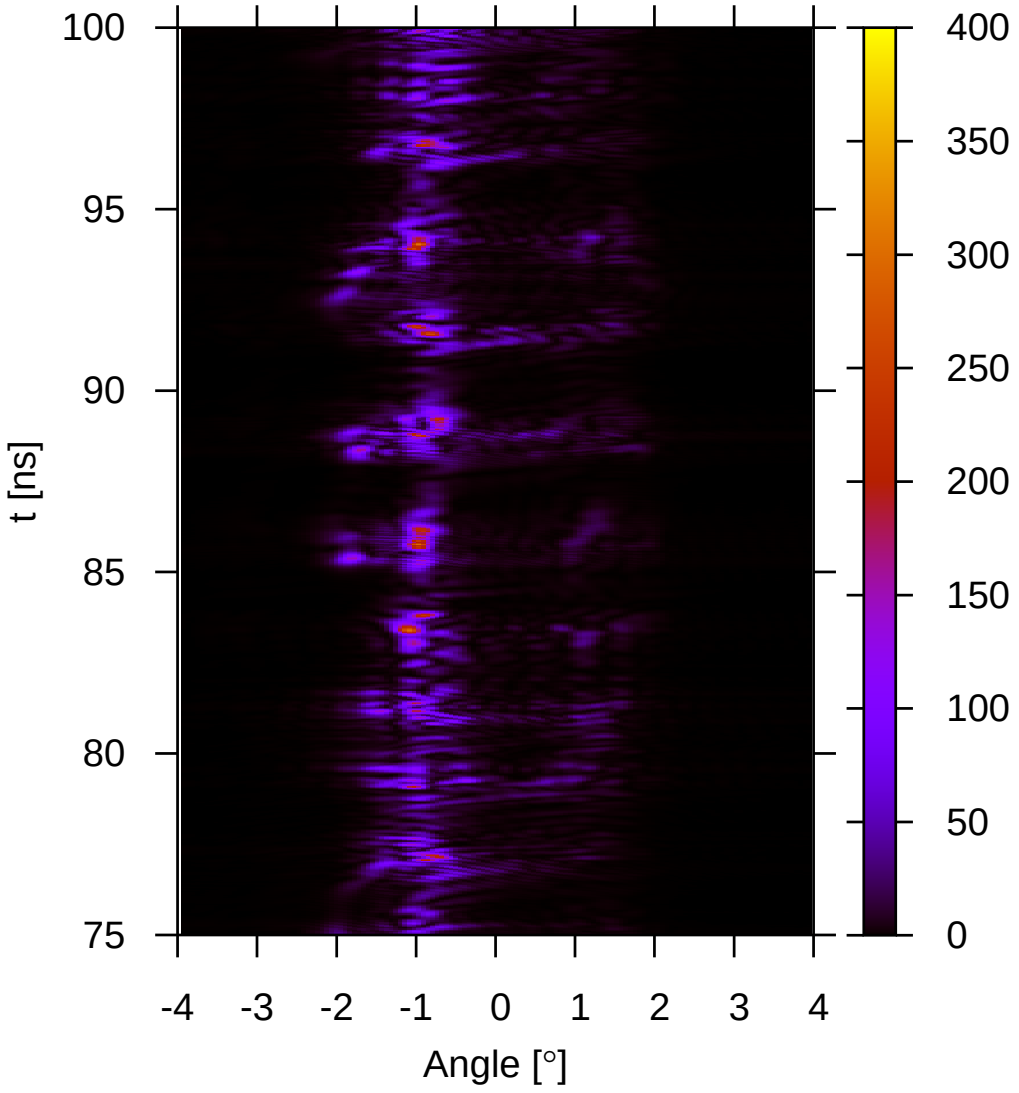

Figure 5.11: Far-field emission over 25 ns of asymmetric external cavity laser. Same case as in Figure 5.10. Main intensity peaks appear around $\theta = -1°$ corresponding to the time-average.

is easily possible to obtain perfect (time-averaged) single-lobe far-field. The far-field is thus localized tightly around a specific angle. The time variation can be made perfectly periodic with τ_{ext} as one of the characteristic periods. Also, in terms of phase-plane plots, one can obtain beautiful toruses like it is possible in single-lateral-mode EC lasers [80]. In essence the AEC laser behaves much more like a single-lateral-mode external cavity laser in this case. The reason is that the single-lobe in the far-field, in this case, is localized at the same angle as the stripe mirror thus making the feedback much more effective than in the case where the mirror is located at approximately the angle opposite the optical axis. The field is then fed back to the position of the near-field from which it was emitted, making way for a very efficient feedback laser. One can realize a feedback setup resulting in the described mode of operation by inserting an additional lens in the external cavity [94]. Related to this discussion is the case of a phase-conjugate feedback. In this case the field fed back to the laser is (for a unfiltered feedback) [30]

$$E_{PC}(x,t) \propto E^*(x, t - \tau_{ext}). \tag{5.23}$$

There is no minus in front of the x; instead the field is the complex conjugate of the emitted field. This is readily extended to the filtered case. An experimental example of phase-conjugate feedback may be found in [95].

5.7 Summary

For the AEC laser we extended the z-averaged field equation to include an external cavity with a spatially filtered feedback and obtained good qualitative agreement with time-averaged measurements; a single-lobed time-averaged far-field was calculated for an appropriate position of the stripe mirror. The effect of the external mirror on the time-varying near-field was seen to be a prevention of the lateral movement of filaments which is common for a freely running BA laser. The field was, however, still varying in time. The improved order in the near-field led to a far-field where most of the intensity was fluctuating around an angle off the laser axis, approximately opposite to stripe mirror.

The phenomenological description of the gain material using linear gain and the α-parameter has to *ad hoc* be supplemented with an wavenumber-dependent loss. This method was found in the literature on time-dependent

modeling of BA lasers, and it is necessary in order to avoid unphysical amplification of field components with high spatial frequency. The phenomenological model was seen to be able to capture the dynamic filamentation of the solitary BA laser giving zig-zag patterns.

Chapter 6

Modal expansion of lateral modes

In chapter 3 we found a wide variety of stationary states. The modes m^I were definite-parity modes. They have conventional threshold pump rates at which the field is zero in the absence of noise. For currents modestly above the threshold, the field of the regarded mode becomes finite and the nonlinear light-semiconductor interaction causes the field to change shape. Take Figure 3.3 where the near-field of 6^I just above threshold (a) changes by an increased dip in the middle of the near-field when increasing the current (b). Similar behavior is seen for the near-field of 5^I in Figure 3.4 (a) and (b). This behavior can be understood by regarding the nonlinear mode m^I as a linear gain guided mode perturbed by the nonlinearity of the gain material as we shall show in the following. We do this by introducing a mode-expansion technique to calculate nonlinear lateral field distributions. The lateral field is expanded in linear gain guided modes. As opposed to Chapter 3 we include carrier diffusion and regard its effect on the field at low currents. To make our results easy to interpret we neglect the spreading of current.

6.1 Expansions of the lateral field and the carrier density

We denote the nonlinear stationary states calculated in this chapter E_m, where m is the mode number. Let $E_m(x)$ and $\Phi_m(x)$ be related by a scaling factor ξ_m, that is, $E_m = \xi_m \Phi_m$, and let Φ_m be normalized such

that $\int_{-\infty}^{\infty} \Phi_m^2 dx = 1$. The lateral modes Φ_m are expanded in a complete biorthonormal set, i.e.

$$\Phi_m = \sum_{q=1}^{\infty} b_m^q \psi_q, \tag{6.1}$$

where the modes ψ_q are eigenfunctions of the operator H_0:

$$H_0 \psi_q = \beta_{0,q}^2 \psi_q, \tag{6.2}$$

and H_0 is defined as

$$H_0 = \frac{d^2}{dx^2} + k_{tr}^2(x), \tag{6.3}$$

and $\beta_{0,q}^2$ are the eigenvalues corresponding to ψ_q. The wavenumber k_{tr} is defined through

$$k_{tr}^2(x) = \begin{cases} k_r^2 & \text{for } |x| < x_0 \\ k_r^2 - 2k_r \frac{\partial k}{\partial N} N_r & \text{for } |x| > x_0. \end{cases} \tag{6.4}$$

Recall that $N_r = N_0 + \alpha_i/(\Gamma a)$. The wavenumber k_{tr} is to describe the BA laser at transparency provided that no spreading of current takes place. The mode Φ_m is to be understood through its near-field $|\Phi_m|^2$ having m dominant peaks implying $b_m^m > b_m^{q \neq m}$. Now, the full field problem is written as

$$(H_0 + H')\Phi_m = \beta_m^2 \Phi_m, \tag{6.5}$$

where the operator H' is introduced as a perturbation that will modify the unperturbed modes ψ_q and their corresponding eigenvalues $\beta_{0,q}^2$. H' is defined as

$$H' = \begin{cases} 2k_r \left[\frac{1}{v_g}(\omega_s - \omega_r) + \frac{\partial k}{\partial N}(N - N_r) \right] & \text{for } |x| < x_0 \\ 2k_r \frac{1}{v_g}(\omega_s - \omega_r) & \text{for } |x| > x_0. \end{cases} \tag{6.6}$$

Inserting the expansion of Eq. (6.1) in (6.5), multiplying by ψ_k on both sides, and then integrating gives us

$$\sum_q [H'_{kq} + \delta_{kq}(\beta_{0,q}^2 - \beta_m^2)] b_m^q = 0. \tag{6.7}$$

In Eq. (6.7) δ is Kronecker's delta and

$$H'_{kq} = \int_{-\infty}^{\infty} \psi_k H' \psi_q dx. \tag{6.8}$$

Further, we have used that $\int_{-\infty}^{\infty} \psi_k \psi_q dx = \delta_{kq}$. Also, as in Eq. (3.31) $\beta_m = k_r + \frac{\alpha_m}{2}$. This constant value of β_m for all m may be inserted in Eq. (6.7). For clarity we rename it $\gamma_1 = k_r + \frac{\alpha_m}{2}$ and Eq. (6.7) becomes

$$\sum_q [H'_{kq} + \delta_{kq}(\beta_{0,\,q}^2 - \gamma_1^2)] b_m^q \equiv \sum_q A_{kq} b_m^q = 0. \tag{6.9}$$

We express the carrier density N as a Fourier series on $|x| \leq x_0$, i.e.

$$N = \overline{N} + \sum_{u=1}^{\infty} \left(\Delta N_u e^{jK_u x} + \text{c.c.} \right). \tag{6.10}$$

Further, we impose periodic boundary conditions:

$$K_u x_0 = u\pi. \tag{6.11}$$

Inserting (6.10) in Eq. (3.43) and then averaging from $-x_0$ to x_0 yields

$$-\overline{N} + J\tau_R = \frac{1}{P_{sat}} \left[(\overline{N} - N_0)|E_{0,\,m}|^2 + \frac{1}{2x_0} \int_{-x_0}^{x_0} |E_m(x)|^2 \sum_u (\Delta N_u e^{jK_u x} + \text{c.c.}) dx \right], \tag{6.12}$$

while projecting onto $\exp(\mp jK_i x)$ gives

$$\eta_i \Delta N_i = \frac{1}{P_{sat}} \left[(\overline{N} - N_0) v(K_i) + \sum_{u \neq i} \Delta N_u v(K_i - K_u) + \sum_u \Delta N_u^* v(K_i + K_u) \right], \tag{6.13}$$

and

$$\eta_i \Delta N_i = \frac{1}{P_{sat}} \left[(\overline{N} - N_0) v(-K_i) + \sum_{u \neq i} \Delta N_u v(-K_i - K_u) + \sum_u \Delta N_u^* v(-K_i + K_u) \right]. \tag{6.14}$$

We have used

$$|E_{0,\,m}|^2 = \frac{1}{2x_0} \int_{-x_0}^{x_0} |E_m|^2 dx, \tag{6.15}$$

$$\eta_i = -DK_i^2 \tau_R - 1 - \frac{|E_{0,\,m}|^2}{P_{sat}}, \tag{6.16}$$

and

$$v(K_i) = \frac{1}{2x_0} \int_{-x_0}^{x_0} |E_m(x)|^2 \exp(-jK_i x) dx. \tag{6.17}$$

Eq. (6.12) scales the intensity $|E_m(x)|^2$ for given J, $\overline{N}$, and coefficients ΔN_u, giving the proper ξ_m^2. The properly scaled field can then be used in the linear system of Eq. (6.13) and (6.14) to solve for ΔN_u.

To summarize this section: Eq. (6.9) and Eqs. (6.12) together with (6.13) and (6.14) constitute the nonlinear system of equations that together with the modes ψ_q describe a BA laser where lateral spreading of carriers is neglected. They must be solved iteratively.

6.2 Linear gain guided modes

We must find solutions to the unperturbed eigenvalue problem (6.2) to obtain the modes for the expansion in Eq. (6.1). The lateral current profile is approximated to be constant within $x < |x_0|$ and not to spread into $x > |x_0|$while demanding $\psi_q(x)$ and $\partial_x\psi_q(x)$ to be continuous at $\pm x_0$. Choosing such simple boundary conditions will make our results easier to interpret, which will be evident in our discussion.The profile in Eq. (6.4) describes a gain guided lateral structure. Assuming solutions of region 1 ($|x| \leq x_0$) and region 2 ($|x| > x_0$) of the form $C_i e^{jk_i x} + D_i e^{-jk_i x}$ with $i = 1, 2$ and substituting into Eq. (6.2), one may obtain

$$k_{1,\mathrm{q}}^2 + \beta_{0,q}^2 = k_r^2 \tag{6.18}$$

$$k_{2,\mathrm{q}}^2 + \beta_{0,q}^2 = k_r^2 - 2k_r \frac{\partial k}{\partial N} N_r = k_r^2 + k_r \Delta\alpha(\alpha - j) \tag{6.19}$$

and in addition the relation

$$k_{2,\mathrm{q}}^2 - k_{1,\mathrm{q}}^2 = k_r \Delta\alpha(\alpha - j), \tag{6.20}$$

where $\Delta\alpha = \Gamma a N_r = \alpha_i + \Gamma a N_0$ is the difference between the losses in the unpumped region 2 and the pumped region region 1. Since the unperturbed system is linear and has inversion symmetry the solutions must have definite parity. The symmetric solutions are (integer q odd)

$$\psi_q(x) = \begin{cases} B_q \exp(-jk_{2,q}x) & \text{for } x < -x_0 \\ A_q \cos(k_{1,q}x) & \text{for } |x| < x_0 \\ B_q \exp(jk_{2,q}x) & \text{for } x > x_0. \end{cases} \tag{6.21}$$

The asymmetric solutions are (integer q even)

$$\psi_q(x) = \begin{cases} -B_q \exp(-jk_{2,q}x) & \text{for } x < -x_0 \\ A_q \sin(k_{1,q}x) & \text{for } |x| < x_0 \\ B_q \exp(jk_{2,q}x) & \text{for } x > x_0. \end{cases} \tag{6.22}$$

The boundary conditions at $x = \pm x_0$ imply the transcendental equations

$$-k_{1,\mathrm{q}} \tan(k_{1,q} x_0) = j k_{2,q} \text{ , } q \text{ odd,} \tag{6.23}$$

and

$$k_{1,\mathrm{q}} \cot(k_{1,\mathrm{q}} x_0) = j k_{2,q} \text{ , } q \text{ even.} \tag{6.24}$$

Eqs. (6.23) and (6.24) together with Eq. (6.20) must be solved numerically for a given set of parameters. In general $k_{1,q}$, $k_{2,q}$ are complex. The spatial Fourier frequency K_i associated with the carrier density has a magnitude that is very close to $2\mathrm{Re}(k_{1,i})$. The imaginary part of $k_{1,q}$ implies a slow lateral variation in $\psi_q(x)$ on $|x| < x_0$ in addition to the fast variation caused by the spatial frequency $\mathrm{Re}(k_{1,q})$. In particular a dip may be seen around $x = 0$ in $|\psi_q(x)|^2$ for $q \geq 3$. This dip is also found using BPM [31]. Finally, with Eq. (6.18) we find the unperturbed complex propagation constants $\beta_{0,\mathrm{q}}$.

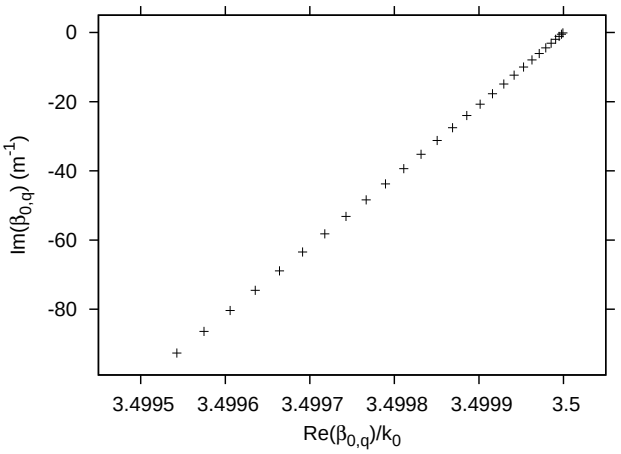

Figure 6.1: Calculated real- and imaginary parts of the unperturbed propagation constants $\beta_{0,q}$ for $q = 1$ through $q = 28$. The lowest order, $q = 1$, corresponds to the point with the smallest negative imaginary part in the upper right corner. Higher orders have successively higher loss.

For q going from 1 to 28 we show the real and imaginary parts of $\beta_{0,\mathrm{q}}$ in Fig. 6.1. $\beta_{0,1}$ is located in the upper right corner and the sequence ends $\beta_{0,28}$ in the lower left corner. The sequence illustrates how mode 1 has the lowest loss and that the loss increases monotonously with increasing mode number as we also saw in Chapter 3. The increasing loss is due to growing energy flow in outward directions for increasingly high mode order.

6.3 Results of mode expansion

The numerical procedure of obtaining stationary solutions is described in Appendix F. It returns the expansion coefficients. The expansion representation of the field allows one to interpret nonlinear perturbations. That is, which coefficients $b_m^{q\neq m}$ are significant.

6.3.1 Comparison of modal expansion with scattering-potential method

In order to compare the modal-expansion method of this chapter with the method of finding m^I-modes in Chapter 3 we first set the diffusion coefficient equal to zero in the former method and also set the current spreading distance d of the latter method equal to zero. Of course, we expect the two methods to agree well; at least for pump rates where Φ_m can be regarded as a perturbed ψ_m. Near-fields for mode 7 for $J = 1.015J_0$ obtained by the two different methods are shown together in Fig. 6.2. The two methods show good agreement.

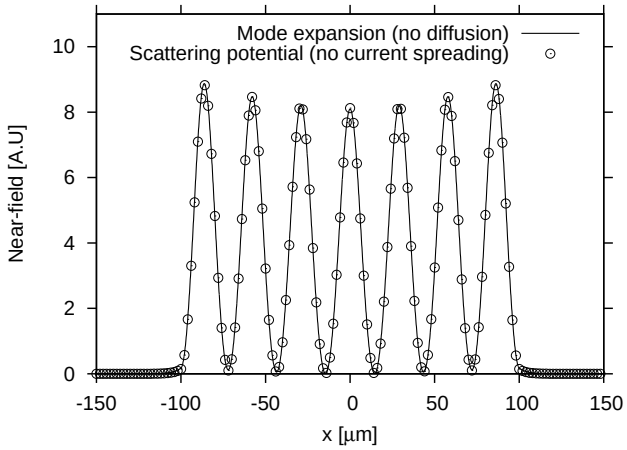

Figure 6.2: Near-field of mode 7 obtained by method of present chapter (Modal expansion) with $D = 0$ and by the method of Chapter 3 (Scattering potential) with $d = 0$. The pump rate is $J = 1.015J_0$. The two methods agree well.

6.3.2 Perturbation interpretation of low-current nonlinear modes

To be able to understand the effects of spatial hole burning in more detail, we consider the case of infinite absorption outside the pumped region, i.e. for $\Delta\alpha$ going to infinity, as a reference. For this special case, the unperturbed modes and their eigenvalues may be found analytically [56]. For $|x| < x_0$ the unperturbed modes ψ_q are given as

$$\psi_q^{\inf}(x) = \begin{cases} \frac{1}{\sqrt{x_0}} cos(k_{1,q}^{\inf} x) & \text{for odd } q \\ \frac{1}{\sqrt{x_0}} sin(k_{1,q}^{\inf} x) & \text{for even } q. \end{cases} \tag{6.25}$$

where

$$2x_0 k_{1,q}^{\inf} = q\pi, \tag{6.26}$$

and q is a positive integer. For $|x| > x_0$, $\psi_q^{\inf} = 0$ for all q. The modes in (6.25) are thus truncated sinusoidals. The corresponding eigenvalues are given as

$$(\beta_{0,q}^2)_{\inf} \simeq k_r^2 - \frac{q^2\pi^2}{4x_0^2}. \tag{6.27}$$

For a given q, $k_q^{\inf}$ is real and has half the magnitude of the spatial frequency associated with ΔN_q, that is K_q. Then $k_{1,q}^{\inf}$ lies very close to $\mathrm{Re}(k_{1,q})$, which is much greater than $\mathrm{Im}(k_{1,q})$, and similarly $(\beta_{0,q}^2)_{\inf}$ lies close to $\mathrm{Re}(\beta_{0,\mathrm{q}}^2)$, which is much greater than $\mathrm{Im}(\beta_{0,q}^2)$. Thus $k_{1,q}^{\inf}$ and $(\beta_{0,q}^2)_{\inf}$ serve as useful references for interpretation in the following.

So far, we have regarded the field Φ_m as an expansion with one dominating unperturbed mode ψ_m. This allows us, within restrictions, to use perturbation theory, using $\psi_q^{\inf}$, to interpret the solutions, which we have obtained by solving the complete nonlinear system of equations.

We wish to identify the role of individual Fourier components ΔN_u. For this purpose we define $M(m,u,q)$:

$$\Delta N_u M(m,u,q) = \int_{-x_0}^{x_0} \psi_m^{\inf}(\Delta N_u \exp(jK_u x) + \text{c.c.})\psi_q^{\inf} dx, \tag{6.28}$$

with the matrix elements

$$M(m,u,q) = \delta_{(m-q-2u),0} + (-1)^{m+1} + \delta_{(m-q+2u),0}. \tag{6.29}$$

Note that with inversion symmetry, we have taken ΔN_u to be real.

To understand the results of the nonlinear calculations, we turn to perturbation theory. We settle for first order, which gives expansion coefficients

$$b_m^m = 1 \tag{6.30}$$

and for $q \neq m$

$$b_m^q = \frac{H'_{qm}}{\beta_{0,\,m}^2 - \beta_{0,\,q}^2} \tag{6.31}$$

Again, the approximation of infinite $\Delta\alpha$ offers us insight. Using $(\psi_q)_{\text{inf}}$ and $(\beta_{0,\,q})_{\text{inf}}$ in Eq. (6.31) gives for $q \neq m$

$$(b_m^q)_{\text{inf}} = 2k_r \frac{\partial k}{\partial N} \left(\frac{4x_0^2}{\pi^2} \right) \frac{\sum_{u=1}^{\infty} \Delta N_u M(m,u,q)}{q^2 - m^2} \tag{6.32}$$

For a mode Φ_m, we find from actual computations of E_m that the most important Fourier components of the carrier density distribution at low currents are in general ΔN_m and ΔN_1. ΔN_m is caused by ψ_m as the main spatial frequency of $|\psi_m|^2$ lies close to $K_m = 2k_m^{\text{inf}}$. In conjunction with ΔN_m, we further identify the matrix element $M(m,m,3m)$, which enters Eq. (6.32). We note that this element involves ψ_{3m}, which one could call the first higher Bragg order of the grating component ΔN_m. In fact, in our calculations, we find this Bragg component of the field to be non-zero, i.e. $b_m^{3m} \neq 0$. Slow variations in the near-field cause ΔN_1 to be significant. Via the matrix elements $M(m,1,m\pm 2)$, ΔN_1 will enter Eq. (6.32) causing $\beta_m^{m\pm 2}\psi_{m\pm 2}$ to be significant in the expansion of Φ_m. Hence, we have used the approximation of infinite $\Delta\alpha$ to identify the most important matrix elements for the 2 regarded Fourier coefficients of the carrier density that are typically the most significant.

As stated in the beginning of this chapter Figures 3.3 and 3.4 show how the dip in the middle of the near-field increases as the current is increased just above threshold. Beating between $b_m^m\psi_m$, and $b_m^{m\pm 2}\psi_{m\pm 2}$ yields an increased slow variation of approximate spatial frequency K_1. As the current is increased and the intensity increases, $|\Delta N_1|$ is going to increase causing $|b_m^{m\pm 2}|$ to rise yielding a larger dip and in turn a larger $|\Delta N_1|$ and so on. For higher currents more coefficients become significant.

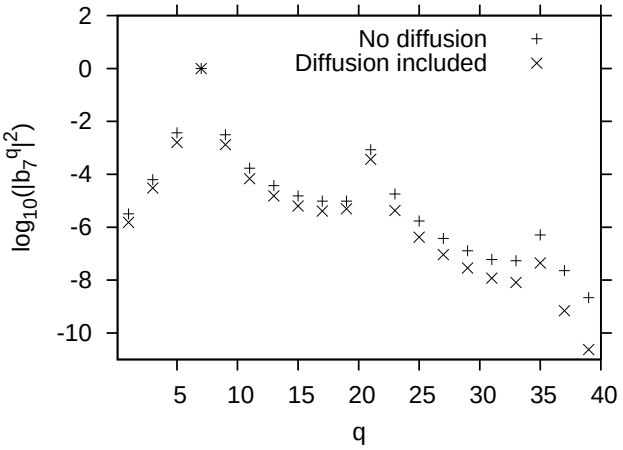

Figure 6.3: The absolute squares of the expansion coefficients b_7^q are plotted as a function of q. Both the case with diffusion and the case with no diffusion included in the calculation are shown. Pump rate is $J = 1.015J_0$. The effect of diffusion is to diminish the coefficients $b_m^{q\neq m}$.

6.3.3 Identification of most important expansion terms and the influence of carrier diffusion

We perform a low-current investigation of modes 1 and 7. First mode 7. The absolute squares of the expansion coefficients of mode $m = 7$ at $J = 1.015J_0$ are given as an example in Fig. 6.3. Both the cases without diffusion ($D = 0$) and with diffusion ($D = 30$ cm/s^2). Other parameters are as in Chapter 3. Clearly, the coefficient b_7^7 is close to unity at this current. As predicted by the infinite loss approximation and perturbation theory, the largest coefficients $b_7^{q\neq 7}$ are b_7^5 and b_7^9 joined by the $q = 3m$-coefficient b_7^{21}. Also the higher-order Bragg order at $q = 5m = 35$ is visible. It is rather striking to see the traces of a nonlinear Bragg grating, albeit a theoretical one. The effect of carrier diffusion is to diminish the expansion coefficients $b_7^{q\neq 7}$ slightly. The corresponding near-fields can be seen in Figure 6.4. Two things can be seen from the comparison. The near-field with diffusion has a smaller dip around $x = 0$ because of the inhibited $b_7^{7\pm 2}$; and the total power of the near-field obtined with diffusion is higher. This is due to a reduction in spatial hole burning, caused by the diffusion. It can be shown that a reduced $|\Delta N_m|$ for mode Φ_m reduces the nonlinear loss. We lastly investigate the influence of carrier diffusion on E_1 at a low pump rate. As one could expect it is small.

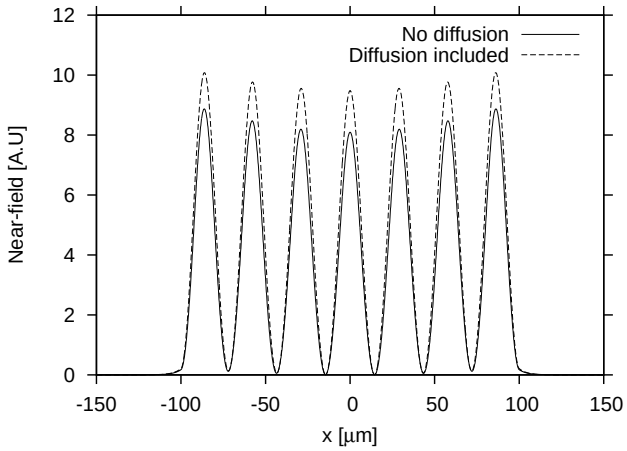

Figure 6.4: Near-field of mode E_7 for cases of no diffusion respectively included diffusion when calculating the field at $J = 1.015J_0$. The dip around $x = 0$ is smaller when diffusion is included. The total output power is higher when computed including the diffusion due the diffusion-induced suppression of spatial hole burning.

The comparison of coefficients b_1^q in Figure 6.5 tell that carrier diffusion is of minor importance for the fundamental mode. The corresponding comparison between near-fields is displayed in Figure 6.6 and the near-fields for cases with and without diffusion are very similar.

6.4 Summary

We have compared calculations of modes 1 and 7 including and excluding, respectively, carrier diffusion. We used a mode expanion technique. Clearly, mode 7 was more affected by diffusion. Nevertheless, the qualitative features, namely the dip in the middle and the identification of the largest coefficients $b_m^{q\neq m}$ for $m = 7$ as $b_m^{m\pm 2}$ and b_m^{3m}, also held true when the diffusion was included. Based on this we believe that there is good reason to believe that the stability properties found in Chapter 4 of modes m^I with $m \geq 3$, which were calculated in Chapter 3, are likely to hold true also when diffusion is included. This seems very certain for the fundamental mode $m = 1$ as it is only affected to a very small degree by carrier diffusion at low pump rates.

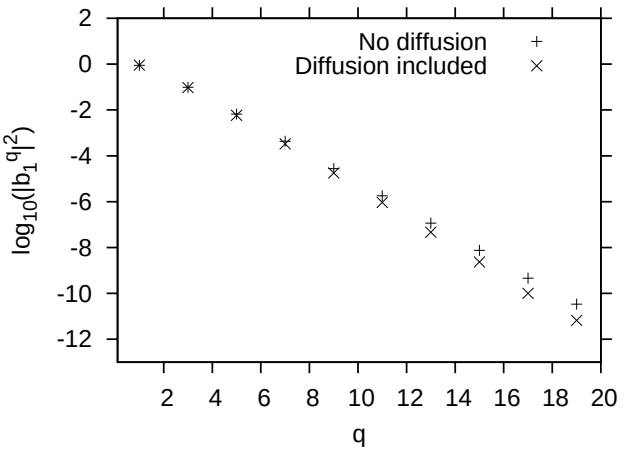

Figure 6.5: The absolute squares of the expansion coefficients b_1^q plotted as a function of q. Both the case with diffusion and the case with no diffusion included in the calculation are shown. Pump rate is $J = 1.003J_0$. The effect of diffusion is seen to be small for the most significant coefficients $b_1^{q\neq 1}$.

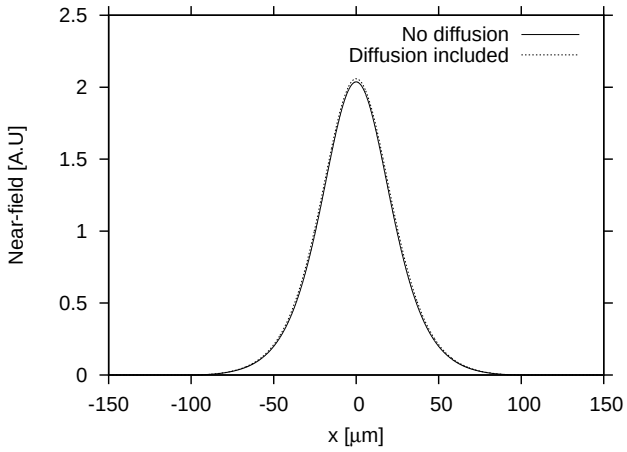

Figure 6.6: Near-fields of mode E_1 for $J = 1.003J_0$ calculated without diffusion and with diffusion respectively. The difference is small.

Chapter 7

Summary

In this thesis we presented and discussed calculations regarding lateral modes of broad area lasers. We explored the actual mode structure, calculating individual stationary solutions. We then performed a small-signal analysis with the emphasis on the stability properties of the lateral modes. The mode of operation of an existing asymmetric external-cavity set-up was studied in the studied in the time-domain. Lastly stationary solutions were studied close to their their threshold using a modal-expansion technique suited for interpretation via perturbation theory. Throughout the thesis we used equations obtained through a mean field approximation implying averaging over the longitudinal direction of the laser.

A BA laser pumped at a considerable current is in a fluctuating state. Most measured intensity distributions presented in the literature are due to time-averaged measurements. When calculating lateral, stationary modes in a BA laser it is therefore a misconception to expect that calculated stationary solutions should reproduce such time-averaged measurements. However, from a theoretical point of view it is of interest to know about the stationary mode structure, both from the point of view of fundamental laser theory and perhaps also for designing devices. The lateral mode structure turned out to be much richer than merely the "ordinary" lateral modes normally associated with BA lasers. Several different types of modes constituted a structure where different mode-types were found to be interrelated. Most notably is the existence of asymmetric modes, which exist in spite of the symmetric lateral structure. One category of asymmetric modes has a single-lobed far field that resembles the far-field of the asymmetric external cavity laser that we

studied in Chapter 5. We saw another category of asymmetric modes whose near-field compressed itself towards the lateral edge of the active region in the manner of an accordion as the pump rate was increased. In total we presented four different categories of modes whose tuning curves were seen to be part of a systematic structure of merging curves.

Due to the spatial dependence of the lateral modes, we employed a Green's function method to study the small signal properties of some of the calculated stationary solutions. By means of this method one can determine the linear stability of calculated stationary solutions. We demonstrated methods to determine both stability and bifurcations of the saddle-point type and of the Hopf-type respectively. For the saddle-node stability we stated the function σ which in order to be in accordance with bifurcation theory must change sign whenever a new branch emerges on the tuning curve along which one is running. We saw that σ fulfilled this requirement. In addition its sign determined the local stability of a given stationary state

The stability analysis gave some general results. Firstly, for a BA laser of width 200 μm, we find no stable modes except at very low currents (currents below 1.002 times the threshold current of the laser). This theoretical result is fundamental because it tells why a BA laser driven at considerable currents operate in a fluctuating state: all modes are unstable. We have not tested the stability of all types of modes found in Chapter 4. Nevertheless, experiments and time-domain simulations tell us that hypothetical stable stationary solutions never yield a steady-state; the trajectory in some face space will newer settle to the point of the hypothetical stable mode. Specifically for the fundamental lateral mode, we found that when increasing the pump rate from threshold it becomes unstable (it Hopf-bifurcates) around 1.001 times the threshold current. The first higher order mode Hopf-bifurcates around 1.0016 times the threshold current. These values are of course dependent on the utilized parameters. All standard gain guided modes of higher order, i.e. order 3 or greater, become unstable immediately above threshold or are alternatively "born" unstable. The asymmetric modes conceivably related to the AEC laser are locally stable but are globally unstable, i.e. they suffer from a Hopf-instability.

We demonstrated the calculation of linewidth for the fundamental mode and found a value of 8.0 GHz at a current just under the one at which the mode Hopf-bifurcates. We mentioned that the Green's function method can also be used to calculate noise spectra for stable stationary solutions. We

leave the calculation of noise spectra for future work. Further, it was shown how the change of the oscillation frequency due to a static change in current can be predicted correctly by the small-signal analysis. This shows the general strength of the Green's function approach. The small-signal analysis can also be generalized to devices with a built-in lateral index variation. This could be useful in the hunt for a stable lateral mode in wide aperture lasers.

For direct comparisons between experiments and theory on BA lasers not running at the very low currents mentioned above, one probably has to turn to time-domain simulations. We solved our phenomenological mean field equations in the time-domain using the hopscotch method. We extended the field equation to include a term describing a spatially filtered feedback in order to describe the regarded asymmetric external cavity laser. The model was capable of giving a qualitative agreement with experiment: when the stripe mirror of the external cavity was placed, say, to the right of the laser axis, a dominant lobe appeared to the left of the laser axis when performing a time average. This, however, occurs after one has carefully placed the stripe mirror at a specific optimum position. Such an optimization of the position of the stripe mirror is also necessary in an experiment. At this optimum configuration of the asymmetric external cavity, the laser is still in a time-dependent state. However, in the near-field the lateral movement of filaments has been inhibited and the dynamics of the near-field resemble those of a laser array more than those of a solitary broad area laser. In agreement with existing literature we found that the phenomenological description of the gain material urges that one *ad hoc* includes a wavenumber-dependent loss to avoid amplification of field components of high spatial frequency. We saw that phenomenological model could capture the lateral dynamics of the solitary broad area laser yielding zig-zag patterns of filaments in the near-field.

Summing up in broad terms, an analysis of the stationary lateral mode structure of a BA laser showed a rich and systematically structured variety of modes. All modes subject to a small-signal stability analysis proved to be unstable except at very low pump rates where the two lowest order modes might be stable. The instability of all (viewed) modes at considerable pump rates is the small-signal answer to the question why the output of broad area lasers is in general fluctuating. In the time-domain we showed these fluctuations and showed that an asymmetric external cavity could dampen

the fluctuations but could not bring the laser into a stationary state.

Appendix A

Energy density and power

For a static field the energy density is given by

$$W = 2\epsilon_0 n_r n_g \left(|E^+|^2 e^{\alpha_m z} + |E^-|^2 e^{-\alpha_m z}\right) |\phi(y)|^2 . \tag{A.1}$$

If we assume that E^+ and E^- are independent of z, the longitudinal average is

$$\begin{aligned} \overline{W}(x,y) &= 2\epsilon_0 n_r n_g |\phi(y)|^2 |E^-(x)|^2 \frac{1}{l} \int_0^l \left(r_1^2 e^{\alpha_m z} + e^{-\alpha_m z}\right) dz \\ &= 2\epsilon_0 n_r n_g |\phi(y)|^2 K |E_s(x)|^2 \end{aligned} \tag{A.2}$$

where

$$K = \frac{(r_1 + r_2)(r_1 r_2 - 1)}{2 r_1 r_2 ln(r_1 r_2)} . \tag{A.3}$$

We have here used that for z-independent E^+ and E^-, the boundary condition $E^+ = r_1 E^-$ and the definition

$$E_s(x) = \frac{1}{\sqrt{2r_1}} (\overline{E^+}(x) + r_1 \overline{E^-}(x)) \tag{A.4}$$

give the relations

$$E_s(x) = \sqrt{2r_1} E^- = \sqrt{\frac{2}{r_1}} E^+ . \tag{A.5}$$

The average energy in the active region ($y = 0$) is then

$$\overline{W}(x,0) = 2\epsilon_0 n_r n_g |\phi(0)|^2 K |E_s(x)|^2 . \tag{A.6}$$

The transverse confinement factor Γ is given by

$$\Gamma = \frac{\int_{active\ layer} |\phi(y)|^2 dy}{\int_{-\infty}^{\infty} |\phi(y)|^2 dy} \simeq |\phi(0)|^2 h \tag{A.7}$$

where h is the active layer thickness, and where we have used that the distribution $\phi(y)$ is normalized such that $\int_{-\infty}^{\infty} |\phi(y)|^2 dy = 1$. We can therefore replace $|\phi(0)|^2$ in (A.6) by Γ/h_a.

The output power per unit length at the right facet (i.e. the right facet near field power) is

$$\begin{aligned} P_2(x) &= 2\epsilon_0 n_r c |E^+|^2 e^{\alpha_m l}(1 - r_2^2) \\ &= 2\epsilon_0 n_r c |E_s|^2 \frac{1}{2r_2}(1 - r_2^2)\,. \end{aligned} \tag{A.8}$$

The left facet near field power is similarly

$$\begin{aligned} P_1(x) &= 2\epsilon_0 n_r c |E^-|^2 (1 - r_1^2) \\ &= 2\epsilon_0 n_r c |E_s|^2 \frac{1}{2r_1}(1 - r_1^2)\,. \end{aligned} \tag{A.9}$$

The total output power per unit length is then

$$P_{tot}(x) = P_1(x) + P_2(x) = 2\epsilon_0 n_r c \alpha_m l K |E_s(x)|^2\,. \tag{A.10}$$

This is consistent with the fact that the total photon energy per unit lateral length decays with the rate $v_g \alpha_m$, i.e.

$$P_{tot}(x) = v_g \alpha_m l \int_{-\infty}^{\infty} \overline{W}(x, y) dy = 2\epsilon_0 n_r c \alpha_m l K |E_s(x)|^2 \tag{A.11}$$

and then the total output power is given as

$$P_{out} = \int_{-\infty}^{\infty} P_{tot}(x) dx. \tag{A.12}$$

Appendix B

Boundary conditions

In obtaining Eq. (4.31) we neglected $d\boldsymbol{\psi}/dx$ at the interval boundaries

$$\frac{\partial}{\partial x}E(-A) = j\sqrt{\kappa}E(-A). \tag{B.1}$$

In this appendix we omit the "WKB"-subscript on κ. Taking the differential on both sides implies

$$\frac{\partial}{\partial x}\delta E(-A) = j\frac{\partial\sqrt{\kappa}}{\partial\omega}\delta\omega E(-A) + j\frac{\partial\sqrt{\kappa}}{\partial J}\delta J E(-A) + j\sqrt{\kappa}\delta E(-A) \tag{B.2}$$

or in the time domain where $j\delta\omega$ is replaced by d/dt

$$\frac{\partial}{\partial x}\delta E = \frac{\partial\sqrt{\kappa}}{\partial\omega}\frac{d}{dt}E + j\frac{\partial\sqrt{\kappa}}{\partial J}\delta J E + j\sqrt{\kappa}\delta E \tag{B.3}$$

We want the boundary conditions for $\delta b = \delta E/E$. The first derivative of δb is

$$\frac{d}{dx}\delta b = -\frac{\delta E}{E}\frac{1}{E}\frac{d}{dx}E + \frac{1}{E}\frac{d}{dx}\delta E \tag{B.4}$$

Using (B.1) and (B.3) in (B.4) results in

$$\frac{d}{dx}\delta b = \frac{\partial\sqrt{\kappa}}{\partial\omega}\frac{d}{dt}b + j\frac{\partial\sqrt{\kappa}}{\partial J}\delta J, \tag{B.5}$$

where $db/dt = (1/E)dE/dt$ has been used. Hence,

$$\frac{d}{dx}\boldsymbol{\psi} = \frac{d}{dt}\begin{pmatrix} \mathrm{Re}(\frac{\partial\sqrt{\kappa}}{\partial\omega}b) \\ \mathrm{Im}(\frac{\partial\sqrt{\kappa}}{\partial\omega}b) \end{pmatrix} + \begin{pmatrix} -\mathrm{Im}(\frac{\partial\sqrt{\kappa}}{\partial J}) \\ \mathrm{Re}(\frac{\partial\sqrt{\kappa}}{\partial J}) \end{pmatrix}\delta J \tag{B.6}$$

and

$$\frac{d}{dx}\boldsymbol{\psi} = s\begin{pmatrix} \mathrm{Re}(\frac{\partial\sqrt{\kappa}}{\partial\omega}b) \\ \mathrm{Im}(\frac{\partial\sqrt{\kappa}}{\partial\omega}b) \end{pmatrix} + \begin{pmatrix} -\mathrm{Im}(\frac{\partial\sqrt{\kappa}}{\partial J}) \\ \mathrm{Re}(\frac{\partial\sqrt{\kappa}}{\partial J}) \end{pmatrix}\delta J. \tag{B.7}$$

Similarly for the right hand side $x = A$

$$\frac{d}{dx}\delta b = -\frac{\partial\sqrt{\kappa}}{\partial\omega}\frac{d}{dt}b - j\frac{\partial\sqrt{\kappa}}{\partial J}\delta J, \tag{B.8}$$

$$\frac{d}{dx}\boldsymbol{\psi} = -s\begin{pmatrix} \mathrm{Re}(\frac{\partial\sqrt{\kappa}}{\partial\omega}b) \\ \mathrm{Im}(\frac{\partial\sqrt{\kappa}}{\partial\omega}b) \end{pmatrix} + \begin{pmatrix} \mathrm{Im}(\frac{\partial\sqrt{\kappa}}{\partial J}) \\ -\mathrm{Re}(\frac{\partial\sqrt{\kappa}}{\partial J}) \end{pmatrix}\delta J. \tag{B.9}$$

We see from (B.7) and (B.9) that the local stability is not affected by the boundary conditions for a constant current ($\delta J = 0$) since the local stability is associated with the system determinant $D(s)$ at $s = 0$.

For the static frequency tuning, the terms including s equal zero. The equation for static frequency tuning including the effect of boundary conditions is given as (cf. Eq. (4.93))

$$\delta\omega = \delta\omega_B + k_r\frac{\partial g}{\partial N}\int_{-A}^{A}\lim_{s\to 0} s\boldsymbol{\zeta}_2^{\dagger}(x,s)\begin{pmatrix} \alpha \\ -1 \end{pmatrix}\frac{\tau_R\delta J}{1+|E(x)|^2/P_{sat}}dx, \tag{B.10}$$

where

$$\delta\omega_B = -\lim_{s\to 0} s\boldsymbol{\zeta}_2^{\dagger}(x,s)\frac{d}{dx}\widetilde{\boldsymbol{\psi}}\Big|_{-A}^{A}. \tag{B.11}$$

After some derivations one obtains,

$$\delta\omega_B = -\sigma^{-1}\left\{(\boldsymbol{y}_4)_1(A)\left[\left(\frac{d}{dx}\widetilde{\boldsymbol{\psi}}(x)\right)_1(\boldsymbol{y}_3)_3(x) + \left(\frac{d}{dx}\widetilde{\boldsymbol{\psi}}(x)\right)_2(\boldsymbol{y}_3)_4(x)\right] + (\boldsymbol{y}_3)_1(A)\left[\left(\frac{d}{dx}\widetilde{\boldsymbol{\psi}}(x)\right)_1(\boldsymbol{y}_4)_3(x) + \left(\frac{d}{dx}\widetilde{\boldsymbol{\psi}}(x)\right)_2(\boldsymbol{y}_4)_4(x)\right]\right\}\Big|_{-A}^{A}. \tag{B.12}$$

Inserting from (B.7) and (B.9) gives

$$\delta\omega_B = -\sigma^{-1}\left(\mathrm{Im}\left(\frac{\partial\sqrt{\kappa}}{\partial J}\right)\{(\boldsymbol{y}_4)_1(A)\left[(\boldsymbol{y}_3)_3(A)+1\right] - (\boldsymbol{y}_3)_1(A)(\boldsymbol{y}_4)_3(A)\} - \mathrm{Re}\left(\frac{\partial\sqrt{\kappa}}{\partial J}\right)\{(\boldsymbol{y}_4)_1(A)(\boldsymbol{y}_3)_4(A) - (\boldsymbol{y}_3)_1(A)\left[(\boldsymbol{y}_4)_4(A)+1\right]\}\right)\delta J. \tag{B.13}$$

The derivative

$$\frac{\partial\sqrt{\kappa}}{\partial J} = k_r\tau_R\frac{\partial k}{\partial N}\frac{1}{\sqrt{\kappa}} \tag{B.14}$$

is much smaller (10^{-26}) than the various the various other entries. The boundary conditions are therefore neglible on frequency tuning. This has been confiremed numerically.

Appendix C

The stability parameter σ

Here we derive the asymptotic behavior of $D(s)$ when $s \to \infty$ along the real axis. For large positive s we can approximate the matrix $\boldsymbol{M}_u^\dagger$ defined in (4.37) by

$$\boldsymbol{M}_u^\dagger = \left(\begin{array}{c|c} \mathbf{0} & \boldsymbol{I} \\ \hline -s\boldsymbol{M}_\omega & \mathbf{0} \end{array}\right) \tag{C.1}$$

The eigenvalues of this matrix are solutions to the characteristic equation

$$\det(\boldsymbol{M}_u^\dagger - \lambda) = 0, \tag{C.2}$$

which becomes

$$\lambda^4 + s'^2 = 0 \tag{C.3}$$

where s' is the scaled parameter

$$s' = 2\frac{k_r}{v_g}s. \tag{C.4}$$

The eigenvalues of $\boldsymbol{M}_u^\dagger$ are then the four complex numbers $\lambda_1 = e^{j\frac{\pi}{4}}\sqrt{s'}$, $\lambda_2 = -e^{j\frac{\pi}{4}}\sqrt{s'}$, $\lambda_3 = e^{-j\frac{\pi}{4}}\sqrt{s'}$, and $\lambda_4 = -e^{-j\frac{\pi}{4}}\sqrt{s'}$. The eigenvector $\boldsymbol{w}_i$ corresponding to the eigenvector λ_i is

$$\boldsymbol{w}_i^T = (s'\lambda_i, -\lambda_i^3, s'\lambda_i^2, (s')^2). \tag{C.5}$$

From Eqs. (4.64)

$$\frac{d}{dx}\boldsymbol{Y}^\dagger(x,s)\boldsymbol{w}_i = \lambda_i \boldsymbol{Y}^\dagger \boldsymbol{w}_i. \tag{C.6}$$

The solutions to (C.6) leads to

$$\boldsymbol{Y}^{\dagger}(A,s)\boldsymbol{w}_i = e^{\lambda_i 2A)}\boldsymbol{w}_i \tag{C.7}$$

We expand $\boldsymbol{e}_1$ and $\boldsymbol{e}_2$

$$\boldsymbol{e}_1 = \sum_{i=1}^{4} b_{1i}\boldsymbol{w}_i \tag{C.8}$$

and

$$\boldsymbol{e}_2 = \sum_{i=1}^{4} b_{2i}\boldsymbol{w}_i, \tag{C.9}$$

which alternatively can be expressed

$$\boldsymbol{V}\boldsymbol{b}_1 = \boldsymbol{e}_2 \tag{C.10}$$

and

$$\boldsymbol{V}\boldsymbol{b}_2 = \boldsymbol{e}_4 \tag{C.11}$$

where $(\boldsymbol{b}_1)_i = b_{1i}$ and $(\boldsymbol{b}_2)_i = b_{1i}$ for $i = 1, .., 4$. The matrix $\boldsymbol{V}$ is defined as

$$\boldsymbol{V} = \begin{pmatrix} (s')^2 & (s')^2 & (s')^2 & (s')^2 \\ s'\lambda_1 & s'\lambda_2 & s'\lambda_3 & s'\lambda_4 \\ s'\lambda_1^2 & s'\lambda_2^2 & s'\lambda_3^2 & s'\lambda_4^2 \\ -\lambda_1^3 & -\lambda_2^3 & -\lambda_3^3 & -\lambda_4^3 \end{pmatrix}. \tag{C.12}$$

The determinant of $\boldsymbol{V}$ is related to the Vandermonde determinant. It is given by

$$\det\boldsymbol{V} = -(s')^4 \prod_{i>j}(\lambda_i - \lambda_j). \tag{C.13}$$

and inserting the eigenvalues λ_i

$$\det\boldsymbol{V} = 16(s')^7. \tag{C.14}$$

From Eqs. (4.56), (4.57), (C.8), and (C.9) we get

$$\boldsymbol{q}_3(s) = \boldsymbol{Y}^{\dagger}(A,s)\boldsymbol{e}_1 = \sum b_{1i}e^{\lambda_i 2A}\boldsymbol{w}_i \tag{C.15}$$

$$\boldsymbol{q}_4(s) = \boldsymbol{Y}^{\dagger}(A,s)\boldsymbol{e}_2 = \sum b_{2i}e^{\lambda_i 2A}\boldsymbol{w}_i. \tag{C.16}$$

Using the expression for the system determinant $D(s)$ in Eq. (4.61) then yields

$$D(s) = \sum_{i,j} b_{1i} b_{2j} e^{(\lambda_i+\lambda_j)2A}((\boldsymbol{w}_i)_3(\boldsymbol{w}_j)_4 - (\boldsymbol{w}_i)_4(\boldsymbol{w}_j)_3) \tag{C.17}$$

or inserting $\boldsymbol{w}_i$

$$D(s) = (s')^3 \sum_{i,j} b_{1i} b_{2j} e^{(\lambda_i+\lambda_j)2A}(\lambda_i^2 - \lambda_j^2). \tag{C.18}$$

By introducing the matrix $\boldsymbol{B}$ with matrix elements

$$(\boldsymbol{B})_{ij} = (\lambda_i^2 - \lambda_j^2)e^{(\lambda_i+\lambda_j)2A} \tag{C.19}$$

the system determinant can be written

$$D(s) = (s')^3 \boldsymbol{b}_1^T \boldsymbol{B} \boldsymbol{b}_2. \tag{C.20}$$

The squares of the eigenvalues λ_i are

$$\lambda_1^2 = \lambda_2^2 = js' \tag{C.21}$$

$$\lambda_3^2 = \lambda_4^2 = -js'. \tag{C.22}$$

Then $\boldsymbol{B}$ may be written as

$$\boldsymbol{B} = \left(\begin{array}{c|c} \mathbf{0} & \boldsymbol{B}_s \\ \hline -\boldsymbol{B}_s^T & \mathbf{0} \end{array}\right), \tag{C.23}$$

where $\boldsymbol{B}_s$ is the 2×2 submatrix

$$\boldsymbol{B}_s = 2js' \begin{pmatrix} e^{2\sqrt{2s'}A} & e^{j2\sqrt{2s'}A} \\ e^{-j2\sqrt{2s'}A} & e^{-2\sqrt{2s'}A} \end{pmatrix}. \tag{C.24}$$

The dominant factor is $e^{2\sqrt{2s'}A}$ so for large s the system determinant becomes

$$D(s) = 2j(s')^4(b_{11}b_{23} - b_{13}b_{21})e^{2\sqrt{2s'}A}[1 + \mathscr{O}(e^{-2\sqrt{2s'}A})]. \tag{C.25}$$

Solving Eq. (C.10) and (C.11) gives $\boldsymbol{b}_1$ and $\boldsymbol{b}_2$ from which the relevant components are

$$b_{11} = \frac{-4(s')^5\lambda_4}{\det \boldsymbol{V}} \tag{C.26}$$

$$b_{13} = \frac{4(s')^5\lambda_1}{\det \boldsymbol{V}} \tag{C.27}$$

$$b_{21} = \frac{-4j(s')^5\lambda_4}{\det \boldsymbol{V}} \tag{C.28}$$

$$b_{23} = \frac{-4j(s')^5\lambda_1}{\det \boldsymbol{V}}. \tag{C.29}$$

These finally give the asymptotic form of $D(s)$ for large s:

$$D(s) = \frac{1}{4}s' e^{2\sqrt{2s'}A}[1 + \mathscr{O}(e^{-2\sqrt{2s'}A})]. \tag{C.30}$$

Appendix D

The Diffusion matrix $\boldsymbol{D}(x,s)$

The diffusion matrix $\boldsymbol{D}(x,\omega)$ defined by (4.82) originates from the Langevin driving term $F(\boldsymbol{r},s)$ in (3.7), which describes the spontaneous emission noise. We will in this appendix derive an expression for $\boldsymbol{D}(x,s)$ based on the correlation relations for $F(\boldsymbol{r},\omega)$, where $\boldsymbol{r}=(x,y,z)$.

It has been shown by Henry [49] that $F(\boldsymbol{r},\omega)$ obeys the correlation relations

$$\begin{aligned}\langle F(\boldsymbol{r},\omega)F(\boldsymbol{r}',\omega')\rangle &= \langle F^*(\boldsymbol{r},\omega)F^*(\boldsymbol{r}',\omega')\rangle = 0\\ \langle F(\boldsymbol{r},\omega)F^*(\boldsymbol{r}',\omega')\rangle &= D_F(\boldsymbol{r},\omega)\delta(\boldsymbol{r}-\boldsymbol{r}')2\pi\delta(\omega-\omega')\end{aligned} \tag{D.1}$$

where

$$D_F(\boldsymbol{r},\omega)=\frac{2\omega^3\hbar}{c^3\epsilon_0}n_r g_m n_{sp}\,. \tag{D.2}$$

Here n_r is the refractive index, g_m the material gain, and n_{sp} the spontaneous emission factor. They all depend on space and frequency.

From the definitions (3.14) and (3.23) of $f_\omega^\pm(x,z)$ and $f_\omega(x)$ it follows by (D.1) that

$$\begin{aligned}\langle f_\omega(x)f_{\omega'}(x')\rangle &= \langle f_\omega^*(x)f_{\omega'}^*(x')\rangle = 0\\ \langle f_\omega(x)f_{\omega'}^*(x')\rangle &= D_f(x,\omega)\delta(x-x')2\pi\delta(\omega-\omega')\end{aligned} \tag{D.3}$$

where

$$D_f(x,\omega)=\frac{1}{2r_1l^2}\int_{-\infty}^{\infty}\int_0^l\left\{D_F(\boldsymbol{r},\omega)|\phi(y)|^2(r_1^2e^{\alpha_m z}+e^{-\alpha_m z})\right\}dydz\,. \tag{D.4}$$

We will approximate $D_f(x,\omega)$ by

$$D_f(x,\omega) \simeq \frac{2\omega^3\hbar}{c^3\epsilon_0 l} K n_r g n_{sp}, \tag{D.5}$$

and $g = \int_{-\infty}^{\infty} g_m |\phi(y)|^2 dy$ is the modal gain. All parameters n_r, g and n_{sp} are averaged over z. K is the Peterman factor (A.3).

The relation analogous to (3.24) between $f(x,t)$ and $f_\omega(x)$ leads to the following relations between $f_\omega(x)$ and the components of $\widetilde{\boldsymbol{f}}(x,s)$:

$$(\widetilde{\boldsymbol{f}})_1(x,s) = \widetilde{\mathrm{Re}f}(x,s) = \frac{1}{2}\left(\frac{f_{\omega_s+\Omega}(x)}{E_s(x)} + \frac{f^*_{\omega_s-\Omega}(x)}{E^*_s(x)}\right) \tag{D.6}$$

$$(\widetilde{\boldsymbol{f}})_2(x,s) = \widetilde{\mathrm{Im}f}(x,s) = \frac{1}{2j}\left(\frac{f_{\omega_s+\Omega}(x)}{E_s(x)} - \frac{f^*_{\omega_s-\Omega}(x)}{E^*_s(x)}\right) \tag{D.7}$$

where $s = j\Omega$. From the correlation relations (D.3) for $f_\omega(x)$ we can finally obtain correlation relations for the components of $\widetilde{\boldsymbol{f}}(x,s)$ and thereby explicit expressions for the elements of the diffusion matrix in (4.82). They read

$$\begin{aligned}(\boldsymbol{D})_{11} &= (\boldsymbol{D})_{22} = \frac{1}{4|E_s|^2}(D_f(x,\omega_s+\Omega) + D_f(x,\omega_s-\Omega)) \\ (\boldsymbol{D})_{12} &= (\boldsymbol{D})^*_{21} = \frac{1}{4j|E_s|^2}(D_f(x,\omega_s+\Omega) - D_f(x,\omega_s-\Omega))\,.\end{aligned} \tag{D.8}$$

In this paper we disregard the frequency dependence of D_f, i.e. we will use the approximation

$$\boldsymbol{D} \simeq \frac{D_f(x,\omega_s)}{2|E_s|^2}\boldsymbol{I}\,. \tag{D.9}$$

Appendix E

The hopscotch method

We use the hopscotch method to integrate Eq. (5.1) and (5.2).

The x-axis is discretized and "grid" points p are equidistant and fixed. When advancing one time increment Δt, the points with even p and odd p, respectively, are treated differently. A hopscotch cycle consists of four parts. Firstly, field and carrier density at points with even p are advanced explicitly in time. Secondly, field and carrier density at points with even p are advanced implicitly in time. In the last two parts of the cycle the order of the two first parts is changed. Thus in the third part, field and carrier density at points with odd p are advanced explicitly and in the fourth part field and carrier density at points with odd p are advanced implicitly. The implicit steps yield nonlinear systems of difference equations which are solved through Newton iteration. The Jacobian for this purpose is derived analytically.

First we show how to explicitly advance the field and carrier density a step in time, which is trivial. Thereafter we give the equations for the implicit step. Since our regarded system of PDEs is nonlinear, the implicit part will involve Newton-iteration.

The equations for the field in (5.1) may be written

$$\frac{j+\epsilon}{2k_r}\frac{\partial^2}{\partial x^2}E+\frac{1}{v_g}\frac{\partial}{\partial t}E-\frac{1+j\alpha}{2}\frac{\partial g}{\partial N}(N-N_0)E+\left(\frac{\alpha_i+\alpha_m}{2}\right)E+j\frac{\alpha\alpha_i}{2}E=f(x,t) \tag{E.1}$$

when including the small real number ϵ. Also, let us restate Eq. (5.2):

$$\frac{\partial}{\partial t}N(x,t)=J(x,t)+D\frac{\partial^2}{\partial x^2}N-\frac{N(x,t)}{\tau_R}-v_g g_m(x,t)B|E(x,t)|^2. \tag{E.2}$$

We will find it useful to separate the field equation into real and imaginary parts: The real part is given as

$$-\frac{\epsilon}{2k_r}\frac{\partial^2}{\partial x^2}E_R - \frac{1}{2k_r}\frac{\partial^2}{\partial x^2}E_I + \frac{1}{v_g}\frac{\partial}{\partial t}E_R + \frac{1}{2}\Gamma a(N-N_0)(\alpha E_I - E_R) + \left(\frac{\alpha_i+\alpha_m}{2}\right)E_R - \frac{\alpha\alpha_i}{2}E_I = f_R(x,t), \tag{E.3}$$

while the imaginary part reads

$$-\frac{\epsilon}{2k_r}\frac{\partial^2}{\partial x^2}E_I + \frac{1}{2k_r}\frac{\partial^2}{\partial x^2}E_R + \frac{1}{v_g}\frac{\partial}{\partial t}E_I - \frac{1}{2}\Gamma a(N-N_0)(\alpha E_R + E_I) + \left(\frac{\alpha_i+\alpha_m}{2}\right)E_I + \frac{\alpha\alpha_i}{2}E_R = f_I(x,t). \tag{E.4}$$

We now describe such a hopscotch cycle applied to our system of PDEs in more detail.

The field at the position x_p is explicitly advanced one time increment as

$$E_p^{q+1} = -j\mathscr{A}r(E_{p-1}^q + E_{p+1}^q) + \left[1 + 2j\mathscr{A}r + \Delta t v_g\frac{1+j\alpha}{2}\Gamma a(N_p^q - N_0) + \Delta t v_g\frac{\alpha_i+\alpha_m}{2} + \Delta t v_g j\frac{\alpha\alpha_i}{2}\right]E_p^q + \Delta t v_g f_p^q, \tag{E.5}$$

where $r = \Delta t/(\Delta x)^2$ and $\mathscr{A} = v_g(1+j\epsilon)/(2k_r)$. The carrier density at the position x_p is explicitly advanced one time increment as

$$N_p^{q+1} = \Delta t(J_p^q - v_g a N_0 B|E_p^q|^2) + Dr(N_{p+1}^q + N_{p-1}^q) + (1 - 2Dr - \frac{\Delta t}{\tau_R} - \Delta t v_g a B|E_p^q|^2)N_p^q. \tag{E.6}$$

Next, we use Eqs. (E.3) and (E.4) to get expressions for an implicit advancement of the field. Let $\mathscr{A}' = v_g/(2k_r)$ and $\mathscr{A}'' = v_g\epsilon/(2k_r)$. For the real part of the field equation one obtains

$$E_{R,p}^{q+1} - E_{R,p}^q = \mathscr{A}'r(E_{I,p+1}^{q+1} - 2E_{I,p}^{q+1} + E_{I,p-1}^{q+1}) + \mathscr{A}''r(E_{R,p+1}^{q+1} - 2E_{R,p}^{q+1} + E_{R,p-1}^{q+1}) - v_g\frac{1}{2}\Gamma a\Delta t(N_p^{q+1} - N_0)(\alpha E_{I,p}^{q+1} - E_{R,p}^{q+1}) - \left(\frac{\alpha_i+\alpha_m}{2}\right)\Delta t v_g E_{R,p}^{q+1} + \Delta t v_g\frac{\alpha\alpha_i}{2}E_{I,p}^{q+1} + \Delta t v_g f_{R,p}^{q+1} \tag{E.7}$$

Rearranging terms in (E.7) and defining the function $T_1(E_{R,p}^{q+1}, E_{I,p}^{q+1}, N_p^{q+1})$ yields

$$0 = E_{R,p}^{q} - E_{R,p}^{q+1}\left[1 - \Delta t v_g \frac{1}{2}\Gamma a(N_p^{q+1} - N_0) + \Delta t v_g\left(\frac{\alpha_i + \alpha_m}{2}\right) + 2\mathscr{A}'' r\right]$$
$$- E_{I,p}^{q+1}\left[2\mathscr{A}' r + \alpha\Delta t v_g \frac{1}{2}\Gamma a(N_p^{q+1} - N_0) - \Delta t v_g \frac{\alpha\alpha_i}{2}\right] + \mathscr{A}'' r(E_{R,p+1}^{q+1} + E_{R,p-1}^{q+1}) +$$
$$r\mathscr{A}'(E_{I,p+1}^{q+1} + E_{I,p-1}^{q+1}) + \Delta t v_g f_{R,p}^{q+1} \equiv T_1(E_{R,p}^{q+1}, E_{I,p}^{q+1}, N_p^{q+1}). \tag{E.8}$$

Likewise for the imaginary part of the field equation

$$E_{I,p}^{q+1} - E_{I,p}^{q} = -\mathscr{A}' r(E_{R,p+1}^{q+1} - 2E_{R,p}^{q+1} + E_{R,p-1}^{q+1}) + \mathscr{A}'' r(E_{I,p+1}^{q+1} - 2E_{I,p}^{q+1} + E_{I,p-1}^{q+1}) +$$
$$\Delta t v_g \frac{1}{2}\Gamma a(N_p^{q+1} - N_0)(\alpha E_{R,p}^{q+1} + E_{I,p}^{q+1})$$
$$- \Delta t v_g\left(\frac{\alpha_i + \alpha_m}{2}\right) E_{I,p}^{q+1} - \Delta t v_g \frac{\alpha\alpha_i}{2} E_{R,p}^{q+1} + \Delta t v_g f_{I,p}^{q+1}. \tag{E.9}$$

Also rearranging terms in (E.9) and defining the function $T_2(E_{R,p}^{q+1}, E_{I,p}^{q+1}, N_p^{q+1})$ yields

$$0 = E_{I,p}^{q} - E_{I,p}^{q+1}\left[1 - \Delta t v_g \frac{1}{2}\Gamma a(N_p^{q+1} - N_0) + \Delta t v_g\left(\frac{\alpha_i + \alpha_m}{2}\right) - 2\mathscr{A}'' r\right]$$
$$+ E_{R,p}^{q+1}\left[2\mathscr{A}' r + \alpha\Delta t v_g \frac{1}{2}\Gamma a(N_p^{q+1} - N_0) - \Delta t v_g \frac{\alpha\alpha_i}{2}\right] -$$
$$\mathscr{A}' r(E_{I,p+1}^{q+1} + E_{I,p-1}^{q-1}) + \mathscr{A}'' r(E_{R,p+1}^{q+1} + E_{R,p-1}^{q-1}) + \Delta t G_{I,p}^{q+1} \equiv M_3(E_{R,p}^{q+1}, E_{I,p}^{q+1}, N_p^{q+1}). \tag{E.10}$$

The carrier density at point q is advanced implicitly as

$$N_p^{q+1} - N_p^{q} = \Delta t J_p^{q+1} + Dr(N_{p-1}^{q+1} - 2N_p^{q+1} + N_{p+1}^{q+1}) - \frac{\Delta t}{\tau_R} N_p^{q+1} - \Delta t v_g a(N_p^{q+1} - N_0) B|E_q^{p+1}|^2. \tag{E.11}$$

Now (E.11) is rearranged and the function $T_3(E_{R,p}^{q+1}, E_{I,p}^{q+1}, N_p^{q+1})$ is defined

$$0 = N_p^{q} - N_p^{q+1}(1 + 2Dr + \frac{\Delta t}{\tau_R} + \Delta t v_g a B|E_q^{p+1}|^2) + Dr(N_{p+1}^{q+1} + N_{p-1}^{q+1}) +$$
$$\Delta t J_p^{q+1} + \Delta t N_0 v_g a B|E_q^{p+1}|^2 \equiv T_3(E_{R,p}^{q+1}, E_{I,p}^{q+1}, N_p^{q+1}). \tag{E.12}$$

When advancing implicitly we must solve the nonlinear set of equations for the three unknowns $E_{R,p}^{q+1}$, $E_{I,p}^{q+1}$, and N_p^{q+1}, i.e.

$$T_1(E_{R,p}^{q+1}, E_{I,p}^{q+1}, N_p^{q+1}) = 0 \tag{E.13}$$

$$T_2(E_{R,p}^{q+1}, E_{I,p}^{q+1}, N_p^{q+1}) = 0 \tag{E.14}$$

$$T_3(E_{R,p}^{q+1}, E_{I,p}^{q+1}, N_p^{q+1}) = 0. \tag{E.15}$$

The unknowns are computed through Newton iteration. For this purpose we need the Jacobian whose nine elements are seen to be

$$\frac{\partial T_1}{\partial E_{R,p}^{q+1}} = -\left[1 - \Delta t v_g \frac{1}{2}\Gamma a(N_p^{q+1} - N_0) + \Delta t v_g \left(\frac{\alpha_i + \alpha_m}{2}\right) + 2\mathscr{A}'' r\right] \tag{E.16}$$

$$\frac{\partial T_1}{\partial E_{I,p}^{q+1}} = -\left[2\mathscr{A}' r + \alpha \Delta t v_g \frac{1}{2}\Gamma a(N_p^{q+1} - N_0) - \Delta t v_g \frac{\alpha \alpha_i}{2}\right] \tag{E.17}$$

$$\frac{\partial T_1}{\partial N_p^{q+1}} = \Delta t v_g \frac{1}{2}\Gamma a(E_{R,p}^{q+1} - \alpha E_{I,p}^{q+1}) + \Delta t v_g \frac{\partial f_{R,p}^{q+1}}{\partial N_p^{q+1}} \tag{E.18}$$

$$\frac{\partial T_2}{\partial E_{R,p}^{q+1}} = 2\mathscr{A}' r + \alpha \Delta t v_g \frac{1}{2}\Gamma a(N_p^{q+1} - N_0) - \Delta t v_g \frac{\alpha \alpha_i}{2} \tag{E.19}$$

$$\frac{\partial T_2}{\partial E_{I,p}^{q+1}} = -\left[1 - \Delta t v_g \frac{1}{2}\Gamma a(N_p^{q+1} - N_0) + \Delta t v_g \left(\frac{\alpha_i + \alpha_m}{2}\right) - 2\mathscr{A}'' r\right] \tag{E.20}$$

$$\frac{\partial T_2}{\partial N_p^{q+1}} = \Delta t v_g \frac{1}{2}\Gamma a(\alpha E_{R,p}^{q+1} + E_{I,p}^{q+1}) + \Delta t v_g \frac{\partial f_{I,p}^{q+1}}{\partial N_p^{q+1}} \tag{E.21}$$

$$\frac{\partial T_3}{\partial E_{R,p}^{q+1}} = 2E_{R,p}^{q+1}(N_0 - N_p^{q+1})\Delta t v_g a B \tag{E.22}$$

$$\frac{\partial T_3}{\partial E_{I,p}^{q+1}} = 2E_{I,p}^{q+1}(N_0 - N_p^{q+1})\Delta t v_g a B \tag{E.23}$$

$$\frac{\partial T_3}{\partial N_p^{q+1}} = -(1 + 2Dr + \frac{\Delta t}{\tau_R} + \Delta t v_g a B |E_q^{p+1}|^2). \tag{E.24}$$

One advantage of the hopscotch method is that after advancing the field and carrier density explicitly at points, say, even p, the only unknowns in the implitic integration at a given odd p are $E_{R,p}^{q+1}$, $E_{I,p}^{q+1}$, and N_p^{q+1}.

The spatially filtering delay term in Eq. (5.18) is easily included. The time delay involves a stack, and the integral may either be obtained through direct integraton or by using Fast Fourier Transforms. We have done the former.

Appendix F

Modal expansion -method of solution

Having established the model equations, we now describe the procedure of calculating a stationary solution, i.e. a point in the $(\omega_s, \overline{N})$-plane along with the coefficients ΔN_u and the lateral field distribution $E_m(x) = \xi_m \phi_m(x)$. Then Eqs. (6.12), (6.13), and (6.14) governing the carrier density and Eqs. (6.9) with (6.6) governing the field constitute the nonlinear set of algebraic equations to be solved iteratively.

Initially, we must choose the mode order m of the mode Φ_m that we wish to regard. The iteration-scheme is prepared (the zeroth iteration) by setting all $\Delta N_u^{(0)} = 0$ implying $\Phi_m^{(0)} = \psi_m$ (the iteration number is denoted in the parenthesis). Then only the mth equation in the system of Eq. (6.9) has to be solved for $(\omega_s, \overline{N})^{(0)}$. With the obtained $(\omega_s, \overline{N})^{(0)}$, Eq. (6.12) is used to scale the field, i.e. to find $\xi_m^{(0)}$ as $|E_m^{(0)}|^2 = (\xi_m^{(0)})^2 |\phi_m^{(0)}|^2$. The core of the iteration-scheme may now begin by solving the linear system of Eq. (6.13) for the Fourier coefficients $\Delta N_u^{(1)}$ using the scaled field. This is easily done numerically [96]. The calculated coefficients $\Delta N_u^{(1)}$ are then inserted into the full system of equations of Eq. (6.9). To find a solution of Eq. (6.9), $(\omega_s, \overline{N})^{(1)}$ must be found such that the determinant of the matrix be zero. A Newton-Raphson algorithm is used for this. We now have a singular matrix, and the coefficients $(b_m^q)^{(1)}$ may be obtained using a singular value decomposition [61][96]. This gives $\Phi_m^{(1)}$ by Eq. (6.1) and the scaling factor $\xi_m^{(1)}$ by means of Eq. (6.12). With the scaled field $|E_m^{(1)}|^2$, Eq. (6.13) is solved for the Fourier coefficients $\Delta N_u^{(2)}$ and so on. Note that in (6.12) the field is

scaled using $(\omega_s, \overline{N})^{(i)}$ and $\Delta N_u^{(i-1)}$. The iteration scheme and is continued until $(\omega_s, \overline{N})$, the coefficients ΔN_u, and $|E_m(x)|^2$ have converged. We find that in general at least the first $3m + 2$ modes ψ_q are needed in the modal expansion for good convergence since field coefficients as high as b_m^{3m+2} may be non-negligible. In the calculations we use 100 modes.

Appendix G

Papers and presentations

Minjung Chi, Søren Blaaberg Jensen, Jean-Pierre Huignard and Paul Michael Petersen, "Two-wave mixing in a broad-area semiconductor amplifier", submitted to *Optics Express*.

Paul M. Petersen, Eva Samsøe, Søren B. Jensen, and Peter Andersen, "Guiding of laser modes based on self-pumped four-wave mixing in a semiconductor amplifier", *Optics Express*, Vol. 13, Issue 9, pp. 3340-3347.

Søren Blaaberg, Paul Michael Petersen, Bjarne Tromborg, "Structure of lateral modes of a broad area semiconductor laser, their stability and spectral properties", in preperation.

Søren Blaaberg Jensen, Bjarne Tromborg, and Paul Michael Petersen. "Spatially nondegenerate four-wave mixing in a broad area semiconductor laser: Modeling", *Northern Optics 2003*, Poster presentation: June, 2003, Helsinki.

Søren Blaaberg Jensen, "A Model for Broad area lasers," *Biomedical Optics 04*, Talk: November 2004, Kgs. Lyngby.

Søren Blaaberg Jensen, "Spatially nondegenerate four-wave mixing in a broad area laser", *European Semiconductor Laser Workshop 2003*, September 2003, Torino Italy.

Bibliography

[1] R. J. Lang, A. G. Larsson, and J. G. Cody, "Lateral modes of broad area semiconductor lasers: Theory and experiment," *IEEE Journal of Quantum Electronics*, vol. 27, no. 3, pp. 312–320, 1991.

[2] I. Fischer, O. Hess, W. Elsasser, and E. Goebel, "Complex spatio-temporal dynamics in the near-field of a broad-area semiconducto laser," *Europhysics letters*, vol. 35, no. 8, pp. 579–584, 1996.

[3] O. Hess and T. Kuhn, "Maxwell-Bloch equations for spatially inhomogeneous semiconductor lasers. i. theoretical formulation," *Physical Review A*, vol. 54, no. 4, pp. 3347–3359, 1996.

[4] O. Hess and T. Kuhn, "Maxwell-Bloch equations for spatially inhomogeneous semiconductor lasers. ii. spatiotemporal dynamics," *Physical Review A*, vol. 54, no. 4, pp. 3360–3368, 1996.

[5] A. Klehr, G. Beister, G. Erbert, A. Klein, J. Maege, I. Rechenberg, J. Sebastian, H. Wnezel, and G. Trankle, "Defect recognition via longitudinal mode analysis of high power fundamental mode and broad are edge emitting laser diodes," *Journal of Applied Physics*, vol. 90, no. 1, pp. 43–47, 2001.

[6] M. Lucente, J. Fujimoto, and G. Carter, "Spatial and frequency dependence of four-wave mixing in broad-area diode lasers," *Journal of Applied Physics*, vol. 53, no. 20, pp. 1897–1899, 1988.

[7] C. J. Chang-Hasnain, E. Kapon, and E. Colas, "Spatial mode structure of index-guided broad-area quantum-well lasers," *Applied Physics Letters*, vol. 26, no. 10, pp. 1713–1716, 1990.

[8] D. Botez, "Design considerations and analytical approximations for high continuos-wave power, broad-waveguide diode lasers," *Applied Physics Letters*, vol. 74, no. 21, pp. 3102–3104, 1999.

[9] B. Sumpf, S. Deubert, G. Erbert, J. Fricke, J. Reithmaier, A. Forcehl, R. Staske, and G. Traenkle, "Nonlinear properties of tapered laser cavities," *IEEE Journal of Quantum Electronics*, vol. 9, no. 3, pp. 823–834, 2003.

[10] M. Chi, B. Thestrup, and P. M. Petersen, "Self-injection locking of an extraordinarily wide broad-area diode laser with a 1000-μm-wide emitter," *Optics Letters*, vol. 30, no. 10, pp. 1147–1149, 2005.

[11] A. Moser, E.-E. Letta, and D. Webb, "Thermodynamics approach to ccatastrophic optical mirror damage of AlGaAs," *Applied Physics Letters*, vol. 55, no. 12, pp. 1152–1154, 1989.

[12] T. Burkhard, M. O. Siegler, I. Fischer, and W. Elsasser, "Spatiotemporal dynamics of broad area semiconductor lasers and its charaterization," *Chaos, Solitons and Fractals*, vol. 19, no. 4-5, pp. 845–850, 1999.

[13] R. J. Lang, D. Meheuys, and D. Welch, "Spontaneous filamentation in broad-area diode laser amplifiers," *IEEE Journal of Quantum Electronics*, vol. 30, no. 3, pp. 685–694, 1994.

[14] D. Mehuys, R. J. Lanf, M. Mittelstein, J. salzman, and A. Yariv, "Self-stabilized nonlinear lateral modes of broad area lasers," *IEEE Journal of Quantum Electronics*, vol. 23, no. 11, pp. 1909–1920, 1987.

[15] R. J. Lang, K. Dzurko, A. A. HArdy, S. Demars, and A. Schoenfleder, "Theory of grating-confined broad-area lasers," *IEEE Journal of Quantum Electronics*, vol. 34, no. 11, pp. 2196–2210, 1998.

[16] K. P. *et al.*, "Design, fabrication and characterization of high-power angled-grating distributed-feedback lasers," in *Semiconductor Laser Conference, 2002. IEEE 18th International*, IEEE, pp. 25–26, 2002.

[17] J. Hohimer, D. C. G. Vawter, and D. Myers, "Near-diffraction-limited angle-switchable output beam from a broad-area diode laser with an

intracavity spatial phase controller," *Applied Physics Letters*, vol. 58, no. 25, pp. 2886–2888, 1991.

[18] D. Mehuys, S. O'Brien, R. Lang, and A. Hardy, "5 W, diffraction-limited, tapered-stripe unstable resonator semiconductor laser," *Electronics Letters*, vol. 30, no. 22, pp. 1855–1856, 1994.

[19] M. Munkel, F. Kaiser, and O. Hess, "Spatio-temporal dynamics of multistripe semiconductor lasers with delayed optical feedback," *Physics Letters A*, vol. 222, pp. 67–75, 1996.

[20] S. K. Mandre, I. Fischer, and W. Elsasser, "Control of the spatiotemporal emission of a broad-area semiconductor laser by spatially filtered feedback," *Optics Letters*, vol. 28, no. 13, pp. 1135–1137, 2003.

[21] S. Wolff and H. Fouckhardt, "Intracavity stabilization of broad area lasers by structured delayed optical feedback," *Optics Express*, vol. 7, no. 6, pp. 222–227, 2000.

[22] C. Simmendinger, M. Munkel, and O. Hess, "Controling complex temporal and spatio-temporal dynamics in semiconductor lasers," *Chaos, Solitons and Fractals*, vol. 19, no. 4-5, pp. 851–864, 1999.

[23] P. Ru, W. Chow, J. Moloney, and S. Koch, "Quantum confinement and strain effects on the lateral mode stability of an unstable resonator semiconductor laser," *Applied Physics Letters*, vol. 64, no. 12, pp. 1469–1471, 1994.

[24] J. Lawrence and D. Kane, "Broad-area diode lasers with plane-mirror and phase-conjugate feedback," *Journal of lightwave technology*, vol. 20, no. 1, pp. 100–104, 2002.

[25] V. Reboud, N. Debreuil, P. Fournet, G. Pauliat, and G. Roosen, "Selv-induced transverse mode selection in a photorefractive extended cavity laser diode," *Optics Express*, vol. 14, no. 7, pp. 2735–2743, 2006.

[26] L. Goldberg and J. Weller, "Broad-area high-power semiconductor amplifier," *Applied Physics Letters*, vol. 58, no. 13, pp. 1357–1359, 1991.

[27] G. Abbas, S. Yang, V. Chan, and J. G. Fujimoto, "Injection behavior and modeling of 100 mw braod area diode lasers," *IEEE Journal of Quantum Electronics*, vol. 24, no. 4, pp. 609–617, 1988.

[28] G. Dente and M. Tilton, "Modeling broad-area semiconductor optical amplifiers," *IEEE Journal of Quantum Electronics*, vol. 29, no. 1, pp. 76–88, 1993.

[29] C. J. Chang-Hasnain, J. Berger, W. S. D. R. Scifres, J. R. Whinnery, and A. Dienes, "High power with high efficiency in a narrow single-lobed beam from a diode laser array in an external cavity," *Applied Physics Letters*, vol. 50, no. 21, pp. 1465–1467, 1987.

[30] J. R. Marciante and G. P. Agrawal, "Lateral spatial effects of feedback in gain-guided and broad-area semiconductor lasers," *IEEE Journal of Quantum Electronics*, vol. 32, no. 9, pp. 1630–1635, 1996.

[31] Y. Champagne, S. Mailhot, and N. McCarthy, "Numerical procedure for the lateral-mode analysis of broad-area semiconductor lasers with an external cavity," *IEEE Journal of Quantum Electronics*, vol. 31, no. 5, pp. 795–810, 1995.

[32] V. Raab and R. Menzel, "External resonator design for high-power laser diodes that yields 400 mw of TEM_{00} power," *Optics Letters*, vol. 27, no. 3, pp. 167–169, 2002.

[33] M. Chi, N.-S. Boegh, B. Thestrup, and P. M. Petersen, "Imrovement of the beam quality of a broad-area diode laser using double feedback from two external mirrors," *Applied Physics Letters*, vol. 85, no. 7, pp. 1107–1109, 2004.

[34] B. Thestrup, M. Chi, and P. M. Petersen, "Lateral mode selection in a broad area laser diode by self-injection locking with a mirror stripe," in *High-Power Diode Laser Technology and Applications II*, vol. 5336 of *Proc. SPIE*, pp. 38–44, 2004.

[35] E. Samsoe, P. Andersen, S. Andersson-Engels, and P. Petersen, "Improvement of spatial and temporal coherence of a broad area laser diode using an external-cavity design with double grating feedback," *Optics Express*, vol. 12, no. 4, pp. 609–616, 2004.

[36] J. Chen, X. Wu, J. Ge, A. Hermerschmidt, and H. J. Eichler, "Broad-area laser diode with 0.02 nm bandwidth and diffraction limited output due to double external cavity feedback," *Applied Physics Letters*, vol. 85, no. 4, pp. 525–527, 2004.

[37] M. Loebel, *Improvement of the coherence charateristics of laser diode arrays using photorefractive phase conjugation*. PhD thesis, Risoe National Laboratory, 1998.

[38] C. Gao and H. Weber, "The proplem with m^2," *Optics and Laser Technology*, vol. 32, pp. 221–224, 2000.

[39] W. W. Chow, S. W. Coch, and M. Sargent III, *Semiconductor laser physics*. Berlin Heidelberg: Springer-Verlag, 1994.

[40] S. Sujecki, L. Borruel, J. Wykes, P. Moreno, B. Sumpf, P. Sewell, H. Wenzel, T. M. Benson, G. Erbert, I. Esquivas, and E. C. Larkins, "Nonlinear properties of tapered laser cavities," *IEEE Journal of Quantum Electronics*, vol. 9, no. 3, pp. 823–834, 2003.

[41] H. Adachihara, O. Hess, E. Abraham, P. Ru, and J. Moloney, "Spationaltemporal chaos in broad-area semiconductor lasers," *J. Opt. Soc. Am. B*, vol. 10, no. 4, pp. 658–665, 1993.

[42] K. Petermann, "External optical feedback phenomena in semiconductor lasers," *IEEE Journal of Quantum Electronics*, vol. 1, no. 2, pp. 480–489, 1995.

[43] G. P. Agrawal and N. K. Dutta, *Semiconductor Lasers*. Ney York, NY: Van Nordstrand Reinhold, second ed., 1993.

[44] J. Moerk, *Nonlinear dynamics and stochastic behaviour of semiconductor lasers with optical feedback*. PhD thesis, Technical University of Denmark, 1989.

[45] O. Hess, S. W. Koch, and J. V. Moloney, "Filamentation and beam propagation in broad-area semiconductor lasers," *IEEE Journal of Quantum Electronics*, vol. 31, no. 1, pp. 35–43, 1995.

[46] J. Buus, "The effective index method and its application to semiconductor lasers," *IEEE Journal of Quantum Electronics*, vol. 18, no. 7, pp. 1083–1089, 1982.

[47] E. Abraham and S. Smith, "Optical bistability and related devices," *Rep. Prog. Phys.*, vol. 45, pp. 815–885, 1982.

[48] B. Tromborg, H. Olesen, and X. Pan, "Theory of linewidth for multi-electrode laser diodes with spatially distributed noise sources," *IEEE Journal of Quantum Electronics*, vol. 27, no. 2, pp. 178–192, 1991.

[49] C. H. Henry, "Theory of spontaneous emission noise in open resonators and its application to lasers and optical amplifiers," *Journal of lightwave technology*, vol. 4, no. 3, pp. 288–297, 1986.

[50] B. Tromborg, H. Olesen, X. Pan, and S. Saito, "Transmission line description of optical feedback and injection locking for Fabry-Perot and DFB lasers," *IEEE Journal of Quantum Electronics*, vol. 23, no. 11, pp. 1875–1889, 1987.

[51] N. Eriksson, A. Larsson, M. Uemukai, and T. Suhara, "Parabolic-confocal unstable-resonator semiconductor lasers -modeling and experiments," *IEEE Journal of Quantum Electronics*, vol. 34, no. 5, pp. 858–868, 1998.

[52] C. H. Henry, "Theory of the linewidth of semiconductor lasers," *IEEE Journal of Quantum Electronics*, vol. 18, no. 2, pp. 259–264, 1982.

[53] D. J. Bossert and D. Gallant, "Gain, refractive index, and α-parameter in InGaAs-GaAs SQW broad-area lasers," *IEEE Photonics technology letters*, vol. 8, no. 3, pp. 322–324, 1996.

[54] L. A. Coldren and S. W. Corzine, *Diode Lasers and Photonic Integrated Circuits*. New York, NY: John Wiley and sons, 1995.

[55] E. O'neil, P. O'Brien, and J. McInerney, "Modification of internal temperature distribution in broad area semiconductor lasers and the effect on near- and far-field," in *Semiconductor Laser Conference, 2002. IEEE 18th International*, IEE Proc.-Optoelectron., pp. 31–35, 2000.

[56] J. Verdiell and R. Frey, "A broad-area mode-coupling model for multible-stripe semiconductor lasers," *IEEE Journal of Quantum Electronics*, vol. 26, no. 2, pp. 270–279, 1990.

[57] E. Gehrig, O. Hess, and R. Wallenstein, "Modeling of the performance of high-power diode amplifier systems with an optothermal microscopic spatio-temporal theory," *IEEE Journal of Quantum Electronics*, vol. 35, no. 3, pp. 320–331, 1999.

[58] A. Larsson, J. Salzman, M. Mittelstein, and A. Yariv, "Lateral coherence properties of broad-area semiconductor quantum well lasers," *Journal of Applied Physics*, vol. 60, no. 1, pp. 66–68, 1986.

[59] W. Joyce, "Current-crowded carrier confinement in double-heterostructure lasers," *Journal of Applied Physics*, vol. 51, no. 5, pp. 2394–2401, 1980.

[60] J. K. White, J. G. McInerney, and J. V. Moloney, "Effects of the injection current profile shape on the sidelobes in large-aperture semiconducor laser amplifiers," *Optics Letters*, vol. 20, no. 6, pp. 593–595, 1995.

[61] W. H. Press, S. A. Teukolsky, W. T. Vetterling, and B. P. Flannery, *Numerical Recipes in Fortran 77: The Art of Scientific Computing*. New York, NY: Cambridge University Press, second ed., 1992.

[62] J. Smoller and A. G. Wasserman, "Symmetry-breaking for solutions of semilinear elliptic equations with general boundary conditions," *Communications in mathematical physics*, vol. 105, pp. 415–441, 1986.

[63] R. Diehl, *High-power diode lasers. Fundamentals, technology, Applications*. Heidelberg: Springer-Verlag, 2000.

[64] S. Mailhot, Y. Champagne, and N. McCarthy, "Single-mode operation of a broad-area semiconductor laser with an anamorphic external cavity: experimental and numerical results," *Applied Optics*, vol. 39, no. 36, pp. 6806–6813, 2000.

[65] C. J. Chang-Hasnain, E. Kapon, and R. Bhat, "Spatial mode structure of broad-area semiconductor quantum well lasers," *Applied Physics Letters*, vol. 54, no. 3, pp. 205–207, 1989.

[66] E. Ultanir, G. Stegeman, D. Micaelis, C. Lange, and F. Lederer, "Stable disspative solitons in semiconductor optical amplifiers," *Physical Review Letters*, vol. 90, no. 25, p. 253903, 2003.

[67] H. Olesen, B. Tromborg, X. Pan, and H. Lassen, "Stability and dynamci properties of multi-electrode laser diodes using a Green's function approach," *IEEE Journal of Quantum Electronics*, vol. 29, no. 8, pp. 2282–2301, 1993.

[68] J. Buus, "Models of the static and dynamic behavior of stripe geometry lasers," *IEEE Journal of Quantum Electronics*, vol. 19, no. 6, pp. 953–960, 1983.

[69] B. Tromborg, H. E. Lassen, and H. Olesen, "Traveling wave analysis of semiconductor lasers: Modulation responses, mode stability and quantum mechanical treatment of noise spectra," *IEEE Journal of Quantum Electronics*, vol. 30, no. 4, pp. 939–956, 1994.

[70] P. Morse and H. Feshback, *Methods of theoretical physics*. New York: McGraw Hill, 1953.

[71] B. Tromborg, H. L. abd H. Olesen, and X. Pan, "Traveling wave method for calculation of liewidth, frequency tuning and astability of semicoductor lasers," *IEEE Photonics technology letters*, vol. 4, no. 9, pp. 985–988, 1991.

[72] E. Mosekilde and R. Feldberg, *Ikke-lineaer dynamik og kaos*. Lyngby: Polyteknisk Forlag, 1994.

[73] S. Wolff, A. Rodionov, V. E. Sherstobitov, and H. Fouckhardt, "Fourer-optical transverse mode selection in external-cavity broad-area lasers: Experimental and numerical results," *IEEE Journal of Quantum Electronics*, vol. 39, no. 3, pp. 448–458, 2003.

[74] E. Detoma, B. Tromborg, and I. Montrosset, "The complex way to laser diode spectra: Example of an external cavity laser strong optical feedback," *IEEE Journal of Quantum Electronics*, vol. 41, no. 2, pp. 171–181, 2005.

[75] M. Shtaif, B. Tromborg, and G. Eisenstein, "Noise spectra of semiconductor optical amplifiers: Relation between semiclassical and quantum descriptions," *IEEE Journal of Quantum Electronics*, vol. 34, no. 5, pp. 869–878, 1998.

[76] A. Yariv, *Quantum Electronics*. Ney York, NY: John Wiley and Sons, third ed., 1988.

[77] O. Hess and T. Kuhn, "Spatio-temporal dynamics of semiconductor lasers: Theory, modelling and analysis," *Prog. Quantum Electronics*, vol. 20, no. 2, pp. 85–179, 1996.

[78] K. Tai, T. Hayes, S. McCall, and W. Tsang, "Optical measurement of surface recombination in InGaAs quantum well mesa structures," *Applied Physics Letters*, vol. 53, no. 4, pp. 302–303, 1988.

[79] R. Lang and K. Kobayashi, "External optical feedback effects in semiconductor injection laser properties," *IEEE Journal of Quantum Electronics*, vol. 16, no. 3, pp. 347–355, 1980.

[80] J. Moerk, B. Tromborg, and J. Mark, "Chaos in semiconductor lasers woth optical feedback: theory and experiment," *IEEE Journal of Quantum Electronics*, vol. 28, no. 1, pp. 93–108, 1992.

[81] K. Verheyden, K. Green, and D. Roose, "Numerical stability analysis of a large-scale delay system modeling a lateral semiconductor lasr subject to optical feedback," *Physical Review E*, vol. 69, no. 3, pp. 036702–1–036702–5, 2004.

[82] M. Bleich and J. Solocor, "Controlling spatiotemporal dynamics with time-delay feedback," *Physical Review E*, vol. 54, no. 1, pp. 17–20, 1996.

[83] M. Bleich, D. Hochheiser, J. Moloney, and J. Solocor, "Controlling extended systems with spatially filtered, time-delayed feedback," *Physical Review E*, vol. 55, no. 3, pp. 2119–2126, 1997.

[84] D. Hochheiser, J. Moloney, and J. Lega, "Controlling optical turbulence," *Physical Review A*, vol. 55, no. 36, pp. 4011–4014, 1997.

[85] W. F. Ames, *Numerical methods for partial differential equations*. San Diego, CA: Academic Press, INC., third ed., 1992.

[86] H. Adachihara, O. Hess, R. Indik, and J. Moloney, "Semiconductor laser array dynamics: numerical simulations on multistripe index-guided lasers," *J. Opt. Soc. Am. B*, vol. 10, no. 3, pp. 496–506, 1993.

[87] V. V. Konotop and L. Vasquez, *Nonlinear random waves*. Singapore: World Scientific Pusblishing Co. Pte. Ltd., first ed., 1994.

[88] J. Houlihan, J. O'Callaghan, V. Voignier, G. Huyet, and J. McInerney, "Experimental observation of traveling waves in the transverse section of a laser," *Optics Letters*, vol. 26, no. 20, pp. 1556–1558, 2001.

[89] L. Romero, E. Zapata, and J. Ramos, "Efficient parallel solution of a semiconductor laser array dynamics model," in *High-Performance Computing and Networking (HPCN Europe'96)*, 1996.

[90] D. Merbach, O. Hess, H. Herzel, and E. Scholl, "Injection-induced bifurcations of transverse spatiotemporal patterns in semiconductor laser arrays," *Physical Review E*, vol. 52, no. 2, pp. 1571–1578, 1995.

[91] B. Thestrup. private communication.

[92] J. Lawrence and D. Kane, "etermination of the external cavity coupling coefficient for a diode laser with phase conjugate feedback," *Electronics Letters*, vol. 36, no. 6, pp. 535–537, 1999.

[93] D. Skoczowsky, V. Raab, A. Heuer, R. Menzel, S. Mandre, I. Fischer, and W. Elsasser, "ps-pulse generation by self-induced modelocking of a high power broad area diode laser in an external resonator," in *2005 CLEO Europe*, IEEE, p. 135, 2005.

[94] B. Tromborg. private communication.

[95] M. Loebel, P. Petersen, and P. M. Johansen, "Tunable single-mode operation of a high-power laser-diode array by use of an external cavity with a grating and a photorefractive phase-conjugate mirror," *J. Opt. Soc. Am. B*, vol. 15, no. 7, pp. 2000–2005, 1998.

[96] E. Anderson, Z. Bai, C. Bischof, S. Blackford, J. Demmel, J. Dongarra, J. Du Croz, A. Greenbaum, S. Hammarling, A. McKenney, and D. Sorensen, *LAPACK Users' Guide*. Philadelphia, PA: Society for Industrial and Applied Mathematics, third ed., 1999.